The Dissertation Committee for Jordan Charles Dwelle Certifies that this is the approved version of the following dissertation:

Polarization Sensitive Optical Coherence Tomography for Primate Retinal Evaluation in a Longitudinal Glaucoma Study

Committee:

H. Grady Rylander III, Co-Supervisor

Thomas E. Milner, Co-Supervisor

Andrew K. Dunn

Adela Ben-Yakar

R. Malcolm Brown Jr.

Polarization Sensitive Optical Coherence Tomography for Primate Retinal Evaluation in a Longitudinal Glaucoma Study

by

Jordan Charles Dwelle, B.S.M.E.; M.S.E.

Dissertation

Presented to the Faculty of the Graduate School of

The University of Texas at Austin

in Partial Fulfillment

of the Requirements

for the degree of

Doctor of Philosophy

The University of Texas at Austin

December 2011

Dedication

This work is thankfully dedicated to my wife Sarah who has patiently and cheerfully stood by my side down this long road and without whom I would have quit many times.

Acknowledgements

I am deeply indebted to my supervising professors for their tutelage and supervision over the past 6 years as I have performed this work. Dr. Milner has been an inspiration personally and professionally and I could spend many more years learning from him. Dr. Rylander has continually pushed me to get things done and without this pushing I don't know when, if ever, this would have all come together.

The work in this dissertation could not have been done without the help of my colleagues in the biomedical laser lab. Nate Kemp introduced me to this project and I have him to thank for a project that was intellectually interesting and socially compelling. I spent a couple of years working closely with Badr Elmaanaoui with whom I learned a lot. Bingqing Wang and Shuang Liu were invaluable help in performing the data analysis to complete this work and I am grateful to them for their hard work.

Staff at UT played a big part in making this happen and don't get as much credit as they deserve. Kathryn Starr took wonderful care of the animals used in these experiments, sat with me through every experiment, and was a compassionate and interested companion. Tony Garza helped handle and care for the animals and was always interested and encouraging. Vicki Stratton before she retired made all things administrative run smoothly and Jim Pollard was quick to ably respond to every emergency with the computers.

I am grateful to the National Institutes of Health (R01EY016462) for the support of this research and to the many taxpayers that have contributed to this and other grants for my tuition and research.

Finally I am grateful without measure to my family. My wife and children have been a source of delight to me in every way. My wife has been endlessly supportive and encouraging throughout this time and her cheerfulness never ceases to amaze me. My mother, Lynn Gossett, has been proud of me in all my endeavors and I hope this will give her more reason for pride. My in-laws Dr. David Dalton and Debra Dalton could not have been more supportive, generous, or encouraging as I have pursued this degree; they have made me a part of their family in every way and I love them deeply.

Polarization Sensitive Optical Coherence Tomography for Primate Retinal Evaluation in a Longitudinal Glaucoma Study

Publication No._____

Jordan Charles Dwelle, Ph.D.

The University of Texas at Austin, 2011

Co-Supervisor: H. Grady Rylander, III

Co-Supervisor: Thomas E. Milner

A polarization sensitive optical coherence tomography (PS-OCT) instrument is presented for the study of glaucoma. Glaucoma is the second leading cause of blindness worldwide and causes irreversible damage to the retina. This PS-OCT system was built to perform retinal imaging with a swept source laser providing a 28 kHz A-scan repetition rate. Thickness, phase retardation, birefringence and reflectance index measurements were taken from the primate eyes on a weekly or semi-weekly basis through the course of a 30 week study. Statistical analysis of these measurements indicates that the reflectance index is the earliest measured indicator of glaucomatous changes and a potential marker for early glaucoma diagnosis.

Table of Contents

LIST OF TABLES

LIST OF FIGURES

CHAPTER 1: INTRODUCTION AND BACKGROUND

1.1 ORGANIZATION OF THE DISSERTATION

Chapter 1 provides an introduction to the disease of glaucoma, which is the disease that motivates all of the study and work in this dissertation. A brief overview of the eye physiology is presented along with the current techniques for the diagnostic methods used for glaucoma. This is followed by an introduction to Optical Coherence Tomography (OCT), the technology behind the work of this dissertation.

Chapter 2 describes the work to build and characterize the Swept Source polarization sensitive (PS-OCT) system. A schematic of the system is included along with a description of the optimization process for several of the key components. A description of the electrical components and their interconnections is described. An overview of the software used to control the system and collect images is also included.

Chapter 3 describes the experimental design for the longitudinal primate study that was performed for this dissertation. The technique used for inducing glaucoma is presented along with the procedures used during the retinal imaging sessions that followed the primates through disease progression for a period of 30 weeks.

The theory and methods for processing the acquired data is presented in Chapter 4. This includes the methods for processing raw acquired data into OCT images. This is followed by boundary detection to isolate the retinal nerve fiber layer (RNFL) segment from the rest of the image. This is followed by a description of the analysis needed to

extract the measurement parameters from this segmented RNFL data. Finally statistical analysis needed to analyze the results over the course of the study are described.

Chapter 5 presents the data that was acquired through the primate study. Plots of the measured parameters are presented as progressing with time and with a measure of the retinal damage. A table of the statistical results from various regions in the eye is presented. A brief discussion of the results is included including an assessment of the statistics and a theory is considered as to the possible mechanism behind the results. Finally there are recommendations for work to further investigate the results found in this study and presented in this dissertation.

1.2 GLAUCOMA

The primary focus of this dissertation is the use of PS-OCT to quantify the retinal neuropathy known as glaucoma. Glaucoma is an optical neuropathy causing irreversible vision loss and, without intervention, blindness. Glaucoma is the second leading cause of blindness worldwide behind only cataracts[1] and it accounts for over 4.5 million cases of blindness[1]. In the U.S. it is the second most common cause of blindness, behind age-related macular degeneration, causing 120,000 cases of blindness among an estimated 2.2 million cases of glaucoma and disproportionately affects minority populations [2]. In a normal course of the disease, the patient experiences gradual visual field loss beginning at the periphery of vision with no other noticeable symptoms, especially in the most

[1] Blindness due to cataracts, a clouding of the intra-ocular crystalline lens can be cured with removal or replacement of the crystalline lens. This procedure is performed routinely in developed countries

common sub-type primary open-angle closure (POAG) glaucoma. According to several population studies, it is estimated that up to half of glaucoma cases in the U.S. are currently undiagnosed [3] ensuring that, in most cases, some vision loss will occur before treatment is started. As a result, clinicians and researchers are calling for better, earlier detection of glaucoma, a greater availability of screening techniques, and standardized classifications methods for the disease.

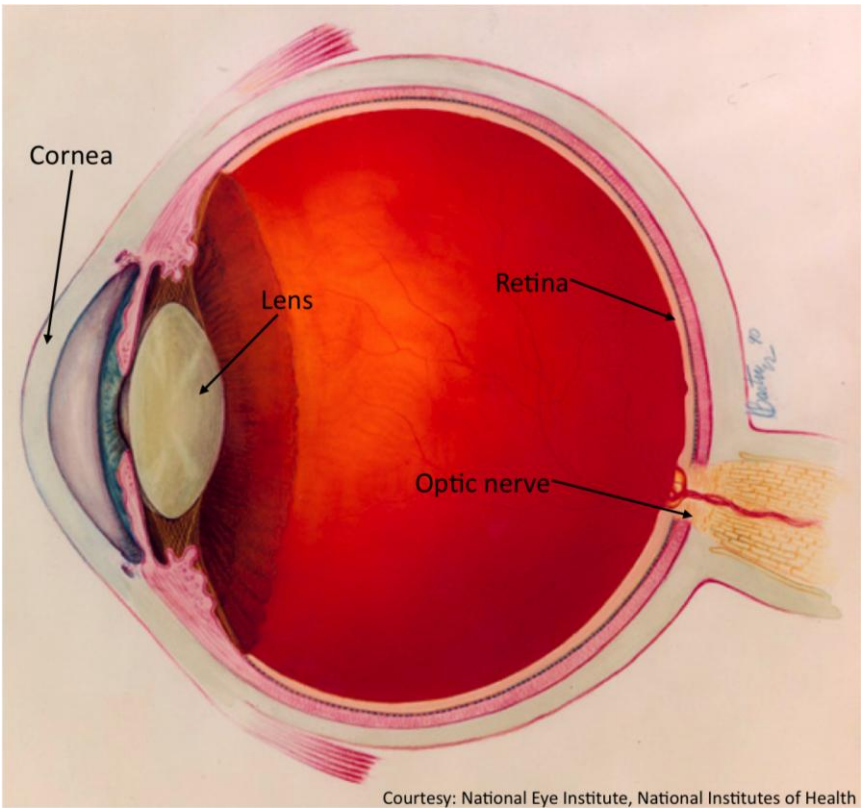

Figure 1.1. The overall eye physiology showing the main ocular elements of interest in this work.

1.2.2 Eye Physiology

In order to understand this disease, it is helpful to have a general overview of the physiology of the eye with a special emphasis on the retina. Light entering the eye is focused on the retina by the corneal surface and the lens (see figure 1.1). The retina has a complex layered structure shown in figure 1.2 to transfer nerve signals generated in the light sensitive cells at the deepest part of the retina to the ganglion nerve cells at the surface of the retina for transmission through the optic nerve head (ONH) into the brain. The first surface encountered by the light is the RNFL. The RNFL is comprised of bundles of axons, which are in turn bundles of microtubules, which transmit nerve impulses. The axons in the RNFL have a radial orientation in from the periphery of the retina towards the ONH where they pass through the retina to the visual cortex in the brain. Immediately behind these axons are the ganglion cell bodies followed by the inner plexiform layer containing dendrites. This layer of dendrites is transferring impulses from the bipolar, amacrine, and horizontal cells in the inner nuclear layer to the ganglion cells. These cells are connected to those in the rod and cone granules of the outer nuclear layer through dendrites in the outer plexiform layer. Of primary interest in glaucoma research are the retinal ganglion cells (RGC's), which die as a result of the disease. The loss of these neural cells, which function as the final transmission step from the retina to the brain, decreases the amount of information that is transmitted causing the loss of vision.

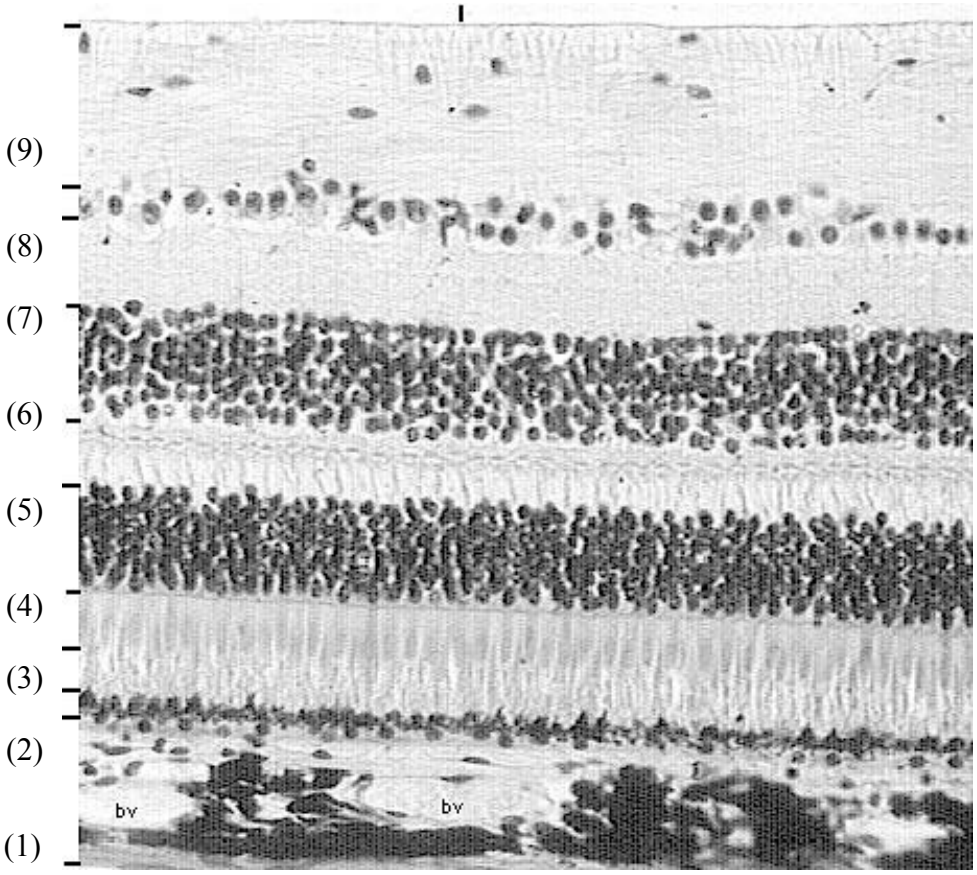

Figure 1.2. TEM closeup of retina showing layers of the retina [4]. Above the highly vascularized choroid (1) is the retinal pigment epithelium (2), followed by the the rods and cones (3), the outer nuclear layer (4), the outer plexiform layer (5), the inner nuclear layer (6), the inner plexiform layer (7), the ganglion cell bodies (8), and the RNFL (9). The RNFL layer varies in thickness according to the location in the retina from ~50 um in the nasal and temporal regions to ~150 um in the superior and inferior regions. These nerve fibers of the ganglion cell bodies (8) recede as the ganglion cells die as a result of glaucoma.

1.2.3 Glaucoma pathophysiology

The progressive loss of the RGC's has long been identified as the primary physiological effect of glaucoma and many proposed mechanisms have been identified that contribute to this neuro-degeneration. The currently accepted damage mechanisms

include increased pressure, vascular insufficiency [5-7], astrocytic reaction [8, 9], and autoimmune attack [10, 11]. Regardless of which damage mechanisms are at work in a specific case, the data suggest that the pathology of glaucoma is selective RGC death, which is followed by degeneration of RGC neurotubules [9, 12].

1.2.4 Glaucoma diagnosis

Glaucoma is commonly associated with increased ocular pressure and this is the currently one of the primary tools used for screening patients at risk for glaucoma; however, measured pressure in cases of glaucoma is not always abnormal. According to various population studies in the U.S. and abroad, between 25% and 50% of people with glaucoma have statistically normal pressures, 22mmHg or less, defining a condition known as normal tension glaucoma [13-15]. In normal tension glaucoma, where visual field defects and other disease markers exist, there remains debate about the effect of pressure on the progression of the disease. Overall, the diagnosis of glaucoma is not made solely on the basis of abnormal pressure measurements though treatment in most cases involves some means of lowering the intra-ocular pressure. To date, there have been no definitive tests developed to diagnose glaucoma before significant visual field defects arise. The current standard for diagnosing glaucoma is a complete eye examination made on individuals at risk every two years [16]. This eye examination may require multiple

office visits resulting in a costly diagnosis. The diagnosis is made based primarily on the following elements in a comprehensive eye examination[2]:

1. Intra-ocular pressure
2. Visual field test
3. ONH and RNFL evaluation

There is as yet, no clear agreement on the criteria to diagnose the disease before visual field loss has begun which, as illustrated below in figure 1.3, comes after the irreversibly damage is already well advanced.

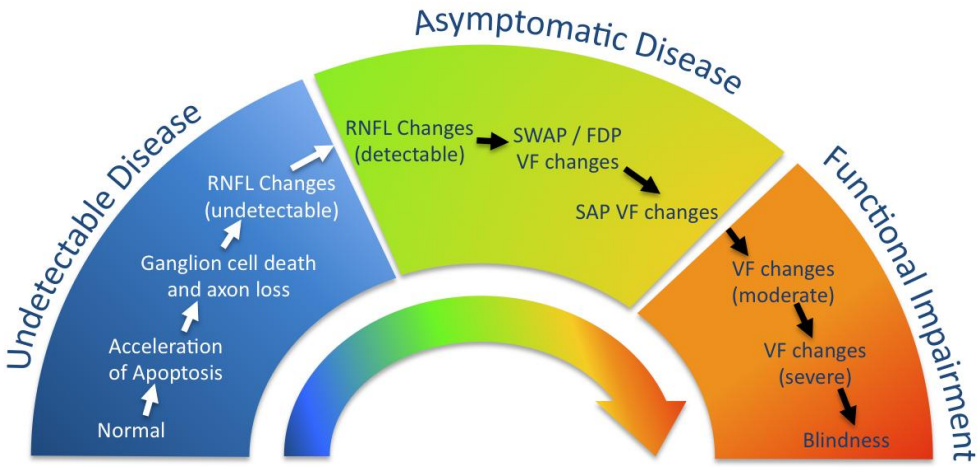

Figure 1.3. A continuum illustrating the progression of the disease and a general picture of the current technologies' ability to monitor the disease. The disease is broken down into three phases and begins with physiological changes that may take years to present as functional changes which increase in severity until blindness. Adapted from [17].

[2] This is not a complete list of the elements of a comprehensive eye examination; only the elements most relevant in the glaucoma diagnosis. The other included elements are used primarily to eliminate other factors that contribute to abnormalities in these tests.

1.2.4.1 Visual Field Tests

A typical visual field test requires a patient to respond to some visual stimuli and allows clinicians to map out the field of vision for comparison to a normal subject. The most common approach is a Goldmann visual field test where a patient must respond to a small light that is moved around the field of vision. This type of visual field test has been shown to be a late indicator of glaucomatous changes [5] and as many as 40% of the ganglion cells may be lost by the time standard visual field tests are effective [18]. Short-wavelength-automated-perimetry (SWAP) is a similar technique that uses a short wavelength stimulus and a yellow background field and has earlier detection. Another of the most important visual field tests for early glaucoma detection is frequency-doubling perimetry (FDP) with similar results to SWAP [19]. This technique relies on a normal response to an alternating sinusoidal grating where the spatial frequency appears to double if the grating is phase-flickered as was described by Kelly in 1981 [20]. This test is performed by varying the frequency of the phase flicker, spatial modulation, and contrast of a periodic pattern while monitoring the subject's visualization of the frequency-doubling phenomenon. Abnormal response is indicative of early glaucomatous loss of vision with a high sensitivity and specificity to glaucomatous damage [21]. Changes in a subject's FDP response has been shown to detect glaucomatous damage up to 4 years prior to standard methods for detecting visual field loss and is among the most promising techniques for early glaucoma detection. A common critique of all visual field tests is that they rely on the subjective response of the patients and are prone to some

associated errors. It is also true that visual field tests are diagnosing the disease based upon degradation in performance after irreparable damage has occurred and therapy is then focused on slowing or halting further damage rather than treating the disease prior to symptomatic presentation. Even the best visual field tests are measuring changes that present after changes in the physiology during the late asymptomatic phase of the disease continuum as shown in figure 1.3.

1.2.4.2 Retinal evaluation

There are several imaging techniques that are used to make an assessment of the ONH and RNFL health. In addition to standard fundus photography, advances within the last decade have led to increasing use of confocal laser scanning tomography (CLST), scanning laser polarimetry (SLP) and OCT [22]. These techniques have overlapping functionality but allow a clinician to visualize different parameters to assist in the clinical determination of glaucoma, primarily optic disc size and shape and RNFL thickness. The RNFL thickness measurement is most often performed using either SLP[3] or OCT [23, 24] and there is evidence that the thinning of the RNFL occurs up to 6 years prior to measurable changes in standard visual field techniques [25]. Optic disc changes, measured with OCT or CLST, such as cup-to-disc ratio and optic disk area are also used to identify glaucoma. Several studies have tested these methods against each other, but

[3] SLP is not strictly an imaging technique and allows only the measurement of RNFL thickness deduced from the phase retardation of the RNFL layer with an assumed value for the RNFL birefringence.

there has been no definitive demonstration of the superiority of any of these techniques [22, 26-30].

1.3 Optical Coherence Tomography

Since the time of its introduction in 1991 [31], OCT has gained widespread adoption in ophthalmology as well as numerous other medical applications. Zeiss Meditec, the first company to commercialize an OCT system for ophthalmology, reported in 2008 that they had installed 10,000 of their OCT ophthalmology systems worldwide since 1995; 80% of these systems are the Stratus OCT system first available in 2002 [32]. This number continues to grow as the technology and applications advance. In the past few years, Zeiss and several competitors have received FDA approval for the newer generation of OCT with orders of magnitude improvements in imaging speed and resolution. In academia, as well, there has been an acceleration of research in OCT since it's introduction as evidenced by the growing number of publications; over 1600 papers published in 2009 are listed on the Web of Science database with keywords "optical coherence tomography." These papers include both development of the technology as well as applications for the technology, and the sheer volume of publications demonstrate the enormous interest that OCT continues to develop as well as the huge range of research that has opened up as a result of this technology. OCT speed, resolution, and image quality all continue to advance on the heels of improvements in light sources,

computing power, and image processing. This is driven by a clear demand for a technology with the strengths of OCT in a variety of biological applications.

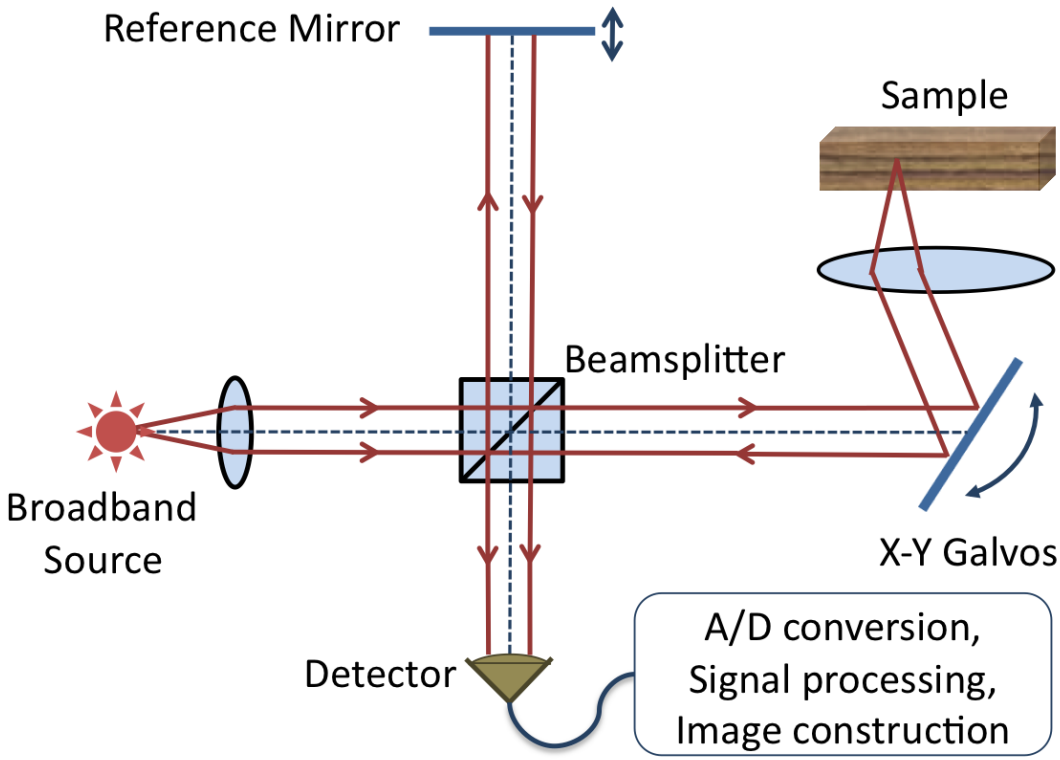

Figure 1.4. Simple diagram of an OCT optical system comprised of a source, beamsplitter, reference and sample arm optics, and a detector.

1.3.2 OCT overview

OCT is an optical imaging modality that allows the recording of depth resolved profiles (A-scans) of light backscattered from a sample. OCT is referred to as an optical histology method because of the high-resolution cross-section images that it generates

non-invasively. A close analog to OCT is ultrasound imaging which measures sound reflected from tissue and localizes the reflections based on a time-of-flight measurement to reconstruct cross-sectional images. Rather than a time-of-flight measurement, which is prohibitively short at the scale of most biological systems, OCT technology utilizes a technique known as optical reflectometry to localize backscattered light within the tissue through coherence gating. In this technique, low-coherence broadband light is separated into two paths, a sample path and a reference path. The backscattered light from the sample is interfered with light in the reference path. The interference frequency depends on the optical path length (OPL) difference of light propagating in the two paths. Analyzing the interference signal from light scattered in a multilayered sample to extract the OPL information allows reconstruction of the depth-resolved reflectance profile (A-scan[4]). By scanning the incident light laterally across a sample, a collection of these A-scans generates two-dimensional images (B-scan). These B-scans are collected for a volume of tissue to give a tomographic image. The scans have axial resolution, depending on the bandwidth of the source, down to a few micrometers and a lateral resolution equivalent to a standard optical imaging system. The maximum imaging depth is tied to the coherence length of the source, but in highly scattering biological tissues, with blood and water absorption, the practical imaging depth is typically limited to 1-3 mm.

[4] The terms "A-scan", referring to a depth-wise reflectance profile, and "B-scan", referring to a linearly spaced collection of A-scans, are inherited from ultrasound imaging.

1.3.3 OCT Implementations

OCT can be implemented in a variety of ways. Time-domain OCT (TD-OCT) was the first implementation of OCT [31] and it was enormously successful, as evidenced by Zeiss Meditec's successful commercialization of ophthalmologic imaging systems described above most of which was accomplished with this type of technology. In TD-OCT, the source is a continuous low-coherence broadband light source, typically a super-luminescent diode or broadband laser source. Interference fringes for different depths in the tissue are recorded serially by means of a scanning reference arm. This type of implementation has two key limitations, namely that it requires frequent rapid scanning of the reference arm path length and it is a point-sampling technique, both contributing to the key limitation in its speed. This technique has been replaced almost completely in the last 10 years with much faster implementations of OCT in the frequency domain (FD-OCT) and as a result TD-OCT will not be fully described here.

Frequency domain techniques for OCT were first introduced as a way to measure intraocular distances in 1995 [33]. This concept was further developed and put into practice for imaging in 1997 [34]. In FD-OCT, the reference arm is fixed and the light source is dispersed to allow spectral readout of the optical frequencies of the light. Path length differences, each with its own optical frequency interference pattern, between the reference and sample paths are encoded in this spectral information. A Fourier transform of this interference signal produces an a-scan. The measured intensity (I) of an

interferogram from the reference (I_r) and sample (I_s) arms for an a-scan measured with spectral detection can be described as follows[35]:

$$I(k) = I_r(k) + 2\sqrt{I_s(k)I_r(k)}\sum_n a_n \cos(kz_n) + I_s(k) \qquad (1.1)$$

In this equation, k is the optical frequency ($k = 2\pi/\lambda$) and α is the square root of the reflectivity values for different depths (z). The depth dependence in the middle term of this equation gives a modulation to the source spectrum. A single depth reflection from a mirror or other plane reflector will give a constant modulation in k-space. Acquisition of the interferogram signal for a broadband source allows the depth information to be retrieved typically with power spectral density analysis. The key advantage of this technique is that rather than being a point sampling technique, it is a line-sampling technique and enables the detection of a-scans at rates several orders of magnitude more quickly than TD-OCT.

FD-OCT is further classified as spectral domain (SD-OCT) or swept source (SS-OCT). The distinction between these techniques is the method of dispersing the optical frequencies for detection in the frequency domain. In SD-OCT, the frequencies are dispersed spatially, typically through a grating, into a line and detected simultaneously as with a line-scan CCD. SS-OCT dispersed the wavelengths in time and they are detected serially. There are advantages to both of these fourier domain techniques that will not be detailed here, but the process is very similar once the data has been acquired as a collection of optical frequencies.

Using these techniques, it is now possible image many dynamic biological processes, collecting a-scans at rates of 100's of kilohertz, generating many thousands of images per second. At these rates, there are still many difficulties in processing, storing and displaying these large amounts of data, but innovation continues to improve processing techniques, acquisition techniques, and computing power.

Chapter 2: Swept Source Polarization Sensitive Optical Coherence Tomography

2.1 Overview

A primarily bulk-optic PS-OCT instrument was designed and constructed to measure intensities in horizontal and vertical polarization states reflected from a sample. This system was designed primarily for imaging retina in primates. For description, the system is divided into the optical, electrical, and software components. Significant effort was devoted to optimizing the performance of several of the key components and this is detailed within the description.

2.2 Optical configuration

In this chapter we present a PS-OCT system using a 1 um wavelength source. This system utilizes a unique clocking scheme that allows the data to be acquired in k-space, eliminating the need for a processing intensive interpolation step. Separate polarization channels are detected simultaneously and the initial polarization state impinging on the sample is controlled by means of a customized electro-optic phase modulator. This system has been used to collect three-dimensional image scans in nonhuman primates as well as polarization maps around the ONH. The OCT system components are presented sequentially as an interferometer with a source arm, reference and sample arms, and a detection arm, followed by a description of the k-space clock a separate optical interferometer circuit that is used to generate the timing signal for data acquisition. This system has shown the ability to

generate OCT images at a 28kHz A-scan rate, where an A-scan is one depth scan or one column in a full B-scan (cross-section) image. A system schematic is shown in figure 2.1 below.

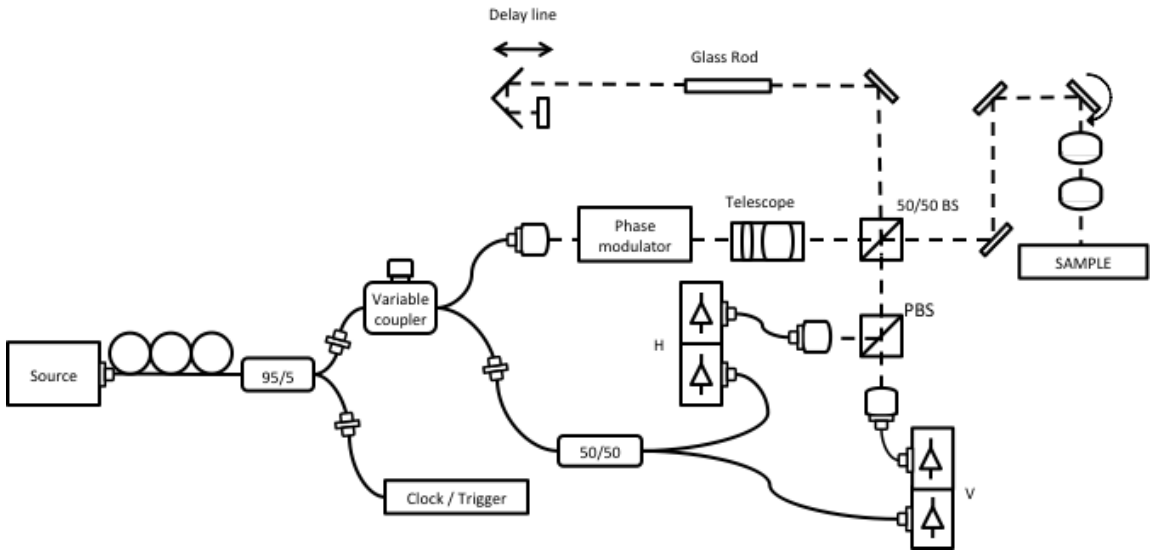

Figure 2.1. OCT system schematic, PC: polarization controller, PBS: polarizing beam splitter. Clock schematic is shown in separate figure below.

2.2.2 Laser Source

The source is a swept source laser (HSL 1000, Santec, Komaki Aichi, JP) centered at λ=1064 nm, a full width half max (FWHM) bandwidth of 60nm and a duty cycle of 64% with a 28kHz repetition rate. The swept-source laser sweeps through a range of optical frequencies and repeats the sweep at a rate of 28kHz. This source has a coherence length of 4 mm, defining the maximum imaging depth or the maximum path length mismatch that will still interfere. This maximum imaging depth is further limited by the spectral resolution of the detection scheme.

$$z_{max} = \frac{\lambda_0^2}{4n\delta\lambda} \tag{2.1}$$

The 60nm bandwidth of the source dictates the maximum axial resolution that is achievable. Assuming a Gaussian distribution, the maximum axial resolution is:

$$\Delta l = \left(\frac{2ln2}{\pi}\right) * \left(\frac{\lambda_o^2}{\Delta\lambda}\right) \tag{2.2}$$

From equation f(2.2), we calculate a maximum axial resolution of 8.3 um in air.

The light output from the source is fiber coupled and immediately passes through a 95/5 fiber optic beam splitter, which takes 5% of the light for the trigger and clock. Next is an adjustable ratio fiber optic coupler from Canadian Instrumentation and Research. This coupler is used to adjust the amount of light transmitted directly to the detection path to allow balance detection (as discussed below). The remaining light is collimated using an aspheric lens (OFR, Caldwell , NJ) and polarized linearly with a Glan-Thomson polarizer (Karl-Lambrecht, Chicago, IL), oriented at 45^o relative to the lab frame. The light output is fairly well polarized from the source, but this polarizer removes any unpolarized light and more importantly allows orientation of the light relative to the lab frame. Prior to the polarizer, there is an inline polarization controller and this is used to align the primary polarization output from the laser to match the polarizer and maximize the amount of light through the polarizer.

2.2.3 Phase Modulator

In order to control the sample input polarization state, a phase modulator is placed in the source beam path, following the linear polarizer. A voltage applied to this modulator introduces a phase delay between two orthogonal polarization states of up to +/- 120^{o} at a frequency up to 100 Mhz. The modulator is comprised of two 20mm long MgO:$LiNbO_3$ crystals with a 2mm clear aperture. This modulator is a modified commercially available model (4004, New Focus, Santa Clara, CA) and is driven by a high-voltage amplifier (3211, New Focus, Santa Clara, CA).

The crystals in this modulator are set up as a Pockels cell, which is a voltage-controlled waveplate. In this Pockels cell, an electric field applied transverse to the direction of propagation of the light introduces a birefringence to the crystal. The change in the birefringence in the electro-optic crystal introduces a phase delay between light oscillations along two orthogonal axes (fast and slow). By orienting the optic axis of the cell at 45^{o} to the input polarization state, equal amplitudes of the light propagate in the fast and slow axes of the crystal and any elliptical polarization state can be achieved by retarding one polarization relative to the other.

We use three input polarization states selected in order to avoid having a case where the eigen-polarization vectors in the RNFL are at 45^{0} relative to the lab frame H and V states. If this were to be the case, the detected signals would have no phase difference and we would not measure any birefringence.

Following the modulator, the beam is expanded in a simple optical telescope for propagation through the rest of the system. The beam diameter is roughly 1.6 mm at the exit of the telescope.

2.2.3.1 Modulator ghost line removal

A single electro-optic crystal typically has a very high value for native birefringence, before the applied voltage, which is undesirable in this and many applications. In order to remove the native birefringence, there are a few options. One is to precisely machine the crystal so that the retardation is an integer multiple of a wave, bringing the waves back into phase with one another. A similar effect could be achieved by applying a constant offset voltage to re-align the phases. Both of these techniques suffer from the shortcoming that the birefringence is wavelength dependent and therefore either technique would only be accurate for a single wavelength rather than the entire range in our broadband source. The final common technique, used in this application, is to utilize two crystals in series with the second rotated 90^{o} relative to the first. In this way the light propagating along the fast axis of the first crystal propagates in the slow axis of the second crystal (fast→slow) and vice versa (slow→fast), so that both polarizations acquire the same retardation and are output in phase. Voltage applied transverse to one of these axes, changes the birefringence and if applied across the same axis in each the retardation is doubled. The shortcomings of this approach for removing the native birefringence are mainly mechanical. If the crystals are not precisely cut to the same length, there will be imperfect removal of birefringence. In addition, the

more serious problem with this technique is that if the crystals are not precisely aligned at 90^o there will be some cross-coupled light.

This cross-coupled light, where fast axis light in the first crystal is coupled to the fast axis light in the second crystal (fast-fast) acquires a double phase retardation, similarly the slow axis light (slow-slow). When another polarizing element is placed in the beam path, this retarded light interferes with the primary light. With a broadband light such as is used in OCT, this causes a signal modulation due to the interference were the interference frequency is related to the length of the phase retardation. This shows up as a "ghost line" in OCT, an imaging artifact at a fixed depth in the image.

The Sellmeier equation describes the index of refraction for a given wavelength in a material:

$$n^2 = 1 + \sum_j \frac{A_j * \lambda^2}{(\lambda^2 - B_j)} \tag{2.3}$$

The parameters in this equation are experimentally determined and computed to give the best predictive accuracy for a given set of wavelengths. The values used for MgO doped $LiNbO_3$ are presented in table 2.1.

Table 2.1 Sellmeier coefficients for 5% MgO doped LiNbO3 crystal [36]

Coefficient	N_o	N_e
A_1	2.4272	2.2454
B_1	0.0148	0.0124
A_2	1.4617	1.3005
B_2	0.0561	0.0531
A_3	9.6536	6.8972
B_3	371.2160	331.3300

The Sellmeier equation gives $n_o = 2.229$ and $n_e = 2.147$ for the two propagation axes in the crystal at the center wavelength of the laser source. The retardation (Γ) acquired by the fast-fast coupled light can be described simply by the difference in the index of refraction between the two axes (Δn) and the length of the crystals (d):

$$\Gamma = \Delta n * d \tag{2.4}$$

From equation (2.4) we compute that for the 20 mm crystals, with Δn = 0.0815, from the Sellmeier equation above (2.3), there is a path length change of 1.6 mm. This is in single pass while the image length is in double pass meaning that the ghost line shows up at half of this length at 0.8 mm relative to the imaging depth.

2.2.3.2 Modulator modification

We discovered that the modulator, as supplied commercially introduced a significant "ghost line" at the predicted location in the OCT images. The modulator has no mechanical adjustment to control the relative crystal rotation so we modified the mechanical design to tilt the crystals and remove the ghost line from recorded images. To perform this modification, we removed the crystal mount from the original box and cut the crystal mount in half. We attached the parts to a custom built mount with separate cantilevered tilts that are controlled using a screw pushing against the solid base. This mount was made so that it would fit back inside the original box with minor modifications. Electrical conductivity through the box, which serves as the ground for the voltage applied to the crystals, was maintained by reattaching the parts with electrically conductive epoxy.

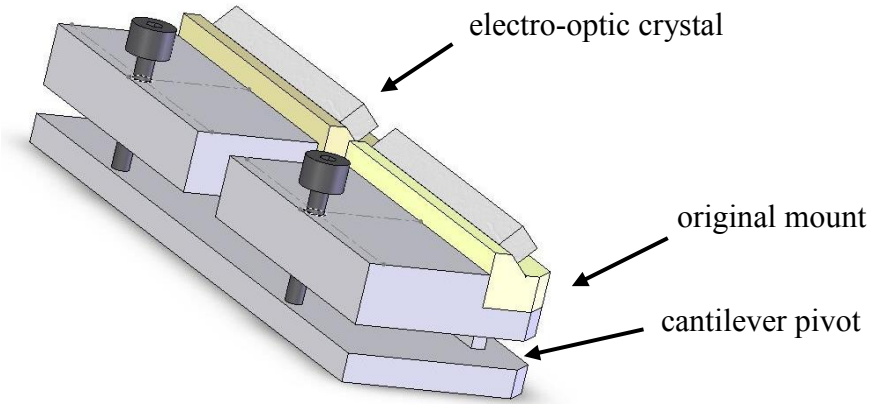

Figure 2.2. Modified modulator rotation mount for precise crystal alignment. Two independent cantilevers allow relative rotation of crystals. The original mount (in gold) was divided and attached to the new mount, maintaining the crystal's electrodes that are epoxied to the original mount.

As can be see in figure 2.3 below the modulator adjustment was made to reduce the strength of the ghost line to the level of the noise in the image. At this level, the ghost line continues to be visible in the images, but it is much less of a problem because it doesn't dominate the brightness of the image, obscure the features around it, or add excessive noise and harmonics by saturating the detectors.

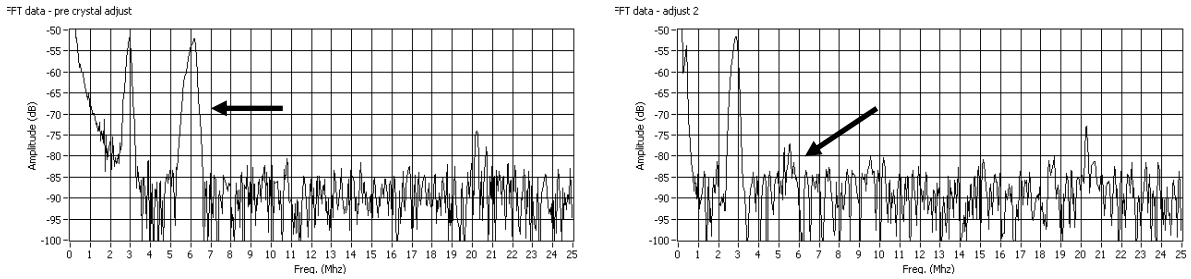

Figure 2.3. FFT of interference signal from modulator before and after fine adjustment. The line at 3 MHz results from multiple reflections in a window covering the photodiode in the detector. The signal at 5-6 Mhz is due to the crystal rotational misalignment and is reduced to close to the noise level after adjustment.

2.2.3.3 Modulator setup

Care is taken in aligning and calibrating the modulator to achieve precise polarization control. The modulator is first aligned to the laser beam to achieve maximum extinction ratio, ensuring the maximum cancellation of native birefringence between the two crystals. The procedure for this is to use a polarizer on the input and output as a polarizer and analyzer, with the modulator between them as shown below in figure 2.4. The polarizer is aligned with the optic axis of the crystals, in this case at 45^{o} relative to the lab frame. Aligning the second polarizer in the position of an analyzer, at 90^{o} relative to the first polarizer, the ideal case would have no light throughput and perfect extinction of the light. The modulator, mounted on a 5-axis (tip, tilt, x, y, rotation) stage is adjusted to minimize the light throughput. With this setup, an extinction ratio (uncrossed polarizer throughput / crossed polarizer throughput) of 40 was achieved.

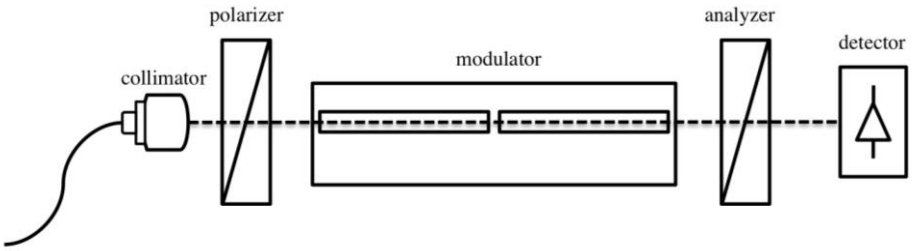

Figure 2.4. Optical setup for modulator alignment and calibration.

Once the modulator is aligned, it is then calibrated to achieve the desired retardation. Calibration is done with the modulator set up as an amplitude modulator, again with crossed polarizers on the input and output. The retardation (Γ) for an electro-optic crystal is linearly dependent on applied voltage.

$$\Gamma = \Gamma_o - \pi\frac{V}{V_\pi}, \text{ where } \Gamma_o = \frac{2\pi}{\lambda_o}(n_1 - n_2)L \quad (2.5)$$

Here the V_π is the wavelength dependent voltage for a retardation of π radians, and n is the index of refraction for one of the two crystal axes. Rotating the second crystal at 90° relative to the first cancels the native retardation (Γ_o) so that:

$$\Gamma = -\pi\frac{V}{V_\pi} \quad (2.6)$$

With crossed polarizers, this gives transmission intensity:

$$T = \sin^2\left(\frac{\Gamma}{2}\right) = sin^2\left(-\frac{\pi}{2}\frac{V}{V_\pi}\right) \quad (2.7)$$

By acquiring a reference signal with uncrossed polarizers, generating the target signal for the output at a desired retardation is straightforward. The reference signal is used to calculate the target signal at a given retardation using equation (2.7).

Because V_π is wavelength dependent, the signal sent to the modulator is not a constant voltage for each state, but is varied with the wavelength of the incident light, in this case a constant ramp is applied during the laser output period. In this application, three polarization states are used (-120°, 0°, 120°) with switching occurring between subsequent A-scans requiring a crystal voltage of ±200V. This high voltage at the high switching rates causes a hysteresis effect in the amplifier. To correct for this, the voltage array is adjusted while modulating at the rate used during imaging. The modulation is triggered to sync the beginning of each ramp at the laser sweep rate and output the ramp voltages at a constant clock rate during the sweep. A user adjusted voltage array, defining the start and ending

voltage for the ramp, is adjusted to minimize the error from the theoretical target signal, which is displayed in real time as it is acquired with a digitizer.

2.2.4 Beamsplitter

It is of utmost importance to maintain maximum return of signal light from the sample. In this type of interferometer, this is best achieved using a 50/50 beamsplitter. The beamsplitter selection is made more important by the need to have neutrality with respect to polarization. A 50/50 cube beamsplitter is made of two 45^{o} wedges of glass cemented together with a dichroic layer between them to select the wavelengths and proportion to reflect. This material and thickness of the dichroic layer can have strong wavelength and polarization dependence. We tested several beamsplitters to get optimal splitting at this wavelength for both polarizations.

To test the beamsplitter quality, fringes were acquired from a simple interferometer using a mirror on two output faces of the beamsplitter and a detector on the return path. Utilizing a mirror on the output faces of the interferometer allowed the beamsplitter effect on the polarization to be isolated from the other optical components. These fringes were acquired for both polarizations using the polarizing beamsplitter and fiber coupling used in the complete PS-OCT system and using the linear k-space clock giving data points equally spaced in optical frequency.

The original beamsplitter, purchased from Reynard Optics, displayed significant polarization artifacts because the split ratio and phase delay was highly polarization

dependent. This data was plotted as the complex polarization ratio (CPR). On the complex polar plane, the analytic phase difference between the polarizations is plotted as theta and the amplitude ratio is plotted as r. Multiple points are plotted as the laser outputs varying optical frequencies. Ideally, the phase difference should be zero and the amplitude ratio should be unity.

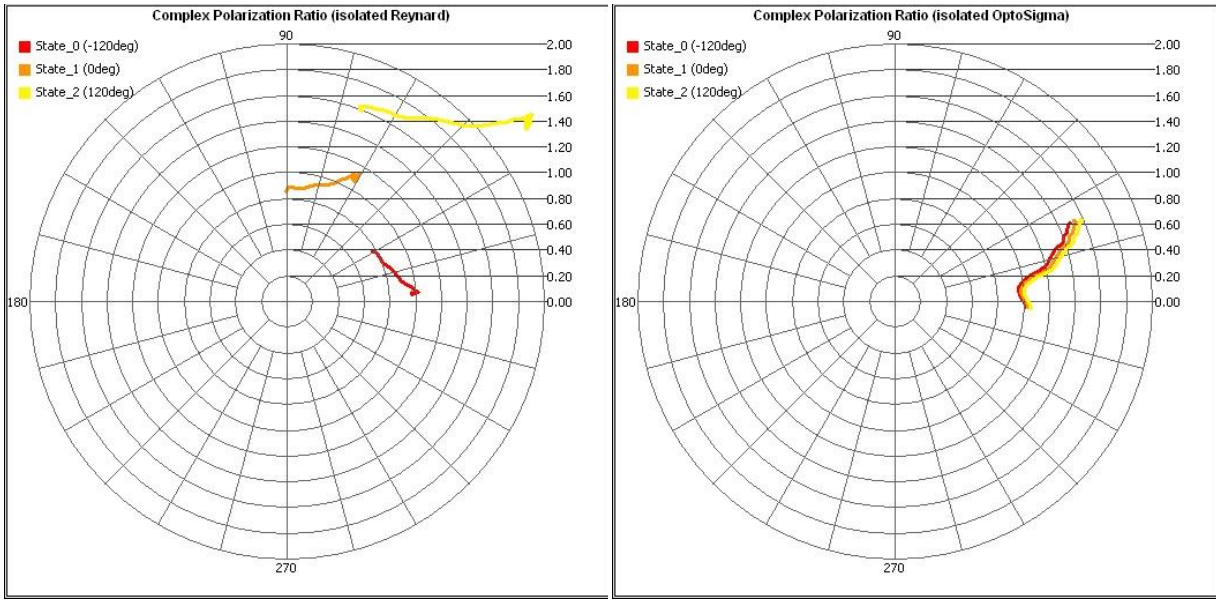

Figure 2.5. CPR representation of interference fringes in a simple interferometer with original beamsplitter (left). Three input polarization states give three widely varying phase and amplitude ratio values. CPR representation for replacement beamsplitter (right) showing good agreement between amplitude and phase for the three input polarization states.

The original beamsplitter used in this system showed significant variation in the phase and amplitude ratio depending on the input polarization state. We identified a beamsplitter (OptoSigma 039-0265, Santa Ana, CA) that had much better characteristics for polarization insensitivity giving close agreement between the CPR for three input polarization states as shown in figure 2.5. In this case, there is a fixed offset in the fringe frequency, but it is constant between the states.

2.2.5 Reference path

A 50/50 beamsplitter (Optosigma, Santa Ana, CA) splits the light into sample and reference paths. The reference path is double pass and a delay line was constructed to match the OPL with the sample path. This delay line is comprised of a corner cube retroreflector (Optosigma, Santa Ana, CA) mounted on a motorized stage (Zaber, Vancouver, BC). The motorized stage is controlled either manually or remotely through a serial port on the computer.

The remaining element in the reference path is a glass rod to balance the dispersion from the sample path lenses. Dispersion does not cause significant problems in interfering systems such as this, provided it is balanced between the two paths.

2.2.6 Sample path

Sample optics in the PS-OCT system shown in figure 2.6 include 3 silver coated mirrors, X- and Y- scanning galvanometer mirrors, and a triplet lens pair. Two silver coated mirrors act as a periscope to raise the beam and provide clearance for the primate in the sample path and direct the beam to the first galvanometer. The X- and Y- scanning galvanometers are mounted in orthogonal planes to provide beam steering in two lateral dimensions. The triplet lens pair is set up in an afocal configuration. The back focal length is set between the two galvos and this lens converts the angular deflection of the galvos into a lateral beam displacement in the lens image plane. This image plane is placed in the back focal plane of the second triplet lens to complete an afocal system with unity magnification.

This second lens recollimates the light and converts the lateral displacement of the beam into an angular deflection so that the beam pivots around the focal plane of this second triplet lens. The effect of this is that for ocular scanning, the beam will pivot about the cornea and allow the beam to be scanned across the retina without clipping on the pupil. For imaging non-ocular specimen, a focusing lens may be placed with the pivot point at the back focal plane of the focusing lens to maintain a flat imaging field.

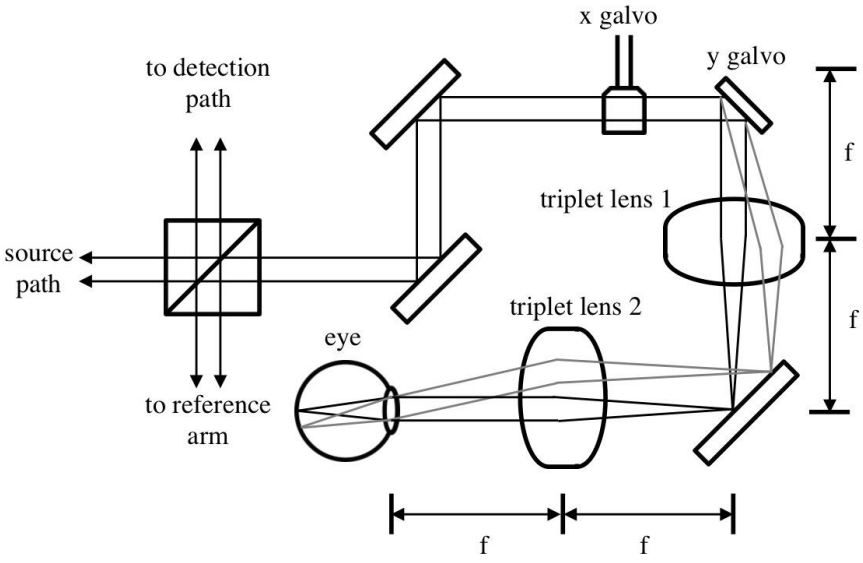

Figure 2.6. Sample optics in PSOCT system for ocular imaging.

2.2.6.2 Dispersion balancing

The optical elements in the sample arm introduce dispersion with a double pass to and from the imaging sample. This dispersion arises primarily from the two large optical length triplet lenses, with multiple glass types. This dispersion must be either compensated for in post-processing or balanced in the reference arm. The dispersion mismatch was measured using a single reflection from a mirror on the output of the sample optics.

To analyze this signal, a Hilbert transform was used to extract the analytic phase of the signal. This signal was acquired with the linear k-space clock discussed below so that sampling was done with equal spacing in optical frequency. In the optimal case with zero-dispersion and using a linear k-space clock, the analytic phase would be linear and the slope would be proportional to the path length mismatch. To isolate the effect of dispersion, the analytic phase of the acquired signal was fit with a line and the residual was taken as the dispersion effect. This analysis showed a phase difference range of almost 4π over the full range of optical frequencies.

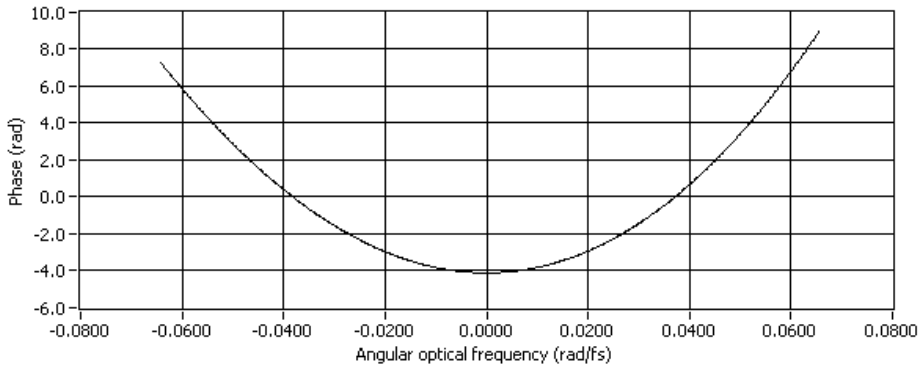

Figure 2.7. Dispersion effect on fringe interference pattern phase over the source output spectrum.

Using this analysis, we were able to quantify and remove, in software, the dispersion effects in the images. The dispersion curve was fit with a cubic polynomial to generate a mathematical description of the dispersion. Once this description was obtained, it was used in subsequent imaging experiments. To do this, the analytic phase was computed for each A-scan with a Hilbert transform. The measured phase error was subtracted from the analytic phase and the inverse Hilbert trasform was performed. The result from this was a dispersion corrected signal in optical frequency or k-space. This signal was then processed normally to

transform the signal into the time-delay domain or time domain. This method improved the signal peak level by 11 db and the signal to noise ratio (SNR) by 5 db. Clearly this improved the signal significantly, although the noise level increased due primarily due to the multiple FFT calculations needed to implement this correction. The resolution increased from 47 μm to 16.5μm. The difference in image quality were dramatic as shown in figure 2.8.

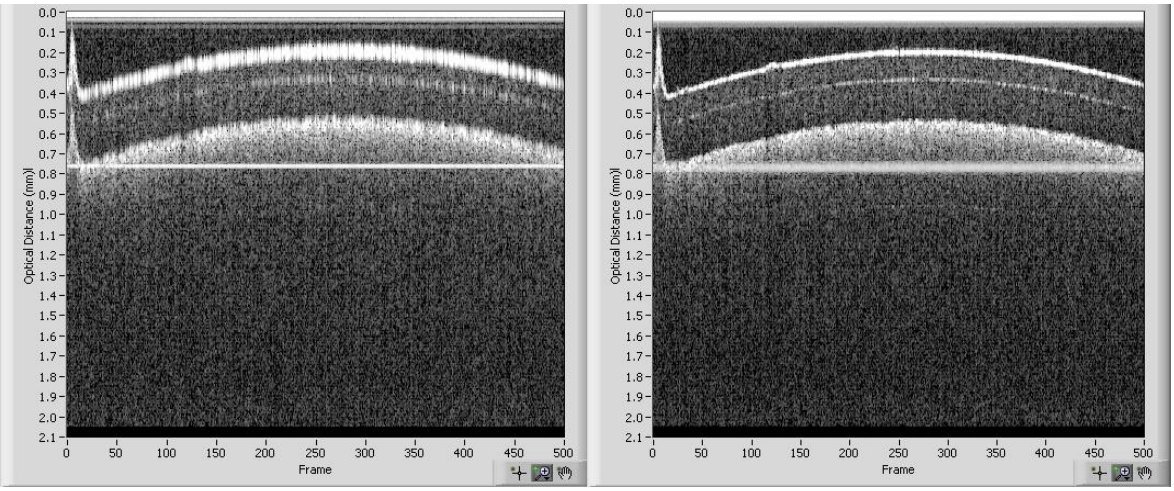

Figure 2.8. Image of plastic fluorescent IR card without and with software phase correction.

This software correction required multiple FFT calculations to implement and consequently increased the processing time considerably so it was never considered a long term solution. A glass rod was obtained from the manufacturer of the triplet lenses with identical glass types and dimensions, although no curvature, to compensate for the dispersion in the reference arm. This glass rod was placed in the reference path, where the light passes through in double pass to balance the dispersion in the reference arm with that of the sample path. This achieved the same effect in signal and resolution improvement without raising the noise floor.

2.2.7 Detection Path

The sample path, in double pass, collects backscattered light from the sample and this interferes with the reference light back at the main 50/50 beamsplitter. The interfered light is then reflected towards the detection path. As shown below in figure 2.9, this light is then separated into two orthogonal polarization states with a polarizing beam splitter (PSCLB-YAG, Thorlabs, Newton, NJ). The polarizing beam splitter (PBS) reflects the vertical polarization and transmits the horizontal polarization. Two matched collimators (PAF-X-5-B, Thorlabs, Newton, NJ) collect the light and couple it into the fiber for transmission to the detectors. In this setup, the fibers act as pinholes to remove reflected light that is not interfered. The signal is then detected in two balanced photoreceivers (1817-FC, New Focus, San Jose, CA). The balanced signal is formed by a differential detection technique to remove random intensity noise (RIN) originating in the laser source and to remove the DC level of the signal to preserve the dynamic range of the detection channel.

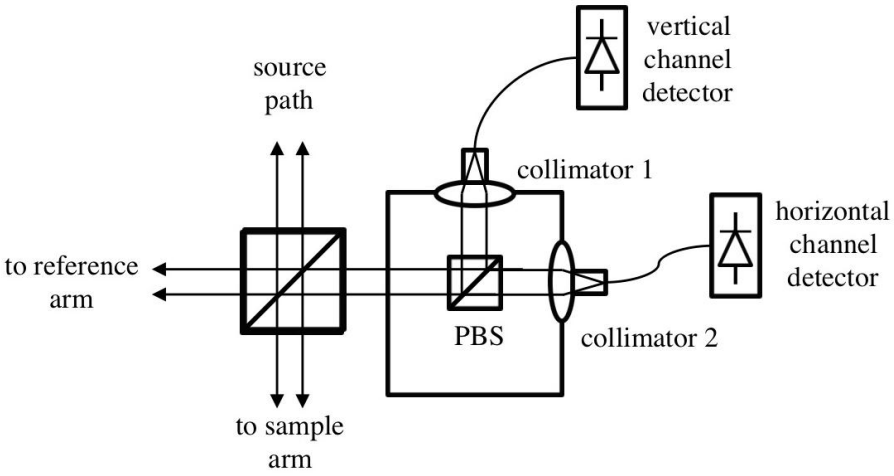

Figure 2.9. Detection path optics consisting of main 50/50 beam splitter, polarizing beam splitter (PBS), matched collimators, and photodetectors. Not shown are the 2nd channel of the balanced photoreceivers. This second channel for each consist of a fiber running from the laser source, through three fiber optic couplers to the negative channel for the photoreceivers.

2.3 LINEAR K-SPACE CLOCK

Time variation of the output from the swept source laser is nonlinear in wavenumber ($k = 2\pi/\lambda$). Because the Fourier transform into the time-delay domain assumes a linear wavenumber or k-space signal, a non-linear sweep gives rise to major image artifacts requiring correction. The typical correction methods either acquire a calibration signal serially or in parallel to use for resampling the data in linear k-space.

2.3.1 Source non-linearity

The non-linearity of the sweep for our laser can be seen in fringes generated in a Mach-Zender interferometer, where the light is separated into two paths with a slight length mismatch and then recombined. With a broadband laser, this generates an interference

signal that oscillates at a single frequency in k-space and thus has a linear analytic phase. To diagnose the non-linearity of the laser source in the PS-OCT system we acquired an interferogram signal with a fixed sampling rate and took the Hilbert transform to find the analytic phase. The derivative of the analytic phase is the angular frequency of the interference fringes. This would be a constant slope line in the ideal case, so the linear portion was subtracted to isolate the non-linearity of the frequency. The 3 MHz variation shown below in figure 2.10 is for a center frequency of 22 Mhz fringe frequency, which works out to a path length difference of 5.4 mm in air for this source. The effect of this non-linearity is that if the signal is acquired with a constant frequency clock, resolution is lost. Because the frequency variation scales as a multiple of the linear frequency, the effect gets worse with higher frequencies or deeper imaging depths. In this case, at a 5.4 mm path length mismatch the total line width is 600 μm while the theoretical axial resolution for this source should be 6.7 μm.

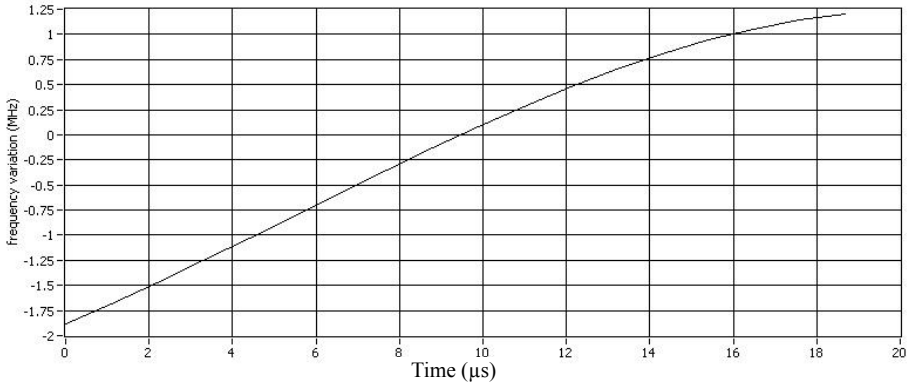

Figure 2.10. Plot of the time variation in the clock frequency due to the non-linear k-space output. This contributes to degradation in image quality if using a linear acquisition clock.

2.3.2 Real-time quadrupled k-space clock

For our system we developed a method to acquire the OCT fringe data linearly in k-space by using a "k-space clock". The k-space clock has been implemented in two ways. Originally, we acquired a reference signal from a single optical path length (OPL) mismatch, digitally processed the signal, and used an arbitrary function generator to reproduce this processed clock signal. Some concern was raised about the phase stability of this reproduced clock method for polarization sensitive measurements since considerable jitter exists in the laser trigger due to sweep-to-sweep power fluctuations. As a result, the method was developed further to use a separate real-time clocking interferometer with the even in k-space pulsed generated in real-time.

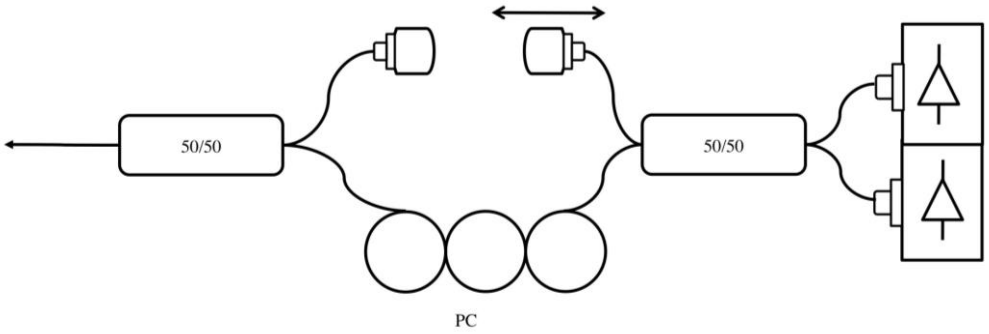

Figure 2.11. Mach-zender interferometer used for generating a fixed frequency interference signal for k-space clock. This optical circuit consists of two 50/50 fiber couplers, a polarization cotroller (PC) to match the polarizations between the two arms, and a balanced photoreceiver.

The interference signal from a simple Mach-Zender interferometer shown in figure 2.11 is processed in an analog circuit and used as the clocking signal for the signal acquisition. The potential downside of using this approach is that the light output has a limited coherence length, meaning that the visibility of the fringes generated in the

Mach-Zender interferometer is reduced at high frequencies and will eventually the two paths will no longer interfere. The implications of this limitation are that generating the clock according to the Nyquist frequency uses up half of the available source coherence because the measurable frequencies are limited to half of the clock frequency.

In order to avoid this limitation, an analog circuit was designed to quadruple the fringe frequency and obtain the maximum imaging depth from utilizing the full extent of the coherence length. The electrical circuit (diagram shown below in figure 2.12) consists mainly of two stages where the signal is amplified then rectified and balanced about ground to quadruple the signal frequency. The clock output switches between the filtered k-space clock and an oscillator approximately matched to the clock frequency in order to present a consistent clock signal to the acquisition board. This switching is timed with the trigger signal and a time delay programmed into the digital delay generator to correspond with the end of the A-scan to ensure that the fringe data is clocked with the non-linear k-space clock and the oscillator is providing timing pulses during the off period in the laser duty cycle.

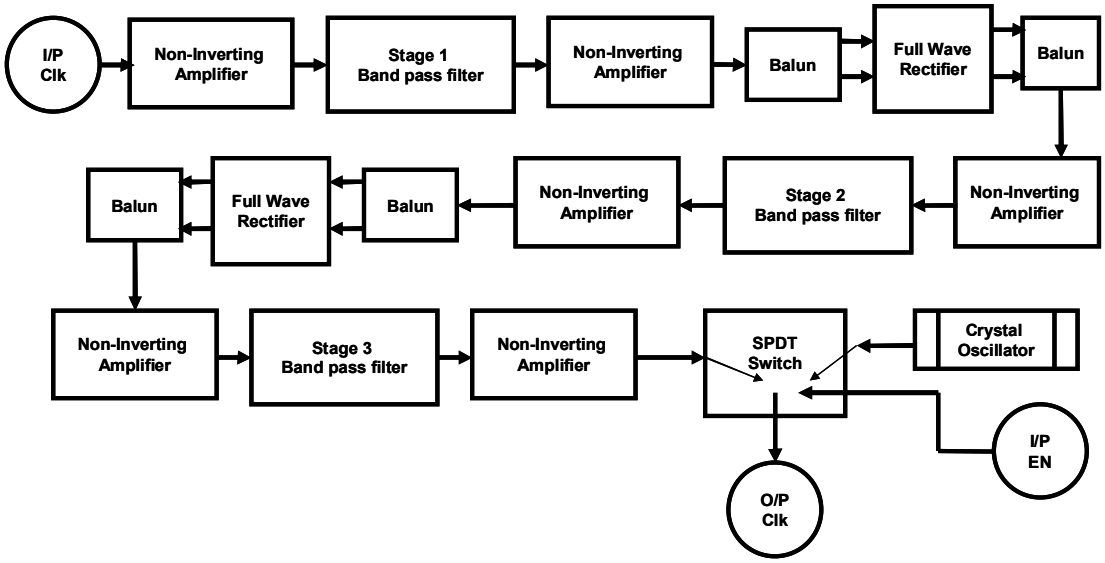

Figure 2.12. Block diagram of the circuit used to quadruple the fringe frequency and generate a clocking signal for the data acquisition [37].

2.3.3 K-space clock frequency

In the process of optimizing the system and designing the k-space clock, we identified a high frequency noise in the laser source. This noise presents as a high frequency fringe signal at 160 Mhz directly out of the laser source. This noise is out of the frequency range of interest in our system; but when sampled at lower frequencies, this signal is aliased down into our system signal and generates a large background noise. We mitigated the influence of this signal in two ways. A built in low-pass filter with a cut-off of 20 Mhz is available on the digitizer and this was implemented. In addition, we identified the sampling frequency that would place the aliased noise at the least disruptive location in the signal. Experimentally, this frequency was decided to be at 40 Mhz and this was the frequency chosen for the k-space clock.

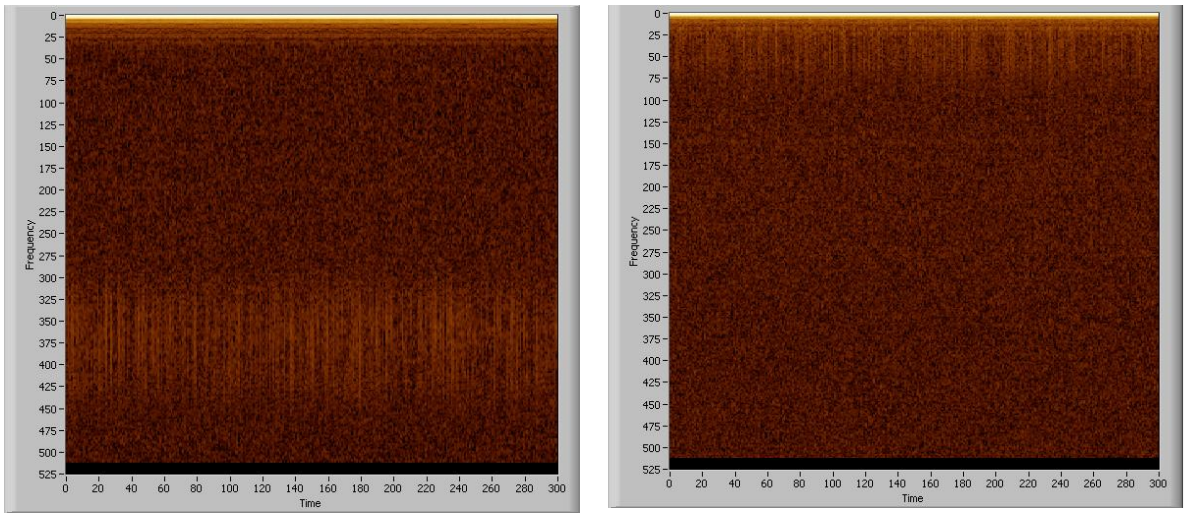

Figure 2.13. Images showing aliased high frequency noise from laser source. The frequency label on the left is of arbitrary units. This is light collected directly from the source so no signal should be present. On left, the data is sampled at a frequency of 30 Mhz and noise shows up in the lower half of the image. On the right, the data is sampled at 39.5 Mhz and the data is placed at the top of the image. The noise is dispersed in both of these images due to the use of a fixed frequency clock. With the k-space clock, the noise ghost image would occupy a much smaller frequency band.

2.4 ELECTRICAL DESCRIPTION OF PS-OCT SYSTEM

The timing and triggering are driven by the A-scan rate, which in turn is driven by the repetition rate of the swept source laser. To do this, an optical fiber with a small fraction of the light separated from the clock optical circuit is detected with a single photodetector. This detected signal is thresholded on a digital delay generator to generate the primary trigger pulse. The coordination scheme for the signal timing is shown below.

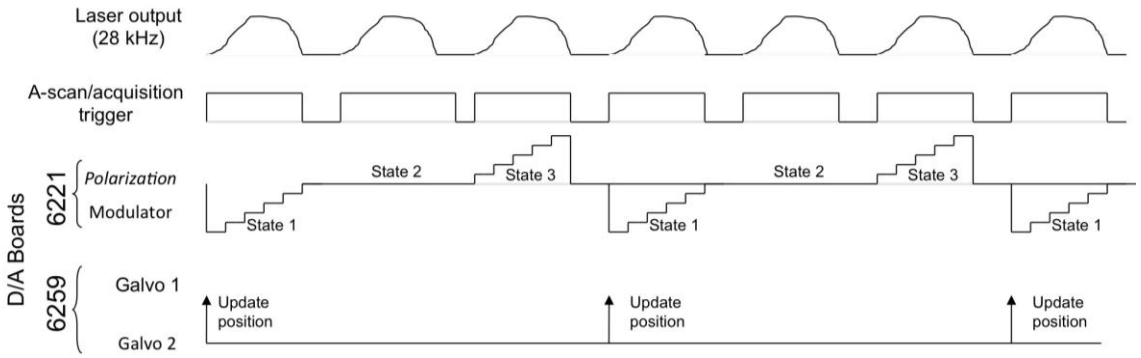

Figure 2.14. Timing diagram showing the various timing pulses that are provided to components in the PS-OCT system.

Digital acquisition of the horizontal (H) and vertical (V) fringes is performed by the acquisition board (ATS-9462, AlazarTech Inc., Pointe-Claire, QC). This two-channel, 16 bit acquisition board has the ability to be clocked externally and has acquisition rates up to 180 Ms/s. In this system, we use an external linear k-space clock described in the following chapter to time the sample acquisition. As supplied from the manufacturer the two channels on the acquisition board were clocked separately by two FPGA's on the board. This scheme caused considerable problems in our application because the two FPGA's, though receiving the same clock signal from the system, sometimes got out of sync even using a relatively clean sine wave clock signal from a function generator. Since we are measuring the phase difference between the two channels, this prevented any usable data from being acquired with any reliability. This was finally resolved with the manufacturer who supplied new firmware for the board to keep the clocks for the two channels synced and make accurate phase-difference measurements possible.

The lateral position of the sample beam is controlled by two single-axis optical scanners (6220h, Cambridge Technologies, Billerica, MA). The signal voltages for both

channels are created and stored in the system memory buffer and output one at a time when a trigger event is recorded. These voltages are output by a D/A converter (NI 6259, National Instruments, Austin, TX) and input to the galvanometer servo driver (Cambridge Technologies, Billerica, MA). The driver controls the angular rotation of the galvos and maintain a linear relationship of voltage to angular displacement. Since a continuous train of trigger pulses are sent by the digital delay generator in response to the laser output, a reproduced trigger signal generated by the acquisition board, during active acquisition only, is used as the trigger signal for the D/A output.

The phase modulator is controlled using a separate A/D board (NI 6221, National Instruments, Austin, TX). There are additional analog outputs channels available on the first A/D board, but the timing requirements for the modulator are different than the galvanometers and each board is only able to use a single clock, making a separate board necessary. Because the electro-optic effect is dependent on wavelength, a voltage calibration is found experimentally to provide a constant modulation with wavelength for each desired state. A fixed length/constant frequency train of voltage values is sent to the high voltage amplifier immediately after each A-scan trigger. The array of voltage values is stored in the A/D card memory and repeats when all three of the states have been output.

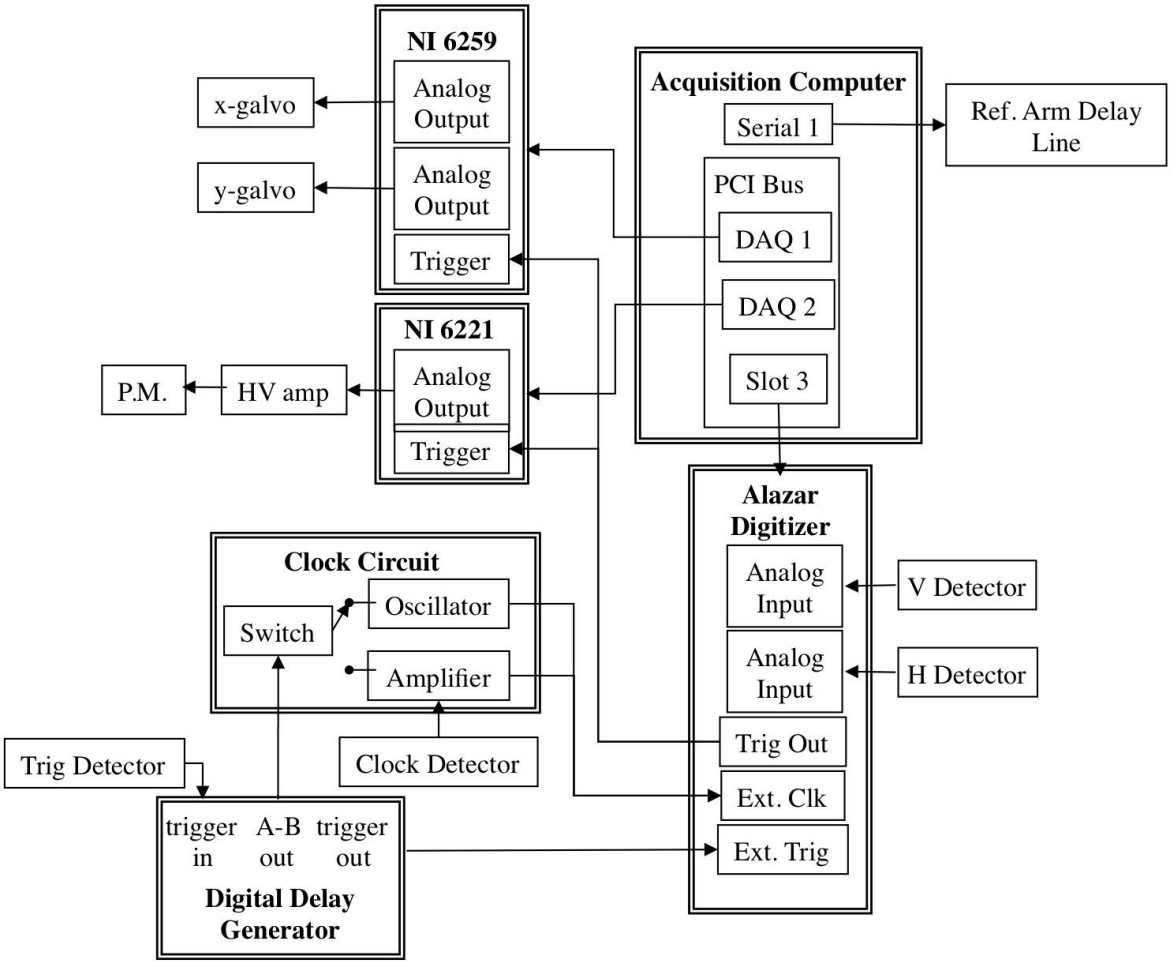

Figure 2.15. Electrical schematic showing the routing of various signals between the electrical components in the PS-OCT system.

2.5 SOFTWARE DESCRIPTION

The software for control and acquisition is written using Labview (Labview v.2009, National Instruments, Austin, TX) with several dynamic linked libraries (dll's) written in C++ to optimize the multithreading and speed of the processor intensive steps. The overall software design is a client-server architecture with three parallel loops running continuously. This approach allows multithreading so that the time-intensive processing steps run continuously in live mode to ensure maximum frame rate display while the acquisition loop can run separately to avoid missing any data.

The first loop, the acquisition loop, controls the instrumentation and acquires the signals. This loop is written as a state machine and the state can be changed via another event loop in response to user input on the screen or in response to software switches. The default state is a continuous data acquisition mode where one B-scan worth of data is acquired into the buffer of the acquisition board and pulled off the board into system memory for every loop iteration. The acquisition loop acts as the server for the processing loop and feeds all the acquired data into a first-in-first-out (FIFO) buffer that is accessed in the processing loop.

The processing loop, which is the client of the acquisition loop, is a continuously running loop that performs a 2-d FFT on complete B-scans. This processing step is one of the primary processor intensive steps and is implemented in a .dll to optimize multi-threading. The raw, unprocessed, B-scan data is either dumped during live imaging mode or streamed to hard-disk during image acquisition for storage and post-processing

depending on a software switch. The processing loop acts as the server for the final, display loop and places the processed B-scan data into a second FIFO buffer.

The display loop is the final client of the software. In this loop, the processed B-scan data is written to the screen for display. The write to screen function is also written as a .dll because it was found that writing via a Labview indicator was sluggish and processor intensive. The processed B-scan data is either dumped from the buffer following this step or is utilized to create an en-face image for display of the overall sample architecture. The en-face image in retinal imaging creates a fundus image that allows visualization of the retina and is used during live imaging for alignment of the eye prior to image acquisition.

Event based programming allows on the fly changes to acquisition or scanning parameters. This software is capable of processing and displaying the data in real-time depending on parameters such as the FFT length and number of A-scans per B-scan. For visualization of the anatomy of the retina, the galvos are programmed to output either a raster scan pattern scanning laterally across the retina or in circular rings centered around the ONH.

When acquiring data for polarization processing, it is necessary to acquire data in clusters to average the phase information and reduce the noise in this measurement. Because the birefringence varies circumferentially and radially around the ONH it is necessary to acquire these clusters in close proximity so that the averaging is enhancing rather than diluting the desired phase information. One of the main contributions to the

noise in the phase measurements is the speckle noise inherent in OCT imaging. This speckle arises from localized interference of the light within the tissue. In order to acquire A-scans in a space where the speckle field is not correlated with the adjacent A-scan, it is necessary to separate A-scans by approximately ½ the spot size. Because we are assuming approximately a 20μm spot size on the retina, depending on the quality of the focus by the cornea, the A-scans within a cluster are separated by approximately 10μm. Our typical cluster scan pattern acquires 18 clusters of 200 A-scans each spaced evenly around the ONH. This is typically done for 10 radially spaced rings to generate a total of 180 birefrigence values in our map of the retinal birefringence.

Chapter 3: EXPERIMENTAL PROTOCOL

3.1 OVERVIEW

PS-OCT measurements were acquired in three macaque primates: two cynomolgus primates (macaca fascicularis), and one rhesus macaque primate (macaca mulatta). One eye in each animal was treated with an argon laser targeting the trabecular meshwork to induce an intraocular pressure (IOP) increase; the fellow eye was left untreated as a control. These animals were followed for a period of 30 weeks during which regular PS-OCT imaging of the retina was performed to assess the changes associated with elevated IOP. All studies performed in this work were done under the direction of The University of Texas Institutional Animal Care and Use Committee and followed an approved protocol (#08013001).

3.2 GLAUCOMA INDUCTION

In order to induce a sustained eye pressure increase and cause glaucoma, we followed an animal model that was first described in 1974 [38] and has been developed and used in many subsequent animal studies on glaucoma [39-41]. All studies performed in this work were done under the direction of the UT IACUC and followed an approved protocol #08013001.

Photocoagulation therapy is an accepted form of treatment for treatment of open-angle glaucoma to lower the intra-ocular eye pressure. A similar procedure is followed for glaucoma induction, except a higher laser power is delivered and a more complete

circumference of the eye is ablated with the laser. For this procedure the animals were anesthetized using Telezol (4mg/kg) IM and a Ketamine (10mg/kg) booster as needed. Topical anesthetic (proparacaine hydrochloride) was applied prior to the procedure. A pediatric goniolens was between the lids with a canthotomy being necessary in two of the eyes. The animals were placed in a prone position with the head facing forward and strapped against the headrest of a slit lamp (Coherent 930 argon laser with Zeiss slit lamp). A series of argon laser pulses (settings shown in Table 3.1) were delivered to the trabecular meshwork. This procedure causes photocoagulation of the trabecular meshwork and impedes the outflow facility of the eye and results in a sustained increase of the intraocular pressure (IOP). Post-op, 0.2 mg celestone was administered was administered sub-conjunctivally to control inflammation. For this study, one eye (OD) in each of the three animals was treated and the other eye (OS) was left untreated as a control. Sustained pressure increase was observed in all of the treated eyes, though two of the eyes required repeated treatments.

Table 3.1 Settings used for all trabeculoplasty surgeries for inducing glaucoma in the three primates used in this study.

Date	Primate	Power (W)	Exposure (s)	No. of pulses
8-5-2010 (re-start after aiming beam fix)	3	1.2 1.5	0.1 0.2	94 195
8-31-2010	3	1.2	0.2	137
8-31-2010	1	1.2	0.2	257
9- 9-2010	2	1.2	0.2	176
10- 5-2010	3	1.0	0.2	230
11-18-2010	1	1.0	1.0	149
2- 7-2011	3	1.0	0.2	230

3.3 PRESSURE MEASUREMENT

Prior to each retinal scan, an IOP measurement was performed with a Tono-Pen VET (Reichert, Depew, NY). This device has a small plunger which extends 10 μm beyond the tip. The movement of this plunger as the device contacts the cornea is monitored with a pressure transducer, repeated brief touches to the cornea are needed to obtain the measurements. This type of device has been in used for over 40 years and has been shown to be highly repeatable and a reliable method to monitor the IOP.

3.4 IMAGING PROCEDURES

3.4.1 Retinal scans

Two scan patterns were utilized to record retinal OCT images and polarimetric information from primate retinas. Continuous ring scan images were obtained to provide a fundus image and blood vessel map for image registration between imaging sessions on different dates. Continuous ring scans consisted of 100 B-scans each comprised of 360 A-scans. Successive A-scans were separated by 1 degree and successive B-Scans were spaced radially by 15 μm. Clustered ring scan images were recorded to provide the polarization data required to deduce birefringence and phase retardation. Clustered ring scans consisted of 8 circumferential B-scans at a fixed radial distance from the ONH. Each of these B-scans contained 18 evenly spaced clusters each consisting of 200 A-scans recorded over a sine wave pattern with 10 μm spacing. Raster scan images were recorded to provide a complete fundus image including the ONH.

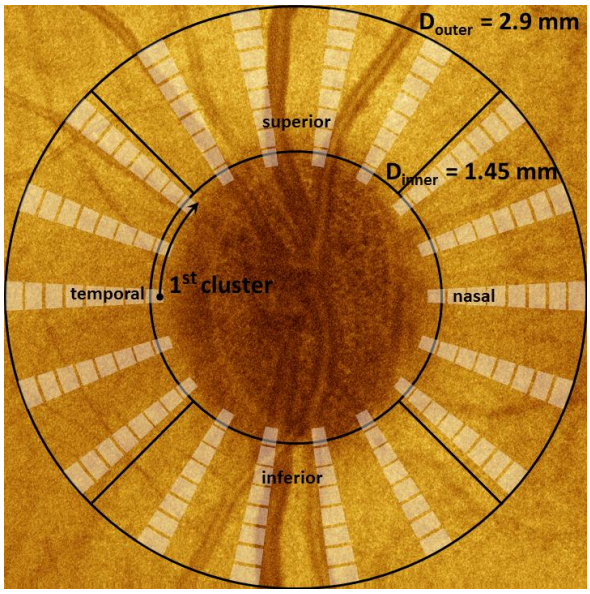

Figure 3.1. Schematic showing clustered imaging regions overlaid on a fundus image with marked quadrants.

3.4.2 ONH placement

For this procedure the animals were anesthetized using Telezol (4mg/kg) IM, intubated, and maintained on ~2% Isofluorane (adjusted as needed to maintain heart rate and respiration). After intubation, prior to imaging, an IOP measurement was performed with a Tono-Pen VET^{TM} (Reichert, Depew, NY). The imaging procedure required stabilizing the animal's head and eyes. The PS-OCT system was mounted on an optical table and the primate was positioned supine for alignment with the PS-OCT scanning optics. The animal's head was mounted in cushioned cradle and maintained in a stable position using a custom rubber mask that was fitted around the nose and mouth to prevent interference with anesthesia apparatus. The mask was attached to the cradle to securely hold the head. The entire fixture including the animal's head could be translated laterally to allow positioning of the pupil in line with the PS-OCT scanning optics. Orthogonal

goniometers permitted rotation of the animal's head and allowed for the ONH head to be centered in the scan range of the of the PS-OCT imaging beam. Temporary sutures were inserted at the limbus on the nasal and temporal side of the eye to prevent eye motion. These sutures were pulled taut and affixed to the stationary facemask. The pupils were dilated prior to the imaging procedure using 1% tropicamide to maximize light throughput. A drop of 10% methylcellulose was placed on the cornea and a custom spherical PMMA 8.4 mm diameter contact lens was placed on the eye to neutralize refractive error of each primate. The lens base curve was 6.2 mm with powers ranging from +3 to -5 diopters.

During the alignment process, the OCT system was continually repeating a raster scanning pattern and updating a fundus image displayed on the computer screen to allow for visualization of the ONH. This fundus image was created in real time by summing the b-scans in the axial direction between user defined depth parameters. The total time to image and display a fundus image depends upon the number of a-scans and the processing time of the computer but was typically on the order of 5 seconds.

3.4.3 Image Collection

A continuous ring scan was taken, to record the location of the primate blood vessels. The continuous ring scan is a series of concentric circular scans around the ONH. Because of the absorption of the light by blood, the blood vessels create a definite shadow in the OCT image, virtually no light is reflected by the tissue below the blood vessels. These continuous ring scan images are summed in the axial dimension to create a

fundus image comprised of the total reflected light from each location in the retina. This fundus image is further improved by using boundary detection to isolate the top surface of the retina, above which is only speckle noise, and a user defined thickness to determine the extent of the retina to be included in the fundus image, minimizing speckle noise below the region of interest. Only the light reflected between the detected boundary and a set thickness is summed to create the fundus image and blood vessel map.

Immediately following the continuous ring scans, to preserve the image position for image registration, 3 clustered ring scans were collected in succession. Clustered ring scans were used to analyze the phase retardation and thickness of the RNFL. Because the phase retardation measurement is extremely susceptible to noise, mainly caused by the speckle noise inherent in the OCT imaging process, numerous a-scans are needed to average the phase information and provide and accurate measurement of the phase retardation. In these experiments 200 a-scans were taken in each cluster for analysis. These clusters were evenly distributed around the ONH (as shown in figure 3.1) in a circular pattern with concentric rings out centered on the ONH in order to evenly sample the RNFL throughout the eye.

Chapter 4: DATA PROCESSING

4.1 OVERVIEW

During the data acquisition raw 16-bit unsigned data were streamed to the computer hard drive and saved as a single binary file. For data processing, the first step in analyzing the phase data and quantifying the RNFL changes was recreating the images from these data. The data are read back in b-scan size segments of data where the B-scan data size is calculated by:

$$16\ \frac{bits}{data\ point} \times \#\ \frac{data\ points}{a\text{-}scans} \times \#\ \frac{a\text{-}scans}{b\text{-}scan} \times\ 2\ channels \tag{4.1}$$

These data are in raw, unsigned 16-bit form and are converted to double precision floating point decimal values using the gain and range value of the card at the time of acquisition and re-shaped into a 2-d array. A fast fourier transform (FFT) converts these data from the k-space (optical frequency) into the time-delay domain. For display as a single b-scan image, these values are scaled to 8-bit grayscale values (0-256) with user-defined values for brightness (minimum value) and contrast (maximum-minimum).

4.2 RNFL SEGMENTATION

Accurate detection of the RNFL boundaries is crucial to achieving accurate polarization and reflectance index measurements. If the boundary is misdetected the thickness measurement is incorrectly calculated and, in addition, the polarization

measurements are sensitive to minor misdetection. The polarization measurements are especially sensitive to errors of overshooting the boundary. Typically for detection of the anterior RNFL boundary the problem is fairly straightforward. Before the RNFL, OCT signal is due mainly to speckle noise arising from SNR in the system making the transition to RNFL signal a steep, immediate transition. The posterior boundary of the RNFL is more difficult to determine because there is a smaller refractive index gradient between the RNFL and the retinal ganglion cell bodies. Various techniques have been introduced over the years [42]-[43] to accurately assess the boundaries. All of these techniques focus on the intensity of light reflected from the RNFL only. The technique used in this study, developed by Wang et al. [44], first finds the boundaries identified using intensity and refines the posterior boundary using the polarization measurement.

The first estimation of the RNFL boundaries is accomplished with a intensity based technique. In this process, each cluster is averaged to reduce the speckle noise and improve the SNR of the image (shown in figure 4.1b). Each averaged A-scan is then processed with a smoothing filter to further reduce the noise. An intensity threshold is then applied to determine the anterior and posterior boundaries of the RNFL (results shown in figure 4.1c).

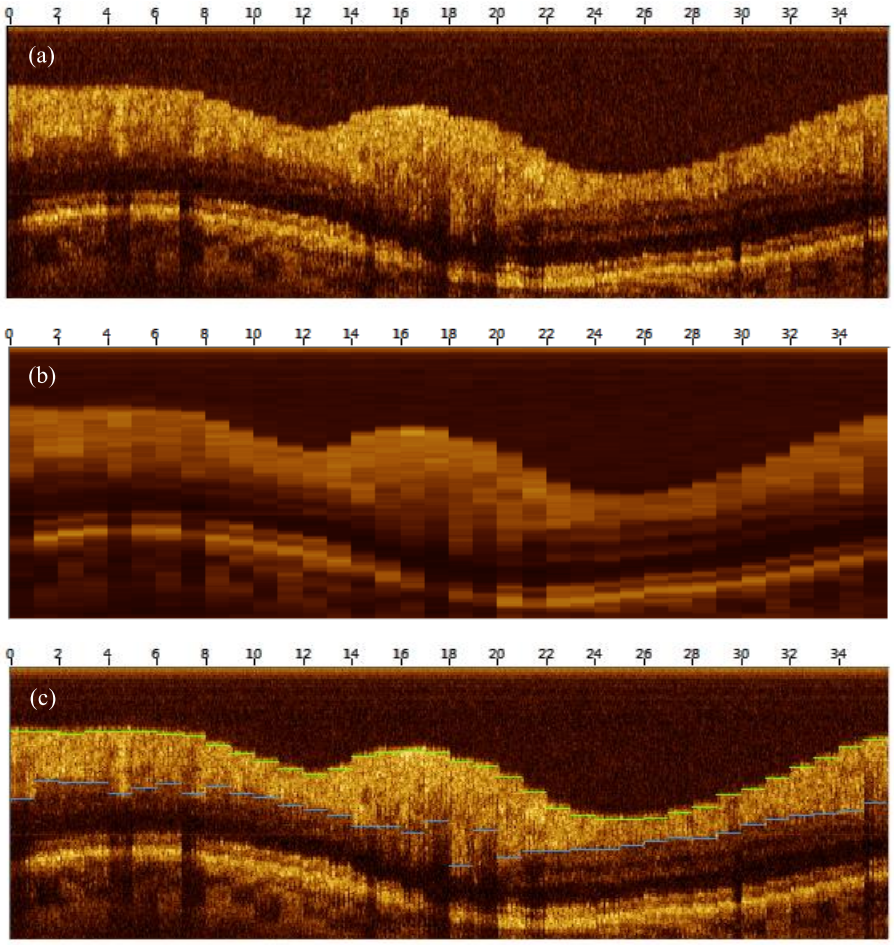

Figure 4.1. A clustered ring scan around the ONH. (a) Original intensity image. (b) Cluster averaged intensity image with improved SNR. (c) Original intensity with overlaid intensity-based RNFL boundaries.

The intensity-based boundaries are then used to calculate the tissue birefringence and its associated uncertainty. Iteratively, the posterior boundary is then adjusted and the birefringence and uncertainty are calculated and compared to the intensity-based measurements. The boundary is adjusted pixel-by-pixel for a total of +/- 22 μm and the boundary that gives the lowest birefringence uncertainty is used as the final boundary.

4.3 FUNDUS IMAGE

For the data collection of this study, it was necessary to orient the data collection in the eye. In a commercial OCT system, this is done with a fundus imaging system such as a line scanning laser ophthalmoscope; but this was not incorporated into the design of the sample optics in this system. Instead, this system creates fundus en face images from the OCT cross-section images.

To create the fundus images, the OCT data, which is a depth-resolved reflection profile, is summed across the A-scans to give a single reflection value for each point in the eye. This removes the depth resolution and integrates the reflected signal from each point in the eye, similar to the image from a standard ophthalmoscope. Each B-scan gives a line in a fundus image and if these summed B-scans are collected for an entire volume scan, the summed lines can be used to create a fundus image. The summed A-scans give a somewhat arbitrary value for each pixel, depending on the scale in the OCT image, so the entire array is normalized according to the max and min values in the entire array and then scaled to a new 8-bit array for display.

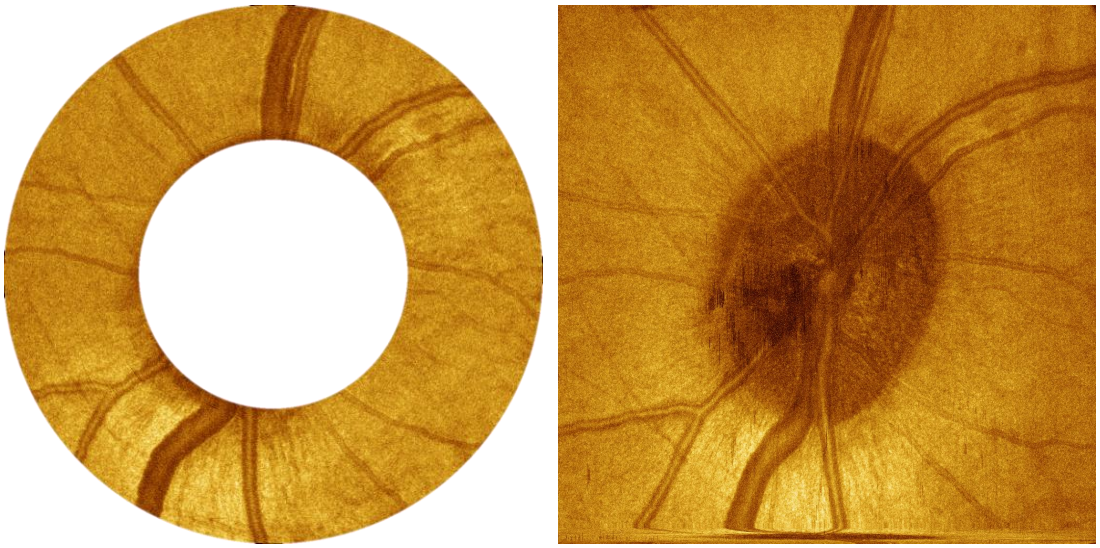

Figure 4.2. Fundus images created from summed a-scans over an entire volume scan. Left is a fundus image created from continuous ring B-scans acquired in rings centered on the optic nerve with a 3 mm maximum diameter. Right is a fundus image created from raster B-scans with a 3 mm edge length.

In this data, the primary features of interest for our purposes are the blood vessels and the ONH. The near-IR wavelength used for imaging makes it an ideal wavelength because the blood absorbs this wavelength preferentially and this absorption gives good contrast between the blood vessels and the surrounding tissue. This technique creates high-resolution fundus images that are exactly registered to the OCT images. The blood vessel "roadmap" is used to register images to account for changes in eye alignment on subsequent days. Also apparent in the fundus image is the ONH, which is used to identify the region of interest for the OCT scans.

4.4 IMAGE REGISTRATION

Because the data for this study was acquired over several months and the eye fixation was accomplished by means of sutures affixed to the head mask the eye had a

somewhat arbitrary rotation and variation in translation during each imaging session. It is the desire of this study to track parameters in a patient over the course of the disease progression and therefore it is necessary to ensure that comparisons in a region are made in a consistent location throughout the study. In order to overcome this challenge, a method was developed for image registration in a given eye through the course of the study. The blood vessels in the fundus image, shown above in figure 4.2, allow for image registration as the eye data is followed over the course of multiple weeks and months. The blood vessel roadmap is a unique signature for each eye and is stable over the time period in this study so is a very convenient way to ensure registration of the data as it is followed through the study.

Data was registered using a translation in 2-dimensions and a rotation [45]. In each imaging session, a continuous ring scan was acquired immediately prior to the clustered ring scans. Sampling of the clustered ring scans was too coarse to allow accurate registration solely based upon this data so the values for rotation and translation found for the continuous ring scan images was applied to the clustered ring scans. Because the registration was applied only during post-processing making exact registration between clusters impossible, the locations of each cluster are only approximate and represent the value of a parameter in the region rather than in an exact location.

Figure 4.3. Fundus image demonstrating registration with reference blood vessel map from data on a different day. Lateral registration forces some of the acquired data to fall off the map.

4.5 POLARIZATION ANALYSIS

4.5.1 Stokes Representation of Polarization

In our PSOCT system, the interference signal is detected for both horizontal [$I_h(k)$] and vertical [$I_v(k)$] polarization components. The digitized signal is then processed to acquire the complex depth-resolved electric field amplitudes for both horizontal $E_h(z)$ and vertical $E_v(z)$ axes. The data is first windowed, with a Hanning window. The power spectral density (PSD) function is then performed. This is done with a custom .dll written with the Intel® performance primitives (IPP) library. This .dll performs the fast Fourier transform and scales the data for the PSD, then returns the amplitudes for each component and the phase difference [$\phi_{diff}(z)$] between the two channels.

This data is used to compute the Stokes vectors for each point. The Stokes vectors are a description of the polarization state of the light and analysis of the change of the Stokes vector as a function of depth allows us to compute the depth-resolved phase retardation in the sample.

Briefly, the Stokes parameters fully describe the light polarization using four parameters (I, Q, U, V). The first, I, is a measure of the intensity and is used to normalize all of the other parameters. The Q parameter describes how well the light is polarized along the horizontal axis (Q=1) or the vertical axis (Q=-1). The U parameter describes how well the light is polarized along the 45^{o} axis (U=1) or the -45^{o} axis (U=-1). The V parameter describes how well the light is circularly polarized right (V=1) or left (V=-1). The stokes parameters are computed from the complex electric fields:

$$\vec{S}(z) \equiv \begin{bmatrix} I(z) \\ Q(z) \\ U(z) \\ V(z) \end{bmatrix} = \begin{bmatrix} E_h(z)^2 + E_v(z)^2 \\ E_h(z)^2 - E_v(z)^2 \\ 2E_h(z)E_v(z)\cos\left(\phi_{diff}(z)\right) \\ 2E_h(z)E_v(z)\sin\left(\phi_{diff}(z)\right) \end{bmatrix} \tag{4.2}$$

The normalized stokes vectors S(z) are typically used for plotting in three dimensional space:

$$S(z) \equiv \begin{bmatrix} Q(z) \\ U(z) \\ V(z) \end{bmatrix} = \begin{bmatrix} E_h(z)^2 - E_v(z)^2 \\ 2E_h(z)E_v(z)\cos\left(\phi_{diff}(z)\right) \\ 2E_h(z)E_v(z)\sin\left(\phi_{diff}(z)\right) \end{bmatrix} \Big/ E_h(z)^2 + E_v(z)^2 \tag{4.3}$$

In the presented PS-OCT system, three input polarization states are sent to the sample, controlled by the phase modulator as described above. The three measured

polarizations are originally separated by 120^{o} around the UV great circle on the Poincare sphere giving three equally spaced initial states on the sphere.

4.5.2 Levenberg-Marquardt LSQ Fits

The Poincare is a useful tool to visualize the light propagation in birefringent media. Normalized Stokes parameters representing the polarization state of light, defined above, are represented by a single point on the 3-dimensional Poincare sphere. In an ideal, noise-free case, a phase retardation in the depth-resolved data maps out a circular arc [*P(z)*] on the Poincare sphere around the optic axis [$\hat{\beta}$] of the media. In the presence of diattenuation [$\varepsilon(z)$], where the eigen-polarization states are differentially attenuated, the arc collapses toward the optic axis. Light collected in OCT accumulates a double pass phase retardation [$2\delta(z)$] and a double-pass diattenuation [$2\varepsilon(z)$]. In the RNFL, the diattenuation is negligible so we are primarily interested in phase retardation [$\delta(z)$].

A Levenberg-Marquardt multi-state nonlinear fitting algorithm [46] is used to determine the double-pass phase retardation from the collected speckle noise corrupted PS-OCT information [*S(z)*]. Phase retardation, diattenuation, and eigen-axis parameters are estimated to determine the ideal noise-free arc on the Poincare sphere. The residual function [R_M] used in the multi-state algorithm is defined such that

$$R_M = \sum_{m=1}^{M} R_0\left(S_m(z); \delta, \hat{\beta}, P_m(0)\right) \tag{4.4}$$

R_0 specifies the goodness of fit and is a measure of squared deviation between *S(z)* and the noise free model *P(z)*. In our case, three input polarization states are used so that M = 3.

$$R_0 = \sum_n \left| S(z) - P\left(z; 2\delta, \hat{\beta}, P(0)\right)\right|^2 \tag{4.5}$$

In this model, the ideal polarization arcs constrained to share the same optic axis and the same phase retardation. High uncertainty is more likely if the input polarization states are close to the optic axis and therefore trace a small arc on the Poincare sphere. Uncertainty in this algorithm is calculated from the sum of squares between the measured and fitted data points. Three input polarization states are used in the system in order to allow for uncertainty in one state to be compensated in the residual function by the other states.

4.6 REFLECTANCE INDEX CALCULATION

To quantify the RNFL reflectance, we present a definition for the RNFL reflectance index (RI), defined as the ratio of RNFL brightness [I_{RNFL}] to the brightness of a thin layer [I_{RPE}] about the RPE containing the inner and outer segment and superficial choroid. The RI definition normalized variation due to system performance and corneal transmission. For example, increased IOP can cause increased corneal cloudiness reducing light intensity incident on the retina. Defining RI as the brightness ratio between the RNFL and RPE mitigates the effect of corneal transmission changes. Variations in refraction are more difficult to compensate; however, the image was optimized for the

best retinal focus at the start of each imaging session using a range of custom made contact lenses to minimize refractive error.

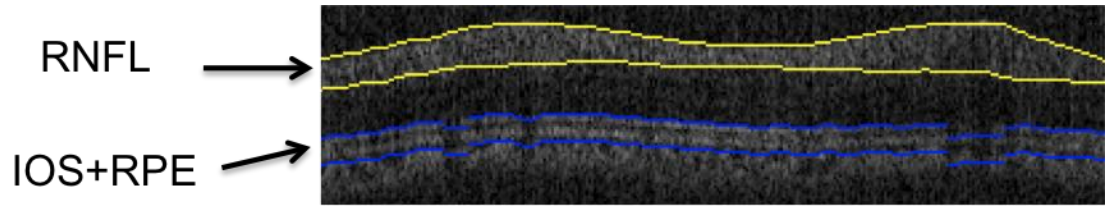

Figure 4.4. Segmented layers to determine RI. RNFL and RPE layers in a B-scan image. The layer between the yellow boundaries is RNFL. The layers between the blue boundaries are the layer containing the inner and outer segment as well as the retinal pigment epithelium (RPE) + superficial choroid.

The RNFL in each A-scan was identified with an automatic boundary detection technique and the average RNFL brightness within the boundaries was used to calculate the RI. The upper boundary of the retinal layer between the inner nuclear layer and the choroid was identified automatically in the B-scan images. The lower boundary was taken to be 10 pixels (~75 μm) below this upper boundary. The brightness value of the region between these two boundaries (Figure 4.4 indicated in blue) is used to compute the *RI*. We define the *RI* for one A-scan in a B-scan image as:

$$RI_a = \frac{\bar{I}_{RNFL_a}}{\bar{I}_{RPE}} \tag{4.6}$$

where for the continuous ring scan,

$$\bar{I}_{RNFL_a} = \frac{\sum_a I_{RNFL_a}}{N_{RNFL_a}} \tag{4.7}$$

which is the average pixel intensity value in the RNFL in a^{th} A-scan. For the clustered ring scan,

$$\bar{I}_{RNFL_c} = \frac{\sum_c \left(\sum_a I_{RNFL_a} \Big/ N_{RNFLa} \right)_c}{N_c} \tag{4.8}$$

which is the average raw signal value in the RNFL in all A-scans of the c^{th} cluster. For both continuous ring scan and clustered ring scan data,

$$\bar{I}_{RPE} = \frac{\sum_b \left(\sum_a I_{RPE_a} \Big/ N_{RPE} \right)_b}{N_b} \tag{4.9}$$

which is the average raw signal value in the region containing the RPE over all the B-scans in one image collection, where N_b is number of B-scans in each image collection, N_{RPE} is number of pixels in the layer containing the RPE in one B-scan and I is the raw OCT signal value. We calculated *RI* for A-scans in each image collection and then constructed an *RI* map from this data.

4.7 FEATURE EXTRACTION AND STATISTICAL ANALYSIS

We used mixed-effects models in this study since they can capture the similarities between as well as the variance among different primates and are effective for the analysis of longitudinal, repeated-data measurements. The R statistical programming language (v2.13.10 07/08/2011; http://www.R-project.org/, R Development Core Team, 2011, R Foundation for Statistical Computing, Vienna, Austria) and R studio (v0.94, 06/15/2011, RStudio, Inc.) was used to implement the linear mixed-effects models. We

used MATLAB™ (The Mathworks, Natick, MA) to implement the non-linear mixed-effects model.

To identify trends in the data, we analyzed averaged data for the entire retinal maps, as well as different regions. We calculated the average for the entire ring as well as the superior, inferior, nasal, and temporal regions as well as the 4 inner rings and 4 outer rings average for all the RNFL thickness, phase, birefringence and RI maps for each primate eye. All these parameters for each eye were plotted against the number of days after the first laser treatment for each primate. Linear mixed effects models were used to evaluate whether there were any changes in the optical parameters over time:

$$P_{i,t} = (a_1 + b_i) + a_2 \times t + E_{i,t} \tag{4.10}$$

where $P_{i,t}$ is the value of parameter P of the control eye or treated eye of the ith primate on day *t*. The intercept [a_1] and the mean slope for number of days [t] after the laser treatments are the fixed effects. The random effect is the intercept for the ith primate [b_i], which is normally distributed with mean zero and standard deviation δ. $E_{i,t}$ is the random error component for the control eye or treated eye of the i^{th} primate on day t and is assumed to be normally distributed with a mean of zero and standard deviation δ_E.

The difference in the measured data parameters between the control eye and treated eye on each day was plotted against both an integral of IOP and the number of days after the laser treatment (IOP damage integral); this is valid assuming that the retinal damage occurs due to chronic increased IOP rather than an acute pressure increase. The

data were fit with a linear mixed effect model below to identify statistically significant trends:

$$Pdif_{i,t} = (\gamma_0 + \beta_i) + \gamma_1 \times IOPintdif_{i,t} + \xi_{i,t} \tag{4.11}$$

where $Pdif_{i,t}$ is the difference of the RNFL parameter between the control eye and the treated eye for the i^{th} primate on day t. The fixed effects are the intercept γ_0 and the mean slope γ_1 for the IOP damage integral. The random effect is the intercept for the i^{th} primate, β_i, which is normally distributed with mean zero and standard deviation δ_i. $x_{i,t}$ is the random error component for the i^{th} primate on day t and is assumed to be normally distributed with a mean of zero and standard deviation δ.

We also fit our data to a nonlinear mixed effects model as described below:

$$Pdif_{i,t} = (\alpha_0 + \eta_i) - \alpha_1 \times e^{-\frac{IOPintdif_{i,t}}{\tau}} + \varepsilon_{i,t} \tag{4.12}$$

where $Pdif_{i,t}$ is the difference of the RNFL parameter between the control eye and the treated eye for the i^{th} primate on day t. The fixed effects are the intercept α_0, the coefficient α_1 for the exponential of IOP damage integral, and the lifetime τ. The random effect is the intercept for the i^{th} primate, η_i, which is normally distributed with mean zero and standard deviation δ_i. $e_{i,t}$ is the random error component for the i^{th} primate on day t and is assumed to be normally distributed with a mean of zero and standard deviation δ_e. We use the Akaike information criterion (AIC) and the Bayesian information criterion (BIC) to compare the non-linear model and the linear model.

Chapter 5: RESULTS

5.1 IOP INCREASE

There were 6 total eyes measured for this experiment, 3 control and 3 treated eyes. Two of the treated eyes required multiple procedures to induce a sustained pressure increase in the eye. A moderate pressure increase was achieved in all of the eyes during the course of this study, shown in figure 5.1, with an average pressure increase of 16 mmHg, a lower and more physiologically relevant pressure increase than was applied in a similar previous study which demonstrated an associated change in RNFL thickness.

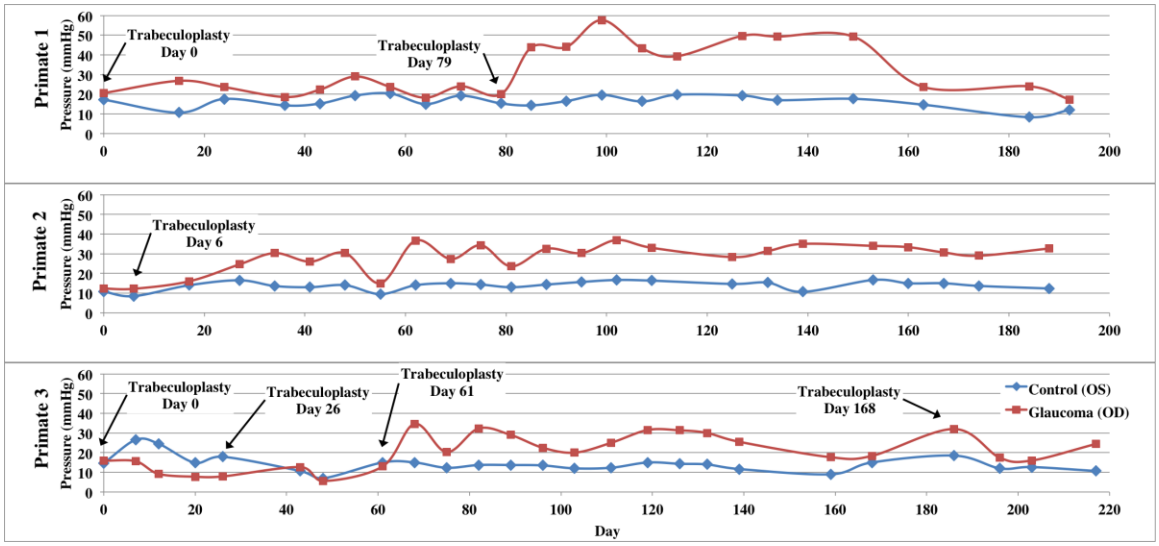

Figure 5.1. IOP vs. time in control (blue) and treated (red) eyes of each primate over course of the study.

5.2 ANALYSIS OF RNFL PARAMETERS VERSUS TIME

We measured 4 parameters from the clustered retinal scans: RNFL thickness, phase retardation, birefringence, and RI. We also measured 2 parameters, RNFL thickness and RI, from the continuous ring retinal scans. The difference values between

control and treated eyes at the beginning, middle, and end time points are presented in figures 5.2 to 5.7.

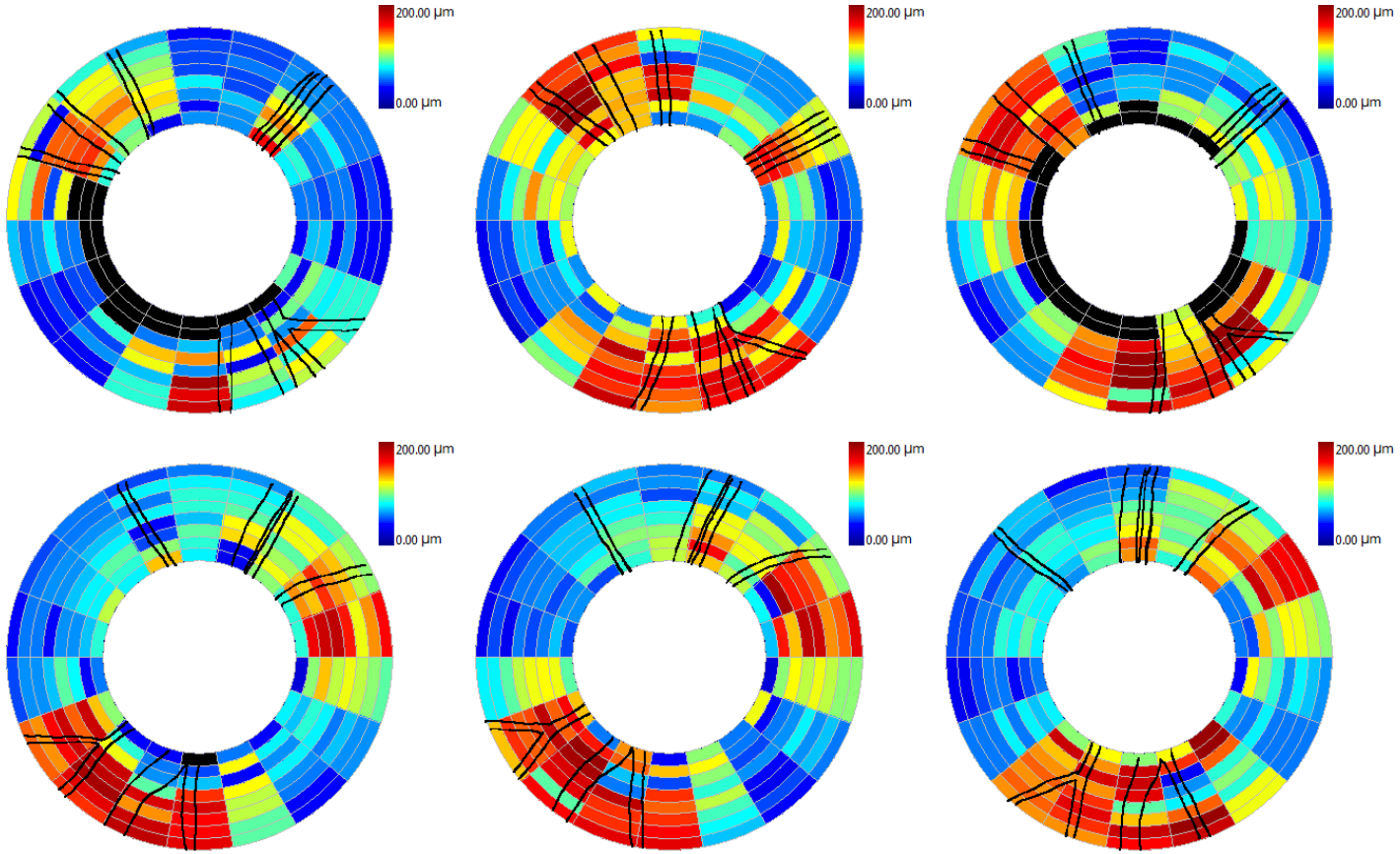

Figure 5.2. RNFL thickness maps for clustered retinal scans for primate 2. Top row is OD (treated eye) and bottom row is OS (control eye). Time points correspond to beginning (left column, day 27), middle (center column, day 81), and end (right column, day 174) of the study. Blood vessels indicated by black lines. Excluded clusters are marked black.

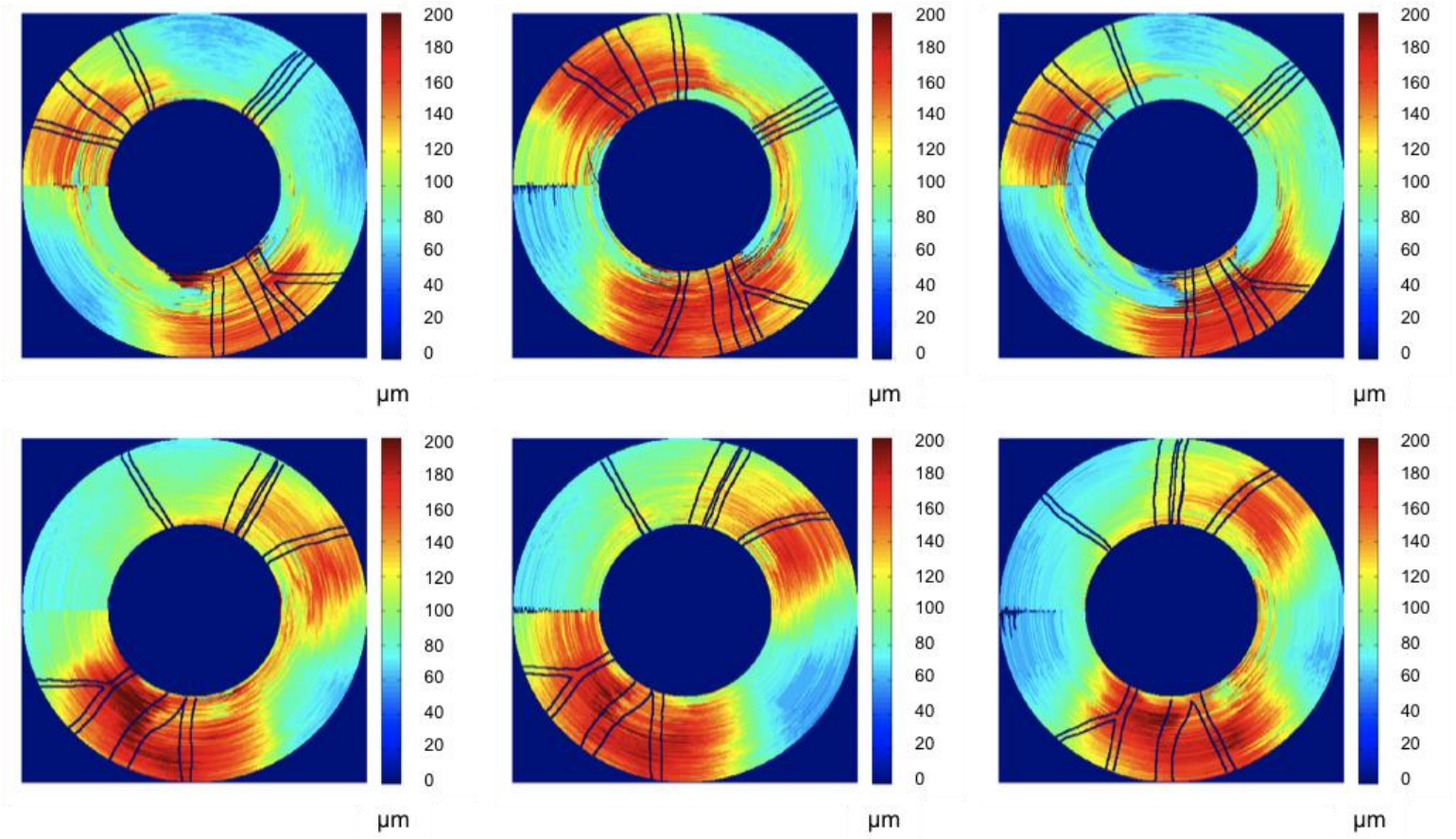

Figure 5.3. RNFL thickness maps for continuous ring scans for primate 2. Top row is OD (treated eye) and bottom row is OS (control eye). Time points correspond to beginning (left column, day 27), middle (center column, day 81), and end (right column, day 174) of the study. Blood vessels indicated by black lines.

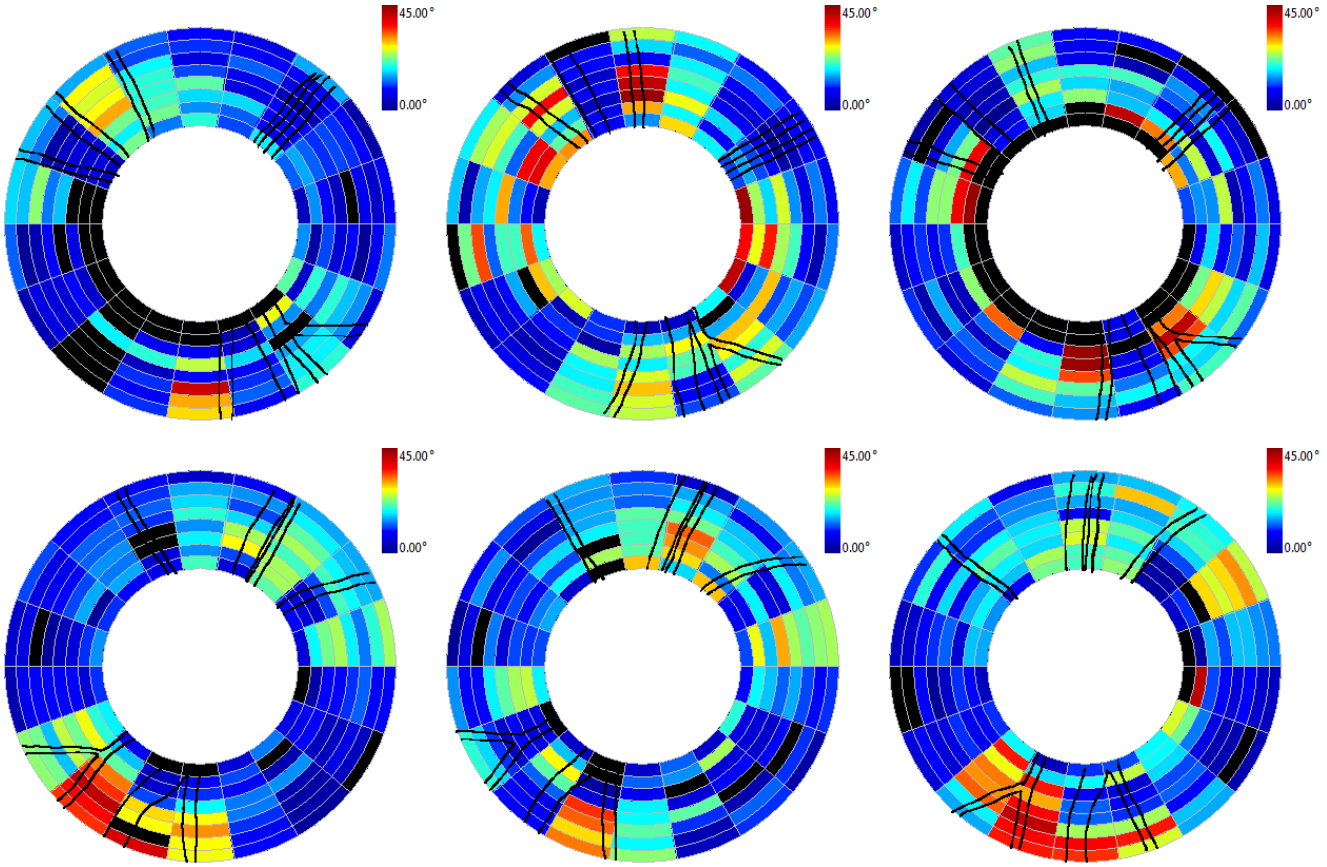

Figure 5.4. RNFL phase retardation maps for clustered retinal scans for primate 2. Top row is OD (treated eye) and bottom row is OS (control eye). Time points correspond to beginning (left column, day 27), middle (center column, day 81), and end (right column, day 174) of the study. Blood vessels indicated by black lines. Excluded clusters are marked black.

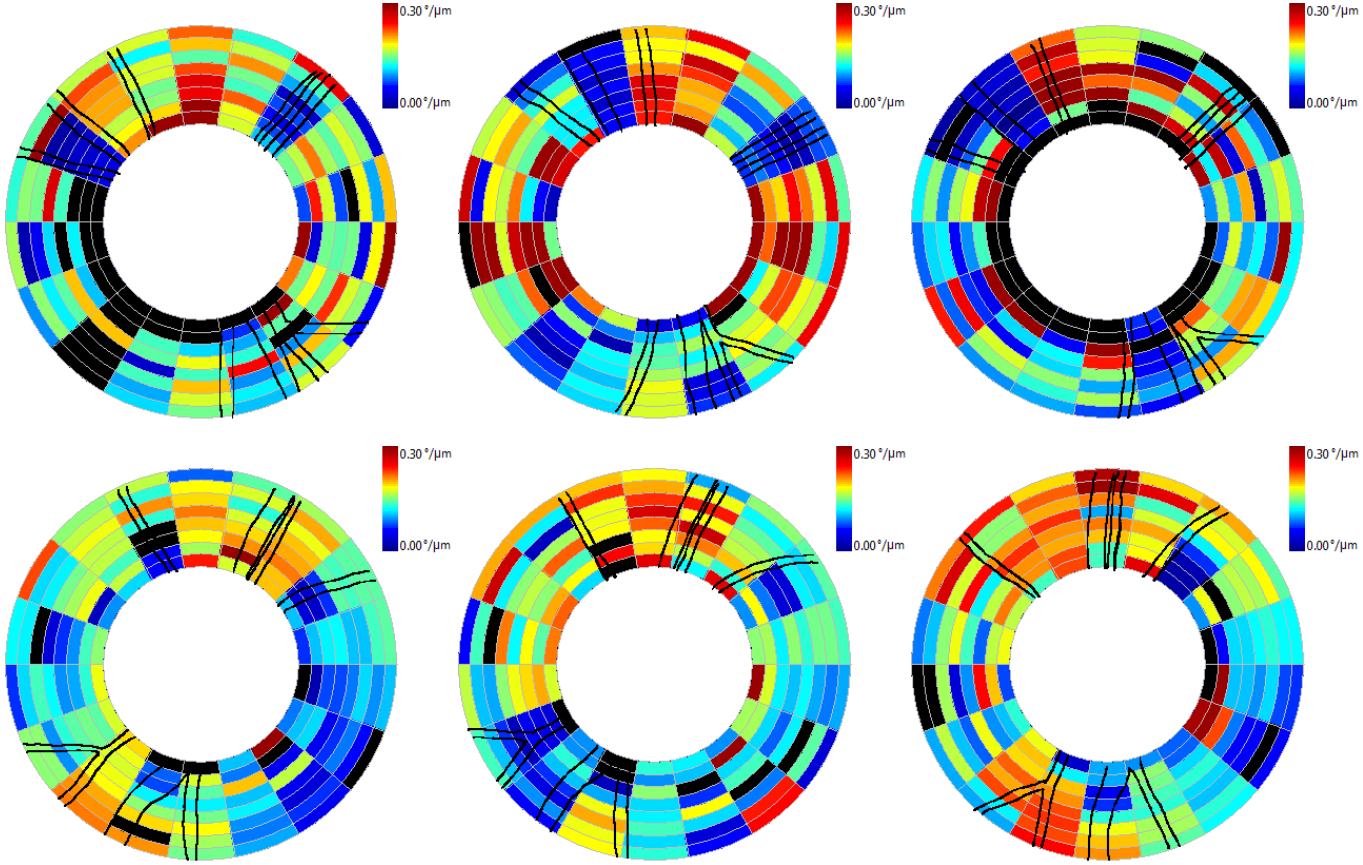

Figure 5.5. RNFL birefringence maps for clustered retinal scans for primate 2. Top row is OD (treated eye) and bottom row is OS (control eye). Time points correspond to beginning (left column, day 27), middle (center column, day 81), and end (right column, day 174) of the study. Blood vessels indicated by black lines. Excluded clusters are marked black.

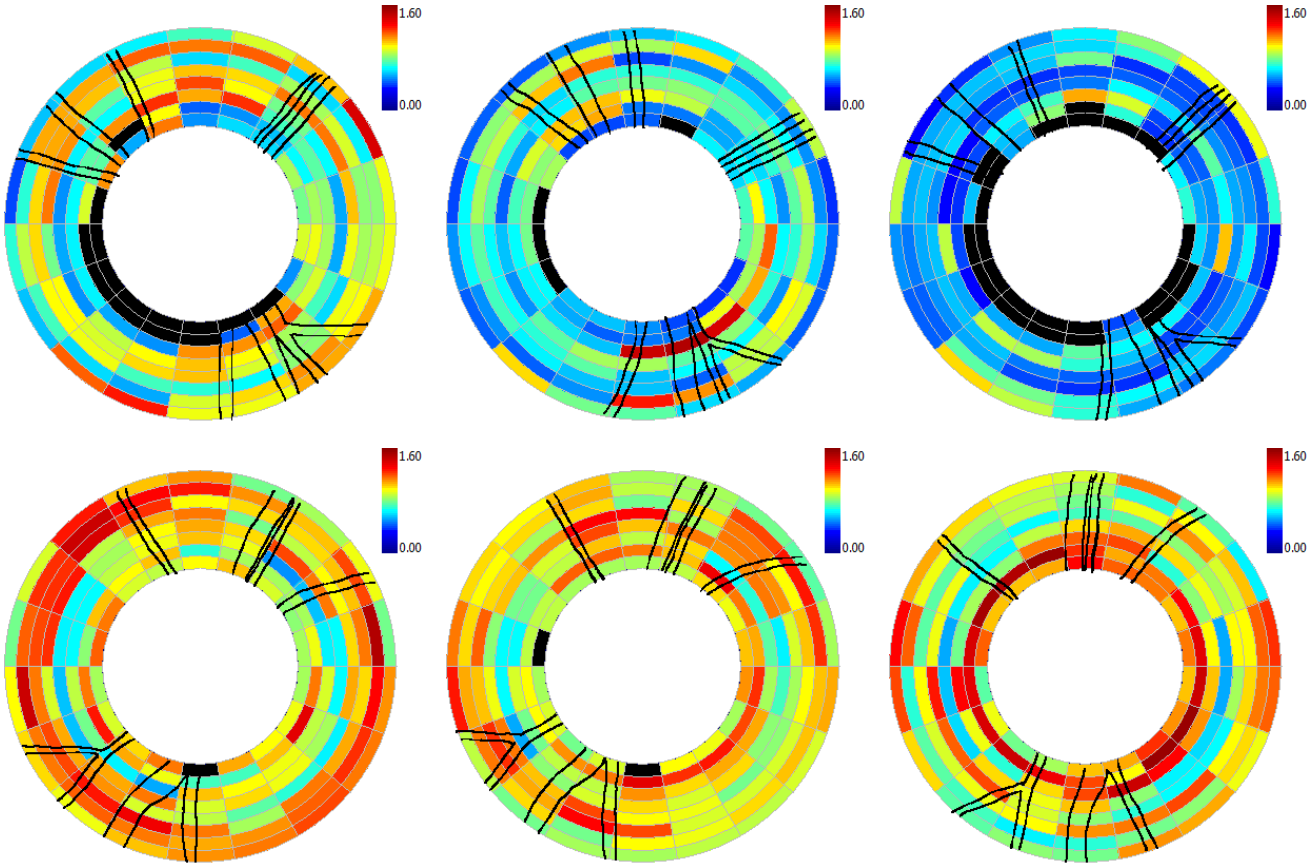

Figure 5.6. RNFL reflectance index (*RI*) maps for clustered retinal scans for primate 2. Top row is OD (treated eye) and bottom row is OS (control eye). Time points correspond to beginning (left column, day 27), middle (center column, day 81), and end (right column, day 174) of the study. Blood vessels indicated by black lines. Excluded clusters are marked black.

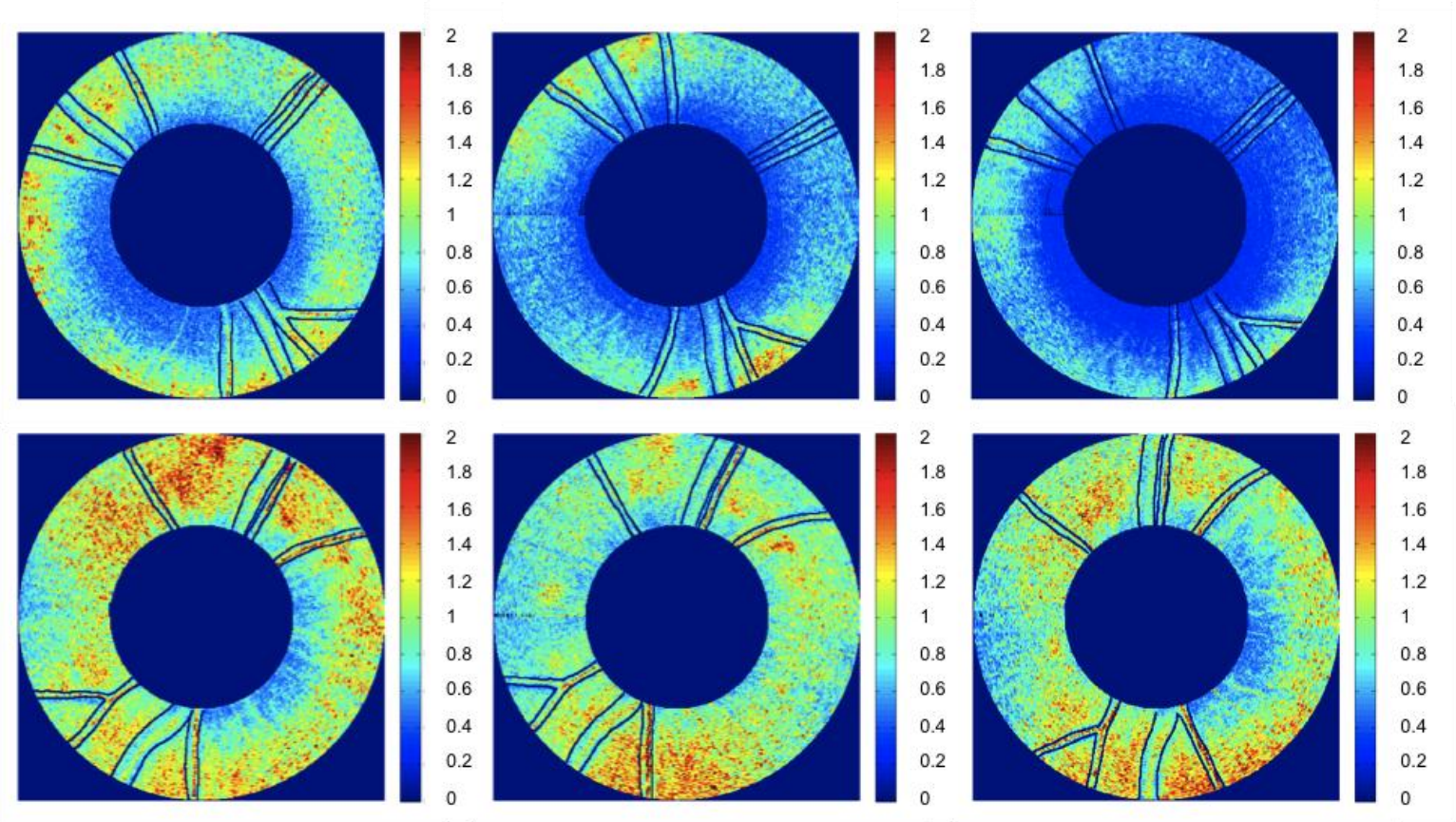

Figure 5.7. RNFL reflectance index (*RI*) maps for continuous ring scans for primate 2. Top is OD (treated eye) and bottom is OS (control eye). Time points correspond to beginning (left, day 27), middle (center, day 81), and end (right, day 174) of the study. Blood vessels indicated by black lines.

Each parameter (RNFL thickness, phase retardation, birefringence, and reflectance index (RI)) averaged over the entire ring scan is plotted against number of days from the first laser trabeculoplasty (Figure 5.8-5.13). A linear mixed effects model (4.10) is applied to fit each RNFL parameter as a function of time. In both clustered and continuous ring scan data, both the control and treated eyes showed a significant decrease in *RI*. No significant changes in RNFL thickness, birefringence, or phase retardation averaged over all rings was observed (Figures 5.8-5.11). Retinal maps were segmented and RNFL parameters in each segment was analyzed separately in addition to parameter averages over the entire retina. RNFL parameters were computed and averaged in segmented regions including the four inner rings, four outer rings, superior, inferior, nasal, and temporal quadrants and plotted over time. Fits were performed in each segmented region for all three primates combined (Table 5.1) as well as individuals (Table 5.2 - 5.4).

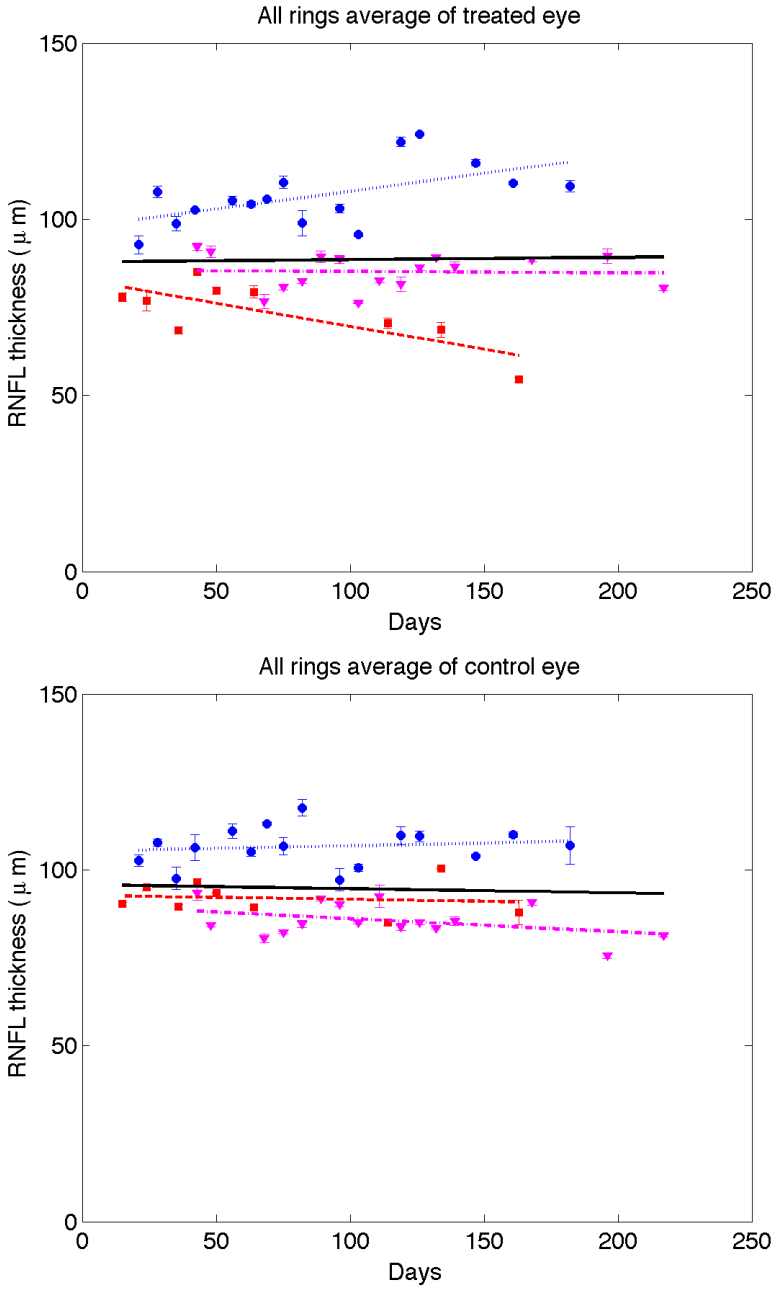

Figure 5.8. Time variation of averaged (all rings) RNFL thickness of treated (top) and control (bottom) eyes for clustered ring scans (squares primate 1; circles primate 2, and triangles primate 3). Linear mixed effects model fits for individual primates (colored lines) and combined (all primates, black).

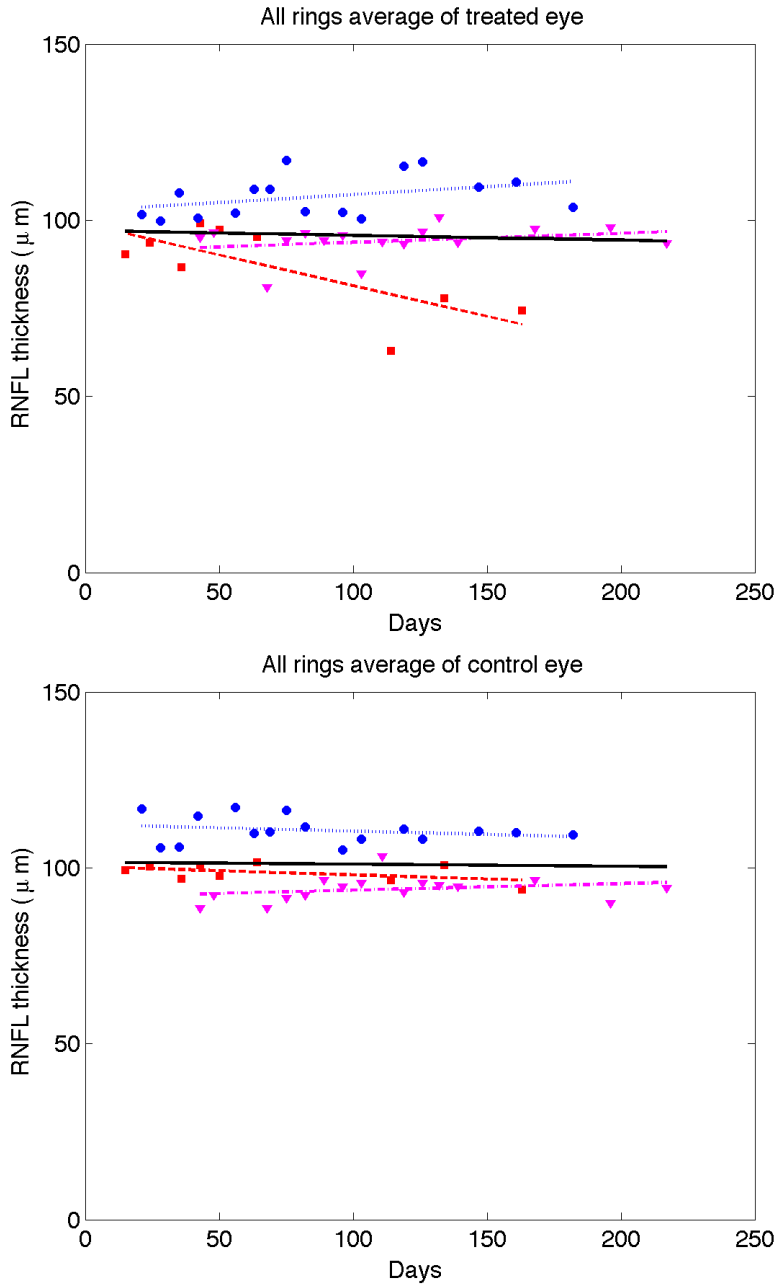

Figure 5.9. Time variation of averaged (all rings) RNFL thickness of treated (top) and control (bottom) eyes for continuous ring scans (squares primate 1; circles primate 2, and triangles primate 3). Linear mixed effects model fits for individual primates (colored lines) and combined (all primates, black).

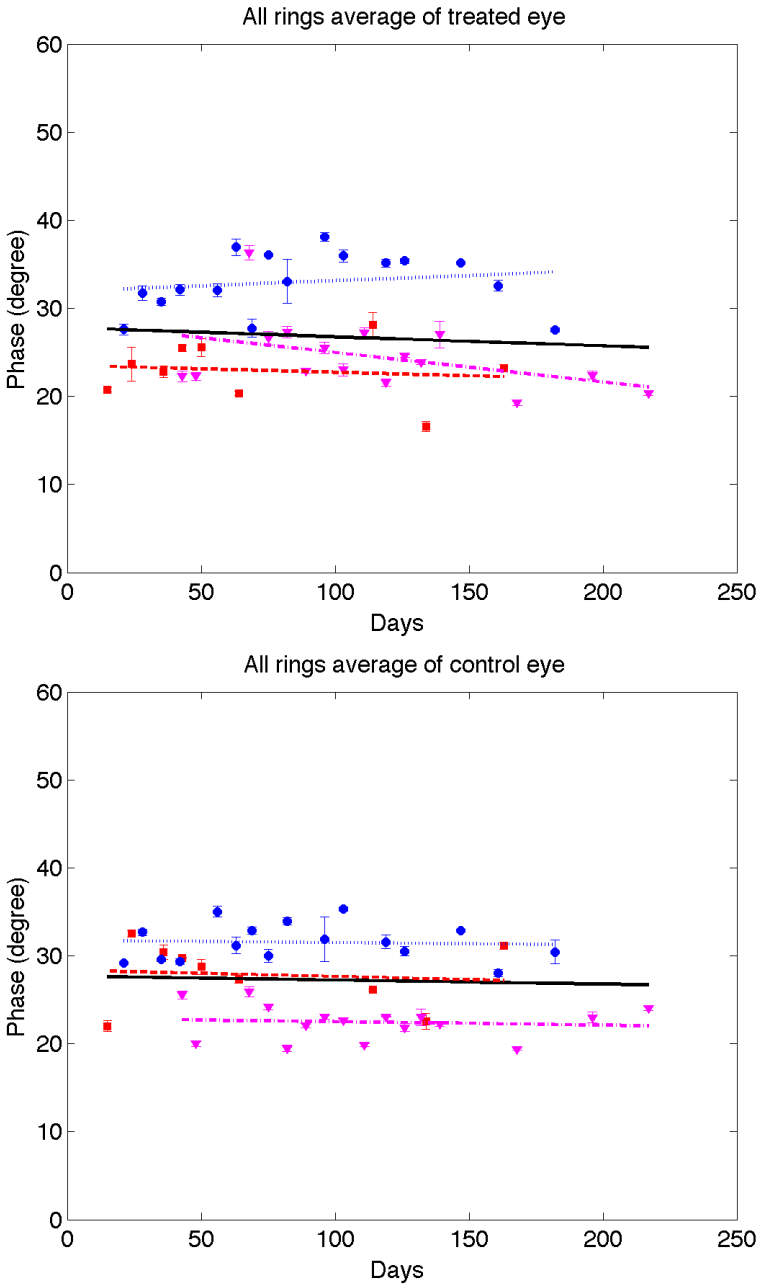

Figure 5.10. Time variation of averaged (all rings) RNFL phase retardation of treated (left) and control (right) eyes for clustered retinal scans (squares primate 1; circles primate 2, and triangles primate 3). Linear mixed effects model fits for individual primates (colored lines) and combined (all primates, black).

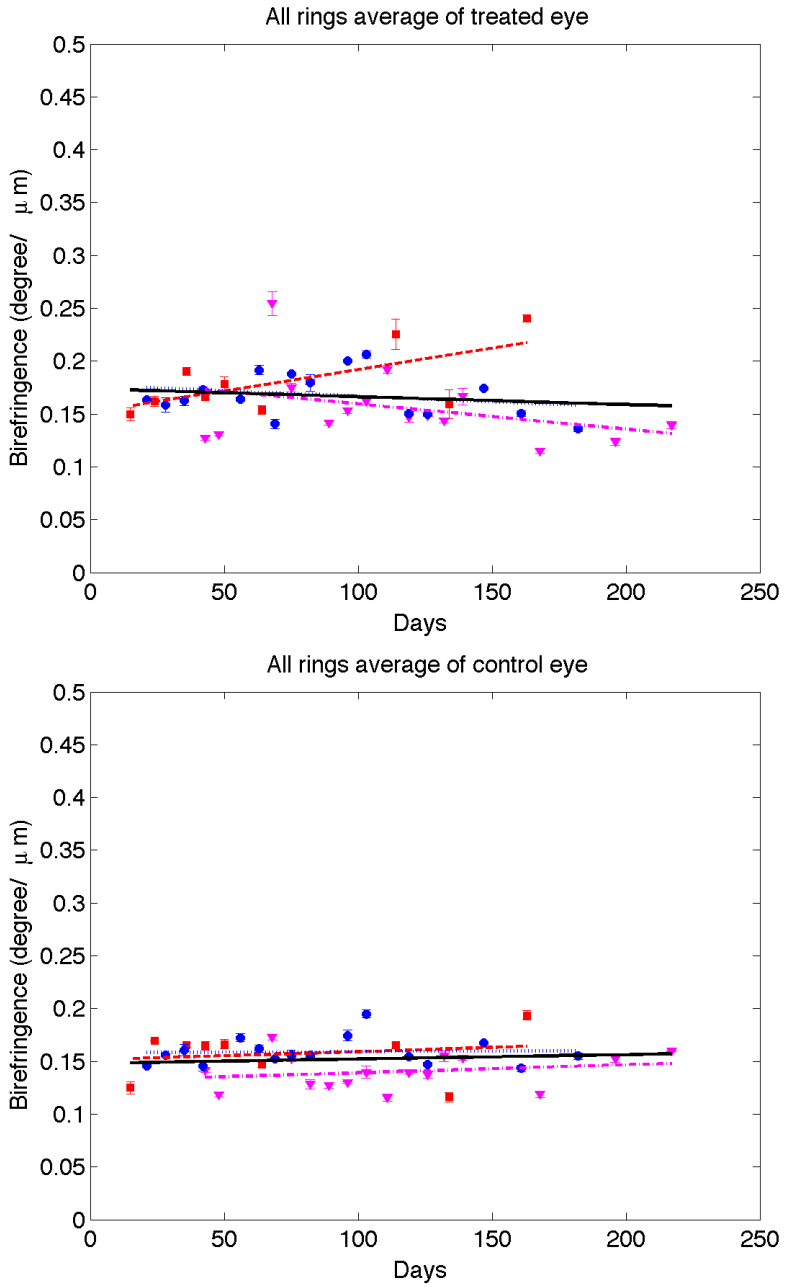

Figure 5.11. Time variation of averaged (all rings) RNFL birefringence of treated (left) and control (right) eyes for clustered retinal scans (squares primate 1; circles primate 2, and triangles primate 3). Linear mixed effects model fits for individual primates (colored lines) and combined (all primates, black).

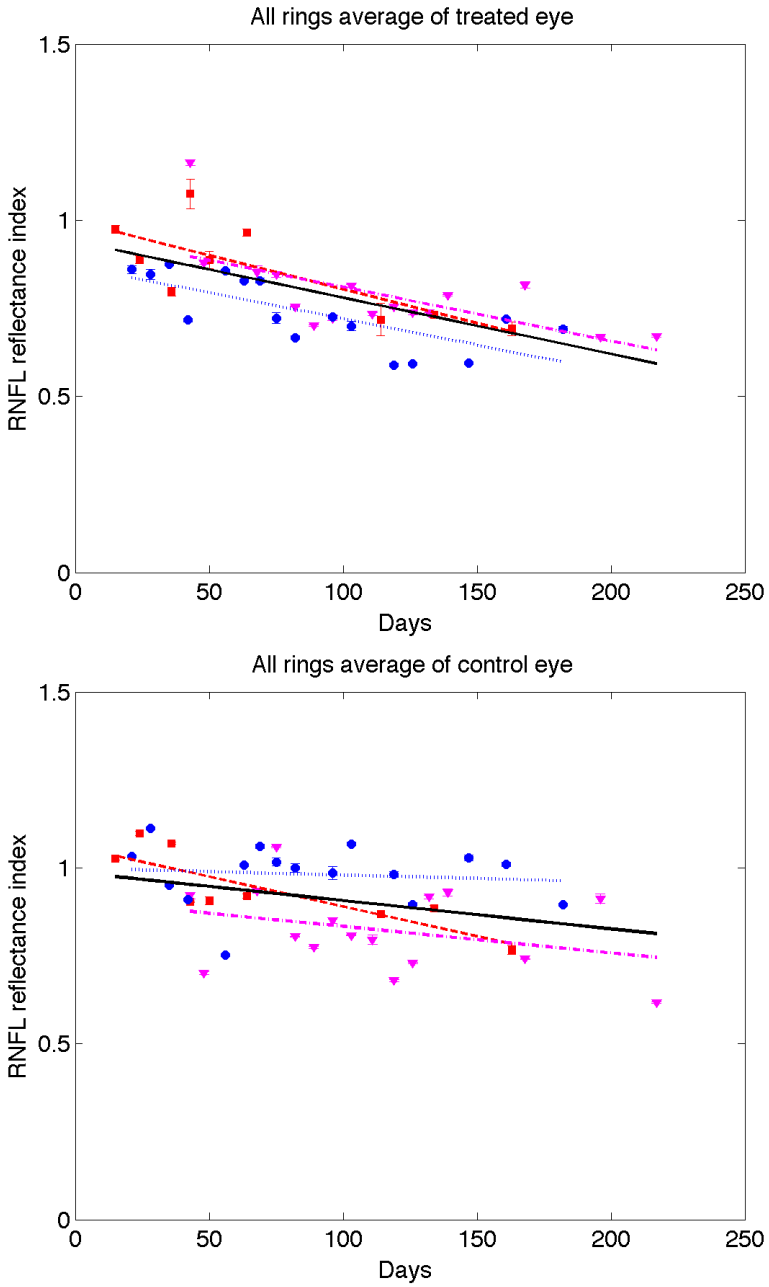

Figure 5.12. Time variation of averaged (all rings) RNFL reflectance index (*RI*) of treated (left) and control (right) eyes for clustered ring scans (squares primate 1; circles primate 2, and triangles primate 3). Linear mixed effects model fits for individual primates (colored lines) and combined (all primates, black). The linear mixed model suggests *RI* decreased significantly over time for both treated ($p<0.0001$) and control eyes ($p<0.05$).

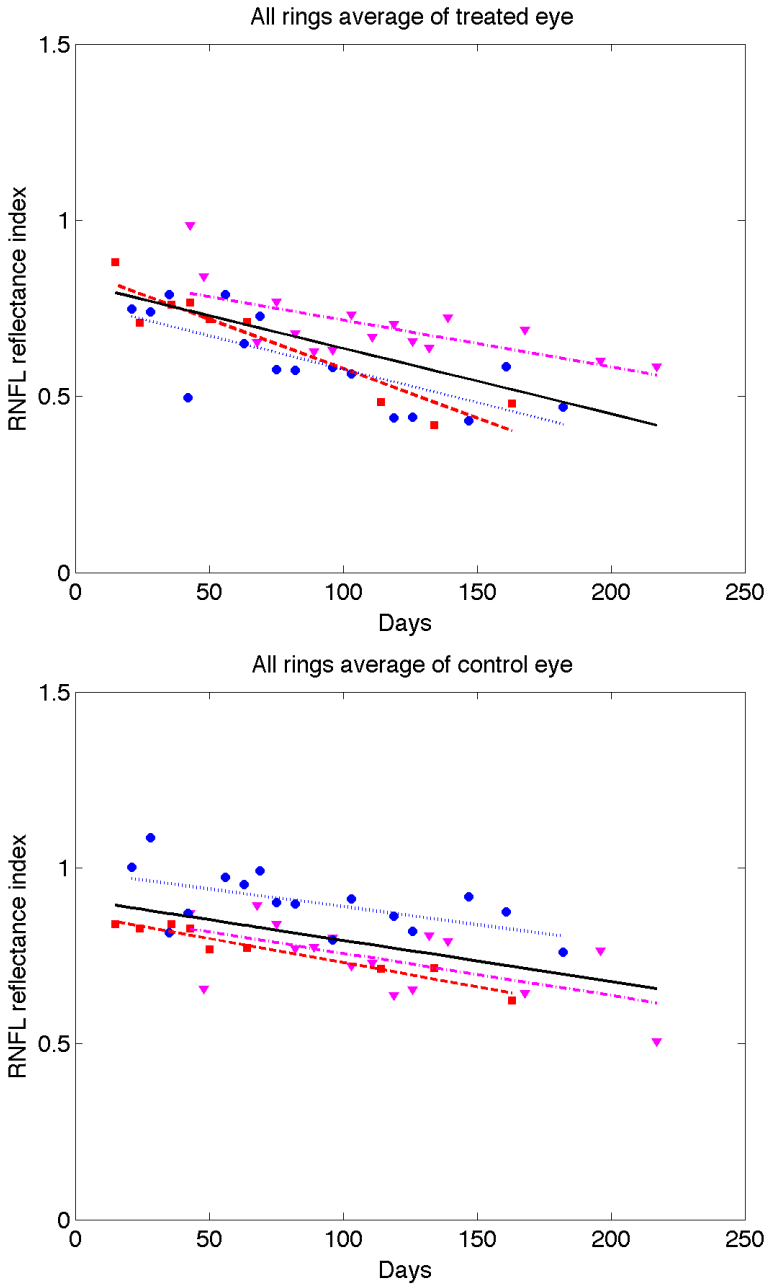

Figure 5.13. Time variation of averaged (all rings) RNFL reflectance index (*RI*) of treated (left) and control (right) eyes for continuous ring scans (squares primate 1; circles primate 2, and triangles primate 3). Linear mixed effects model fits for individual primates (colored lines) and combined (all primates, black). The linear mixed model suggests *RI* decreased significantly over time for both treated ($p<0.0001$) and control eyes ($p<0.05$).

Table 5.1 RNFL parameters in segmented regions versus number of days for all primates analyzed with a linear mixed model.

RNFL Parameter	Feature	Mix of all 3 primates			
		Control		Treated	
		Slope	p (slope)	Slope	p (slope)
Clustered Thickness	All rings	-1.15×10^{-2}	>0.05	6.45×10^{-3}	>0.05
	Inner rings	-1.11×10^{-2}	>0.05	4.03×10^{-2}	>0.05
	Outer rings	-2.30×10^{-2}	>0.05	-1.59×10^{-2}	>0.05
	Superior	3.22×10^{-2}	>0.05	2.93×10^{-3}	>0.05
	Inferior	-2.40×10^{-2}	>0.05	-5.21×10^{-2}	>0.05
	Nasal	-5.47×10^{-2}	<0.05*	4.37×10^{-2}	>0.05
	Temporal	3.13×10^{-2}	>0.05	-2.19×10^{-3}	>0.05
Continuous Thickness	All rings	-5.66×10^{-3}	>0.05	-1.34×10^{-2}	>0.05
	Inner rings	-6.50×10^{-3}	>0.05	-1.05×10^{-2}	>0.05
	Outer rings	-6.76×10^{-3}	>0.05	-1.50×10^{-2}	>0.05
	Superior	-9.73×10^{-4}	>0.05	-1.65×10^{-2}	>0.05
	Inferior	-1.73×10^{-2}	>0.05	-4.54×10^{-2}	>0.05
	Nasal	1.25×10^{-2}	>0.05	-1.02×10^{-2}	>0.05
	Temporal	-1.60×10^{-2}	>0.05	2.96×10^{-2}	>0.05
Clustered Reflectance Index (RI)	All rings	-8.03×10^{-4}	<0.05*	-1.60×10^{-3}	<0.0001*
	Inner rings	-4.40×10^{-4}	>0.05	-1.28×10^{-3}	<0.0001*
	Outer rings	-1.14×10^{-3}	<0.05*	-1.88×10^{-3}	<0.0001*
	Superior	-8.66×10^{-4}	<0.05*	-1.51×10^{-3}	<0.0001*
	Inferior	-6.74×10^{-4}	>0.05	-1.42×10^{-3}	<0.0001*
	Nasal	-8.08×10^{-4}	<0.05*	-1.76×10^{-3}	<0.0001*
	Temporal	-8.64×10^{-4}	<0.05*	-1.76×10^{-3}	<0.0001*
Continuous Reflectance Index (RI)	All rings	-1.17×10^{-3}	<0.01*	-1.86×10^{-3}	<0.0001*
	Inner rings	-1.21×10^{-3}	<0.01*	-1.88×10^{-3}	<0.0001*
	Outer rings	-1.15×10^{-3}	<0.01*	-1.86×10^{-3}	<0.0001*
	Superior	-1.47×10^{-3}	<0.01*	-2.21×10^{-3}	<0.0001*
	Inferior	-8.43×10^{-4}	<0.01*	-1.93×10^{-3}	<0.0001*
	Nasal	-1.09×10^{-3}	<0.01*	-1.93×10^{-3}	<0.0001*
	Temporal	-1.30×10^{-3}	<0.01*	-1.35×10^{-3}	<0.0001*
Birefringence	All rings	4.15×10^{-5}	>0.05	-7.43×10^{-5}	>0.05
	Inner rings	3.98×10^{-5}	>0.05	-1.39×10^{-4}	>0.05
	Outer rings	5.29×10^{-5}	>0.05	1.93×10^{-5}	>0.05
	Superior	4.04×10^{-6}	>0.05	-1.13×10^{-4}	>0.05
	Inferior	-7.72×10^{-5}	>0.05	2.29×10^{-4}	>0.05
	Nasal	1.62×10^{-4}	>0.05	-1.97×10^{-4}	>0.05
	Temporal	1.13×10^{-4}	>0.05	2.67×10^{-4}	>0.05
Phase Retardation	All rings	-4.52×10^{-3}	>0.05	-1.03×10^{-2}	>0.05
	Inner rings	-4.75×10^{-3}	>0.05	-1.27×10^{-2}	>0.05
	Outer rings	-6.72×10^{-3}	>0.05	-4.80×10^{-3}	>0.05
	Superior	9.85×10^{-3}	>0.05	-2.60×10^{-2}	>0.05
	Inferior	-3.69×10^{-2}	<0.05*	1.58×10^{-2}	>0.05
	Nasal	-2.24×10^{-3}	>0.05	-1.26×10^{-2}	>0.05
	Temporal	2.35×10^{-2}	<0.05*	-4.92×10^{-3}	>0.05

Table 5.2 RNFL parameters in segmented regions versus number of days for primate 1 analyzed with a linear mixed model.

RNFL Parameter	Feature	Primate 1			
		Control		Treated	
		Slope	p (slope)	Slope	p (slope)
Clustered Thickness	All rings	-1.04×10^{-2}	>0.05	-1.31×10^{-1}	<0.05*
	Inner rings	-9.97×10^{-3}	>0.05	-1.08×10^{-1}	>0.05
	Outer rings	-2.12×10^{-2}	>0.05	-1.46×10^{-1}	<0.05*
	Superior	3.08×10^{-2}	>0.05	-1.02×10^{-1}	>0.05
	Inferior	-6.18×10^{-3}	>0.05	-3.91×10^{-1}	<0.05*
	Nasal	-1.36×10^{-1}	<0.05*	3.42×10^{-1}	<0.05*
	Temporal	1.61×10^{-1}	<0.05*	-2.22×10^{-1}	<0.05*
Continuous Thickness	All rings	-2.34×10^{-2}	>0.05	-1.75×10^{-1}	<0.05*
	Inner rings	-1.99×10^{-2}	>0.05	-1.89×10^{-1}	<0.05*
	Outer rings	-2.73×10^{-2}	>0.05	-1.64×10^{-1}	<0.05*
	Superior	-3.47×10^{-2}	>0.05	-7.62×10^{-2}	>0.05
	Inferior	-1.19×10^{-2}	>0.05	-4.05×10^{-1}	<0.05*
	Nasal	2.23×10^{-2}	>0.05	-1.42×10^{-1}	<0.05*
	Temporal	-5.33×10^{-2}	>0.05	9.26×10^{-3}	>0.05
Clustered Reflectance Index (RI)	All rings	-1.71×10^{-3}	<0.05*	-1.74×10^{-3}	<0.05*
	Inner rings	-1.45×10^{-3}	<0.05*	-1.19×10^{-3}	<0.05*
	Outer rings	-1.95×10^{-3}	<0.05*	-1.99×10^{-3}	<0.05*
	Superior	-1.54×10^{-3}	<0.05*	-1.33×10^{-3}	<0.05*
	Inferior	-1.69×10^{-3}	<0.05*	-8.65×10^{-4}	>0.05
	Nasal	-1.96×10^{-3}	<0.05*	-2.04×10^{-3}	<0.05*
	Temporal	-1.64×10^{-3}	<0.05*	-2.00×10^{-3}	<0.05*
Continuous Reflectance Index (RI)	All rings	-1.37×10^{-3}	<0.05*	-2.80×10^{-3}	<0.05*
	Inner rings	-1.29×10^{-3}	<0.05*	-2.72×10^{-3}	<0.05*
	Outer rings	-1.43×10^{-3}	<0.05*	-2.86×10^{-3}	<0.05*
	Superior	-1.99×10^{-3}	<0.05*	-3.40×10^{-3}	<0.05*
	Inferior	-1.43×10^{-3}	<0.05*	-3.62×10^{-3}	<0.05*
	Nasal	-1.01×10^{-3}	<0.05*	-1.71×10^{-3}	<0.05*
	Temporal	-1.03×10^{-3}	>0.05	-2.37×10^{-3}	<0.05*
Birefringence	All rings	7.79×10^{-5}	>0.05	4.05×10^{-4}	>0.05
	Inner rings	7.26×10^{-5}	>0.05	3.88×10^{-4}	>0.05
	Outer rings	9.93×10^{-5}	>0.05	4.86×10^{-4}	<0.05*
	Superior	1.71×10^{-4}	>0.05	-1.37×10^{-5}	>0.05
	Inferior	-7.86×10^{-5}	>0.05	1.07×10^{-3}	<0.05*
	Nasal	2.25×10^{-4}	>0.05	-1.24×10^{-4}	>0.05
	Temporal	-7.73×10^{-7}	>0.05	2.10×10^{-3}	<0.05*
Phase Retardation	All rings	-7.01×10^{-3}	>0.05	-7.73×10^{-3}	>0.05
	Inner rings	-3.14×10^{-3}	>0.05	-5.43×10^{-3}	>0.05
	Outer rings	-1.29×10^{-2}	>0.05	-4.52×10^{-3}	>0.05
	Superior	2.58×10^{-2}	>0.05	-4.58×10^{-2}	>0.05
	Inferior	-3.67×10^{-2}	>0.05	6.28×10^{-3}	>0.05
	Nasal	-3.27×10^{-2}	>0.05	-1.17×10^{-2}	>0.05
	Temporal	4.37×10^{-2}	>0.05	6.63×10^{-2}	>0.05

Table 5.3 RNFL parameters in segmented regions versus number of days for primate 2 analyzed with a linear mixed model.

RNFL Parameter	Feature	Primate 2			
		Control		Treated	
		Slope	p (slope)	Slope	p (slope)
Clustered Thickness	All rings	1.54×10^{-2}	>0.05	1.01 x 10-1	<0.05*
	Inner rings	5.75×10^{-2}	>0.05	1.73×10^{-1}	<0.05*
	Outer rings	-3.74×10^{-2}	>0.05	5.76×10^{-2}	>0.05
	Superior	1.59×10^{-1}	>0.05	5.50×10^{-2}	>0.05
	Inferior	-2.64×10^{-2}	>0.05	1.67×10^{-1}	<0.05*
	Nasal	-1.68×10^{-2}	>0.05	8.62×10^{-2}	<0.05*
	Temporal	-3.10×10^{-2}	>0.05	1.11×10^{-2}	>0.05
Continuous Thickness	All rings	-1.87×10^{-2}	>0.05	4.50×10^{-2}	>0.05
	Inner rings	-1.30×10^{-2}	>0.05	5.26×10^{-2}	>0.05
	Outer rings	-2.39×10^{-2}	>0.05	4.02×10^{-2}	>0.05
	Superior	2.13×10^{-2}	>0.05	1.82×10^{-2}	>0.05
	Inferior	-7.32×10^{-2}	>0.05	8.36×10^{-2}	>0.05
	Nasal	-3.44×10^{-2}	>0.05	2.25×10^{-2}	>0.05
	Temporal	6.70×10^{-3}	>0.05	3.25×10^{-2}	>0.05
Clustered Reflectance Index (RI)	All rings	-4.95×10^{-4}	>0.05	-1.63×10^{-3}	<0.05*
	Inner rings	1.49×10^{-4}	>0.05	-1.36×10^{-3}	<0.05*
	Outer rings	-9.90×10^{-4}	<0.05*	-1.85×10^{-3}	<0.05*
	Superior	-7.25×10^{-4}	>0.05	-1.45×10^{-3}	<0.05*
	Inferior	-2.22×10^{-4}	>0.05	-1.65×10^{-3}	<0.05*
	Nasal	-3.66×10^{-4}	>0.05	-1.56×10^{-3}	<0.05*
	Temporal	-6.84×10^{-4}	>0.05	-1.79×10^{-3}	<0.05*
Continuous Reflectance Index (RI)	All rings	-1.02×10^{-3}	<0.05*	-1.90×10^{-3}	<0.05*
	Inner rings	-1.11×10^{-3}	<0.05*	-1.70×10^{-3}	<0.05*
	Outer rings	-9.47×10^{-4}	<0.05*	-2.07×10^{-3}	<0.05*
	Superior	-1.56×10^{-3}	<0.05*	-2.25×10^{-3}	<0.05*
	Inferior	-3.00×10^{-4}	>0.05	-1.80×10^{-3}	<0.05*
	Nasal	-1.10×10^{-3}	>0.05	-2.27×10^{-3}	<0.05*
	Temporal	-1.12×10^{-3}	<0.05*	-1.28×10^{-3}	<0.05*
Birefringence	All rings	1.05×10^{-5}	>0.05	-1.03×10^{-4}	>0.05
	Inner rings	-5.75×10^{-5}	>0.05	-1.85×10^{-4}	>0.05
	Outer rings	7.45×10^{-5}	>0.05	-3.92×10^{-5}	>0.05
	Superior	-6.26×10^{-5}	>0.05	-3.87×10^{-5}	>0.05
	Inferior	-9.25×10^{-5}	>0.05	2.93×10^{-5}	>0.05
	Nasal	1.31×10^{-4}	>0.05	-1.02×10^{-4}	>0.05
	Temporal	5.26×10^{-5}	>0.05	-2.44×10^{-4}	>0.05
Phase Retardation	All rings	-2.51×10^{-3}	>0.05	1.18×10^{-2}	>0.05
	Inner rings	-2.97×10^{-3}	>0.05	2.30×10^{-2}	>0.05
	Outer rings	-6.63×10^{-3}	>0.05	7.48×10^{-3}	>0.05
	Superior	3.10×10^{-2}	>0.05	6.94×10^{-3}	>0.05
	Inferior	-4.94×10^{-2}	>0.05	5.40×10^{-2}	>0.05
	Nasal	1.23×10^{-2}	>0.05	9.24×10^{-3}	>0.05
	Temporal	-4.54×10^{-3}	>0.05	-1.27×10^{-2}	>0.05

Table 5.4 RNFL parameters in segmented regions versus number of days for primate 3 analyzed with a linear mixed model.

RNFL Parameter	Feature	Primate 3			
		Control		Treated	
		Slope	p (slope)	Slope	p (slope)
Clustered Thickness	All rings	-3.74×10^{-2}	>0.05	-3.57×10^{-3}	>0.05
	Inner rings	-6.99×10^{-2}	>0.05	-2.14×10^{-3}	>0.05
	Outer rings	-9.70×10^{-3}	>0.05	-8.07×10^{-3}	>0.05
	Superior	-5.72×10^{-2}	>0.05	1.02×10^{-2}	>0.05
	Inferior	-2.64×10^{-2}	>0.05	-6.36×10^{-2}	>0.05
	Nasal	-4.10×10^{-2}	>0.05	8.72×10^{-3}	>0.05
	Temporal	1.37×10^{-2}	>0.05	1.71×10^{-2}	>0.05
Continuous Thickness	All rings	1.84×10^{-2}	>0.05	2.57×10^{-2}	>0.05
	Inner rings	1.18×10^{-2}	>0.05	3.24×10^{-2}	>0.05
	Outer rings	2.25×10^{-2}	>0.05	2.05×10^{-2}	>0.05
	Superior	2.01×10^{-3}	>0.05	-3.23×10^{-3}	>0.05
	Inferior	3.77×10^{-2}	>0.05	3.79×10^{-2}	>0.05
	Nasal	5.30×10^{-2}	<0.05*	3.56×10^{-2}	>0.05
	Temporal	-1.56×10^{-2}	>0.05	4.04×10^{-2}	>0.05
Clustered Reflectance Index (RI)	All rings	-1.01×10^{-3}	>0.05	-1.65×10^{-3}	<0.05*
	Inner rings	-8.48×10^{-4}	>0.05	-1.58×10^{-3}	<0.05*
	Outer rings	-1.13×10^{-3}	>0.05	-1.69×10^{-3}	<0.05*
	Superior	-1.07×10^{-3}	>0.05	-1.79×10^{-3}	<0.05*
	Inferior	-1.01×10^{-3}	>0.05	-1.37×10^{-3}	<0.05*
	Nasal	-9.98×10^{-4}	>0.05	-1.71×10^{-3}	<0.05*
	Temporal	-9.16×10^{-4}	>0.05	-1.48×10^{-3}	<0.05*
Continuous Reflectance Index (RI)	All rings	-1.20×10^{-3}	<0.05*	-1.33×10^{-3}	<0.05*
	Inner rings	-1.23×10^{-3}	<0.05*	-1.60×10^{-3}	<0.05*
	Outer rings	-1.18×10^{-3}	<0.05*	-1.14×10^{-3}	<0.05*
	Superior	-1.02×10^{-3}	>0.05	-1.47×10^{-3}	<0.05*
	Inferior	-9.63×10^{-4}	>0.05	-1.17×10^{-3}	>0.05
	Nasal	-1.08×10^{-3}	>0.05	-1.86×10^{-3}	<0.05*
	Temporal	-1.74×10^{-3}	<0.05*	-8.76×10^{-4}	>0.05
Birefringence	All rings	7.62×10^{-5}	>0.05	-2.39×10^{-4}	>0.05
	Inner rings	1.27×10^{-4}	>0.05	-3.11×10^{-4}	>0.05
	Outer rings	3.09×10^{-5}	>0.05	-1.75×10^{-4}	>0.05
	Superior	-2.06×10^{-5}	>0.05	-2.66×10^{-4}	>0.05
	Inferior	-3.29×10^{-5}	>0.05	-3.40×10^{-5}	>0.05
	Nasal	1.54×10^{-4}	>0.05	-3.68×10^{-4}	>0.05
	Temporal	2.74×10^{-4}	<0.05*	-2.81×10^{-4}	>0.05
Phase Retardation	All rings	-3.87×10^{-3}	>0.05	-3.35×10^{-2}	>0.05
	Inner rings	-5.86×10^{-3}	>0.05	-5.36×10^{-2}	>0.05
	Outer rings	-1.83×10^{-3}	>0.05	-1.67×10^{-2}	>0.05
	Superior	-1.75×10^{-2}	>0.05	-4.84×10^{-2}	>0.05
	Inferior	-2.16×10^{-2}	>0.05	-1.57×10^{-2}	>0.05
	Nasal	3.94×10^{-3}	>0.05	-3.39×10^{-2}	>0.05
	Temporal	4.01×10^{-2}	<0.05*	-3.65×10^{-2}	>0.05

5.3 ANALYSIS OF RNFL PARAMETER VERSUS IOP DAMAGE INTEGRAL

To evaluate change of RNFL parameters with respect to IOP exposure, we fit the difference between control and the treated eyes of RNFL parameters as a function of IOP damage integral using a linear mixed effects model. Inasmuch as significant trends might emerge in isolated regions of the eyes, retinal maps were segmented and RNFL parameters in each segment was analyzed separately in addition to parameter averages over the entire retina. RNFL parameters were computed and averaged in segmented regions including four inner rings, four outer rings, superior, inferior, nasal, and temporal quadrants and plotted both over both time and IOP damage integral. Fits were performed in each segmented region for all three primates combined (Table 5.5) and for individual primates (Table 5.6).

Difference in RNFL thickness, phase retardation, birefringence and reflectance index (RI) are plotted (Figures 5.14-5.19) for all usable clusters with all primates combined. No significant trend is observed ($p>0.05$) in the difference of RNFL thickness, phase retardation and birefringence between control and treated eyes vs. IOP damage integral. For both clustered and continuous ring scan data, difference between the RNFL reflectance index (RI) of control and treated eyes increases significantly when IOP damage integral increases ($p<0.05$ for both).

Using a linear mixed effects model, RNFL parameters (thickness, phase retardation, birefringence, and reflectance index) averaged in various segmented regions (all rings, inner rings, outer rings, superior, inferior, nasal, and temporal quadrants) were evaluated versus the IOP damage integral (Figures 5.14-5.19). For all RNFL thickness

measurements in each segmented region, only the nasal quadrant showed a significant change. The inferior quadrant showed a significant change for both RNFL phase retardation and birefringence.

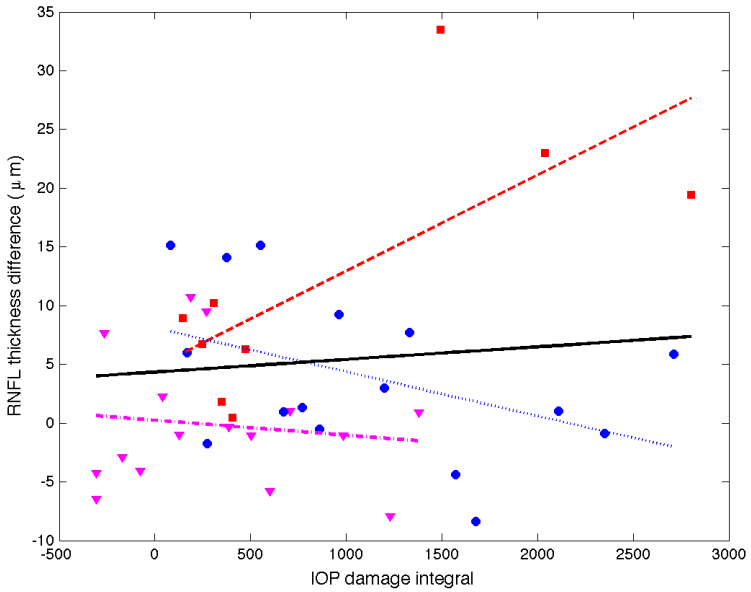

Figure 5.14. Average (all rings) of RNFL thickness difference (control less treated) for clustered retinal scans vs. IOP damage integral (squares primate 1; circles primate 2; and triangles are primate 3). Linear mixed model fits for individual primates (colored lines) and combined (all primates, black).

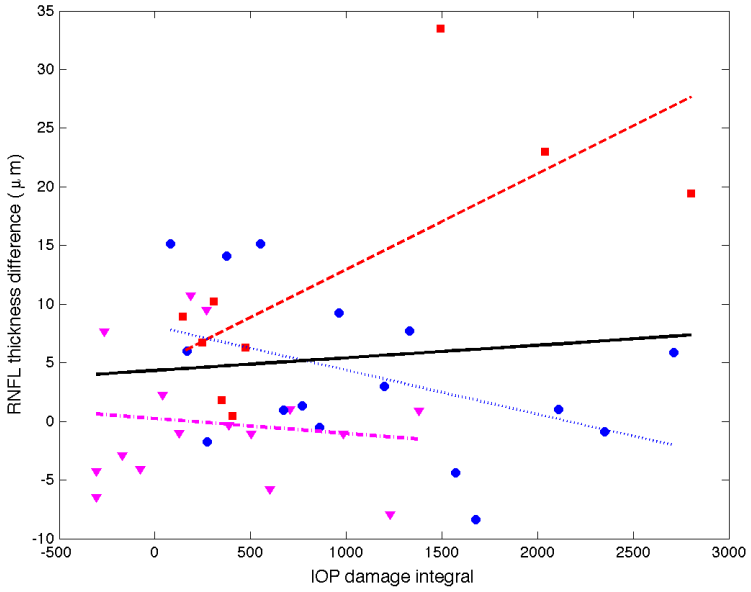

Figure 5.15. Average (all rings) of RNFL thickness difference (control less treated) for continuous retinal scans vs. IOP damage integral (squares primate 1; circles primate 2; and triangles are primate 3). Linear mixed model fits for individual primates (colored lines) and combined (all primates, black).

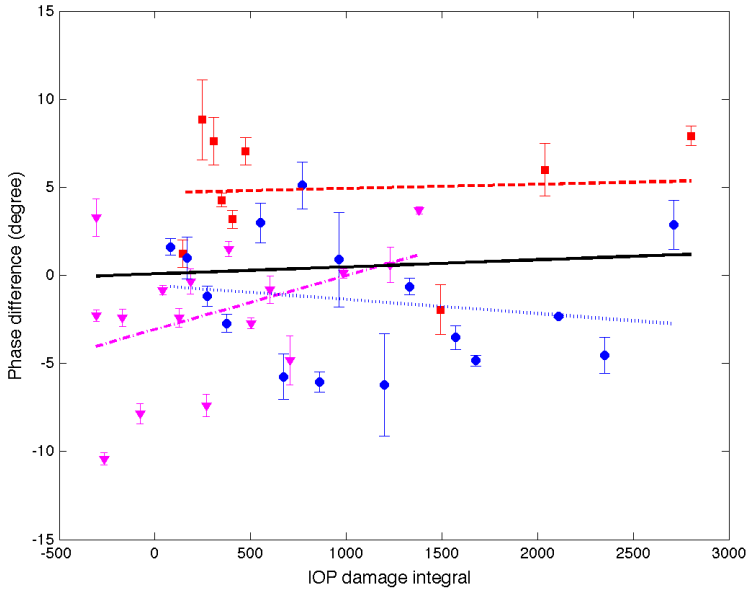

Figure 5.16. Average (all rings) of phase retardation difference (control less treated) for clustered retinal scans vs. IOP damage integral (squares primate 1; circles primate 2; and triangles are primate 3). Linear mixed model fits for individual primates (colored lines) and combined (all primates, black)

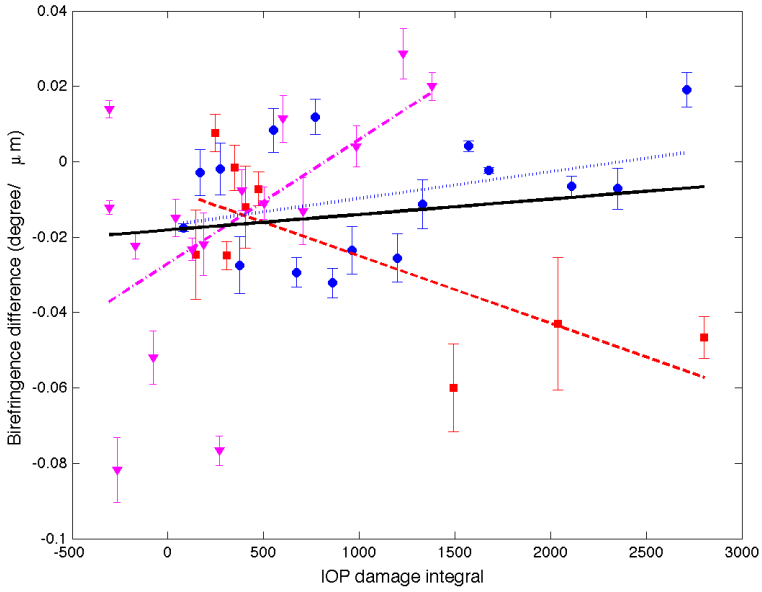

Figure 5.17. Average (all rings) of birefringence difference (control less treated) for clustered retinal scans vs. IOP damage integral (squares primate 1; circles primate 2; and triangles are primate 3). Linear mixed model fits for individual primates (colored lines) and combined (all primates, black).

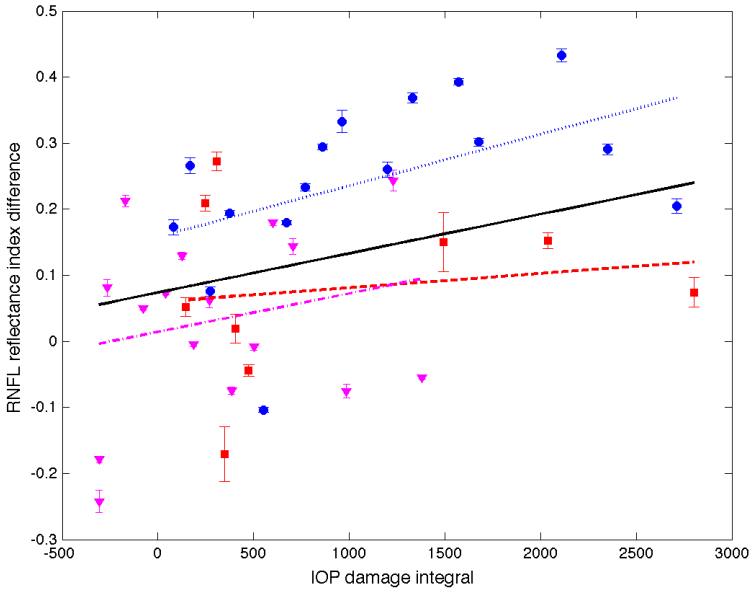

Figure 5.18. Average (all rings) of RNFL reflectance index (RI) difference (control less treated) for clustered retinal scans vs. IOP damage integral (squares primate 1; circles primate 2; and triangles are primate 3). Linear mixed model fits for individual primates (colored lines) and combined (all primates, black).

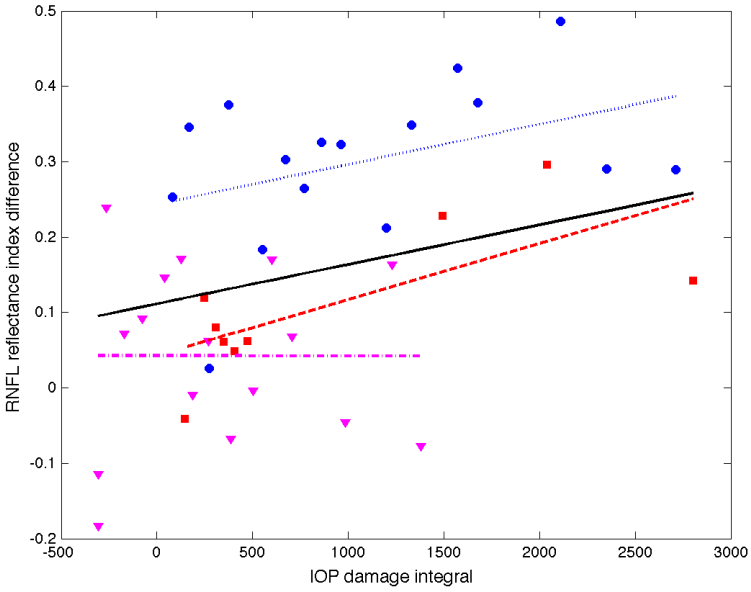

Figure 5.19. Average (all rings) of RNFL reflectance index (RI) difference (control less treated) for continuous retinal scans vs. IOP damage integral (squares primate 1; circles primate 2; and triangles are primate 3). Linear mixed model fits for individual primates (colored lines) and combined (all primates, black).

Table 5.5 RNFL parameter differences (control less treated) in segmented regions versus IOP damage integral for all primates analyzed with a linear mixed effects model.

RNFL Parameter	Region	Slope	p(slope)
Clustered Thickness	All rings	-4.52×10^{-4}	>0.05
	Inner ring	-2.47×10^{-3}	>0.05
	Outer ring	2.16×10^{-4}	>0.05
	Superior	4.81×10^{-3}	>0.05
	Inferior	2.75×10^{-3}	>0.05
	Nasal	-6.83×10^{-3}	<0.05*
	Temporal	4.39×10^{-3}	>0.05
Continuous Thickness	All rings	1.07×10^{-3}	>0.05
	Inner ring	9.30×10^{-4}	>0.05
	Outer ring	1.27×10^{-3}	>0.05
	Superior	2.36×10^{-3}	>0.05
	Inferior	3.22×10^{-3}	>0.05
	Nasal	1.88×10^{-3}	>0.05
	Temporal	-3.06×10^{-3}	>0.05
Phase Retardation	All rings	3.97×10^{-4}	>0.05
	Inner ring	5.49×10^{-4}	>0.05
	Outer ring	-8.01×10^{-5}	>0.05
	Superior	2.72×10^{-3}	>0.05
	Inferior	-3.42×10^{-3}	<0.05*
	Nasal	4.07×10^{-4}	>0.05
	Temporal	1.62×10^{-3}	>0.05
Birefringence	All rings	4.11×10^{-6}	>0.05
	Inner ring	8.03×10^{-6}	>0.05
	Outer ring	2.10×10^{-7}	>0.05
	Superior	7.40×10^{-6}	>0.05
	Inferior	-2.45×10^{-5}	<0.05*
	Nasal	2.26×10^{-5}	<0.05*
	Temporal	-1.94×10^{-5}	>0.05
Clustered Reflectance Index (RI)	All rings	5.93×10^{-5}	<0.05*
	Inner ring	6.30×10^{-5}	>0.05
	Outer ring	5.98×10^{-5}	<0.05*
	Superior	4.99×10^{-5}	>0.05
	Inferior	5.55×10^{-5}	>0.05
	Nasal	7.22×10^{-5}	<0.05*
	Temporal	6.77×10^{-5}	<0.05*
Continuous Reflectance Index (RI)	All rings	5.23×10^{-5}	<0.05*
	Inner ring	4.89×10^{-5}	>0.05
	Outer ring	5.58×10^{-5}	<0.05*
	Superior	5.39×10^{-5}	>0.05
	Inferior	8.89×10^{-5}	<0.05*
	Nasal	6.36×10^{-5}	<0.05*
	Temporal	8.42×10^{-6}	>0.05

Table 5.6 RNFL parameter differences (control less treated) in segmented regions versus IOP damage integral for individual primates analyzed with a linear mixed model.

RNFL Parameter	Feature	Primate 1		Primate 2		Primate 3	
		Slope	p (slope)	Slope	p (slope)	Slope	p (slope)
Clustered Thickness	Entire ring	7.41×10^{-3}	<0.05*	-5.18×10^{-3}	>0.05	-3.62×10^{-3}	>0.05
	Inner ring	6.15×10^{-3}	<0.05*	-6.94×10^{-3}	>0.05	-7.49×10^{-3}	>0.05
	Outer ring	7.72×10^{-3}	<0.05*	-5.78×10^{-3}	<0.05*	-4.98×10^{-5}	>0.05
	Superior	9.69×10^{-3}	>0.05	6.56×10^{-3}	>0.05	-7.03×10^{-3}	>0.05
	Inferior	2.17×10^{-2}	<0.05*	-1.21×10^{-2}	<0.05*	2.77×10^{-3}	>0.05
	Nasal	-8.60×10^{-3}	>0.05	-6.21×10^{-3}	<0.05*	-5.04×10^{-3}	>0.05
	Temporal	2.09×10^{-2}	<0.05*	-8.27×10^{-3}	>0.05	-6.90×10^{-4}	>0.05
Continuous Thickness	Entire ring	8.16×10^{-3}	<0.05*	-3.73×10^{-3}	>0.05	-1.27×10^{-3}	>0.05
	Inner ring	9.08×10^{-3}	<0.05*	-3.85×10^{-3}	>0.05	-2.67×10^{-3}	>0.05
	Outer ring	7.41×10^{-3}	<0.05*	-3.76×10^{-3}	>0.05	-2.71×10^{-4}	>0.05
	Superior	3.43×10^{-3}	>0.05	4.89×10^{-4}	>0.05	5.49×10^{-5}	>0.05
	Inferior	2.12×10^{-2}	<0.05*	-9.51×10^{-3}	<0.05*	-1.21×10^{-3}	>0.05
	Nasal	9.42×10^{-3}	<0.05*	-3.43×10^{-3}	>0.05	1.05×10^{-3}	>0.05
	Temporal	-3.86×10^{-3}	>0.05	-1.40×10^{-3}	>0.05	-5.38×10^{-3}	<0.05*
Clustered Reflectance Index (RI)	Entire ring	8.67×10^{-7}	>0.05	6.89×10^{-5}	<0.05*	4.95×10^{-5}	>0.05
	Inner ring	-7.67×10^{-6}	>0.05	9.07×10^{-5}	<0.05*	5.27×10^{-5}	>0.05
	Outer ring	-6.85×10^{-6}	>0.05	5.33×10^{-5}	<0.05*	4.69×10^{-5}	>0.05
	Superior	-1.22×10^{-5}	>0.05	4.35×10^{-5}	>0.05	5.91×10^{-5}	>0.05
	Inferior	-4.72×10^{-5}	>0.05	8.74×10^{-5}	<0.05*	2.32×10^{-5}	>0.05
	Nasal	1.88×10^{-6}	>0.05	7.31×10^{-5}	<0.05*	5.25×10^{-5}	>0.05
	Temporal	2.00×10^{-5}	>0.05	6.65×10^{-5}	<0.05*	3.80×10^{-5}	>0.05
Continuous Reflectance Index (RI)	Entire ring	7.41×10^{-5}	<0.05*	5.30×10^{-5}	>0.05	-5.20×10^{-7}	>0.05
	Inner ring	7.65×10^{-5}	<0.05*	3.60×10^{-5}	>0.05	1.77×10^{-5}	>0.05
	Outer ring	7.23×10^{-5}	<0.05*	6.72×10^{-5}	>0.05	-1.35×10^{-5}	>0.05
	Superior	6.80×10^{-5}	>0.05	4.24×10^{-5}	>0.05	4.12×10^{-5}	>0.05
	Inferior	1.31×10^{-4}	<0.05*	8.76×10^{-5}	>0.05	-7.55×10^{-6}	>0.05
	Nasal	3.74×10^{-5}	>0.05	7.14×10^{-5}	>0.05	7.08×10^{-5}	>0.05
	Temporal	5.24×10^{-5}	>0.05	9.32×10^{-6}	>0.05	-9.84×10^{-5}	>0.05
Birefringence	Entire ring	-1.79×10^{-5}	<0.05*	7.13×10^{-6}	>0.05	3.29×10^{-5}	<0.05*
	Inner ring	-1.72×10^{-5}	>0.05	8.15×10^{-6}	>0.05	4.57×10^{-5}	<0.05*
	Outer ring	-2.04×10^{-5}	<0.05*	6.95×10^{-6}	>0.05	2.17×10^{-5}	>0.05
	Superior	5.30×10^{-6}	>0.05	-1.36×10^{-6}	>0.05	2.49×10^{-5}	>0.05
	Inferior	-6.48×10^{-5}	<0.05*	-7.13×10^{-6}	>0.05	2.19×10^{-6}	>0.05
	Nasal	1.91×10^{-5}	>0.05	1.43×10^{-5}	<0.05*	5.25×10^{-5}	<0.05*
	Temporal	-1.12×10^{-4}	<0.05*	1.82×10^{-5}	>0.05	5.84×10^{-5}	<0.05*
Phase Retardation	Entire ring	2.42×10^{-4}	>0.05	-7.98×10^{-4}	>0.05	3.08×10^{-3}	>0.05
	Inner ring	2.84×10^{-4}	>0.05	-1.45×10^{-3}	>0.05	4.92×10^{-3}	>0.05
	Outer ring	-1.15×10^{-4}	>0.05	-8.60×10^{-4}	>0.05	1.60×10^{-3}	>0.05
	Superior	3.84×10^{-3}	>0.05	1.63×10^{-3}	>0.05	2.92×10^{-3}	>0.05
	Inferior	-2.02×10^{-3}	>0.05	-6.35×10^{-3}	<0.05*	-2.45×10^{-4}	>0.05
	Nasal	-1.04×10^{-3}	>0.05	2.38×10^{-4}	>0.05	3.71×10^{-3}	>0.05
	Temporal	-7.64×10^{-4}	>0.05	6.30×10^{-4}	>0.05	7.89×10^{-3}	<0.05*

We analyze RI versus IOP damage integral using a non-linear model (Figure 22). We use Akaike information criterion (AIC) and Bayesian information criterion (BIC) values to compare the non-linear model and the linear model. Because AIC and BIC values derived from the nonlinear model (clustered: AIC=-39.4, BIC=-30.8; continuous: AIC=-52.0,BIC=-43.4) are smaller than those of the linear model (clustered: AIC=-16.6, BIC=-9.9; continuous: AIC=-37.8, BIC=-31.2), we conclude that the nonlinear model provides a better fit to RI data compared to the linear model.

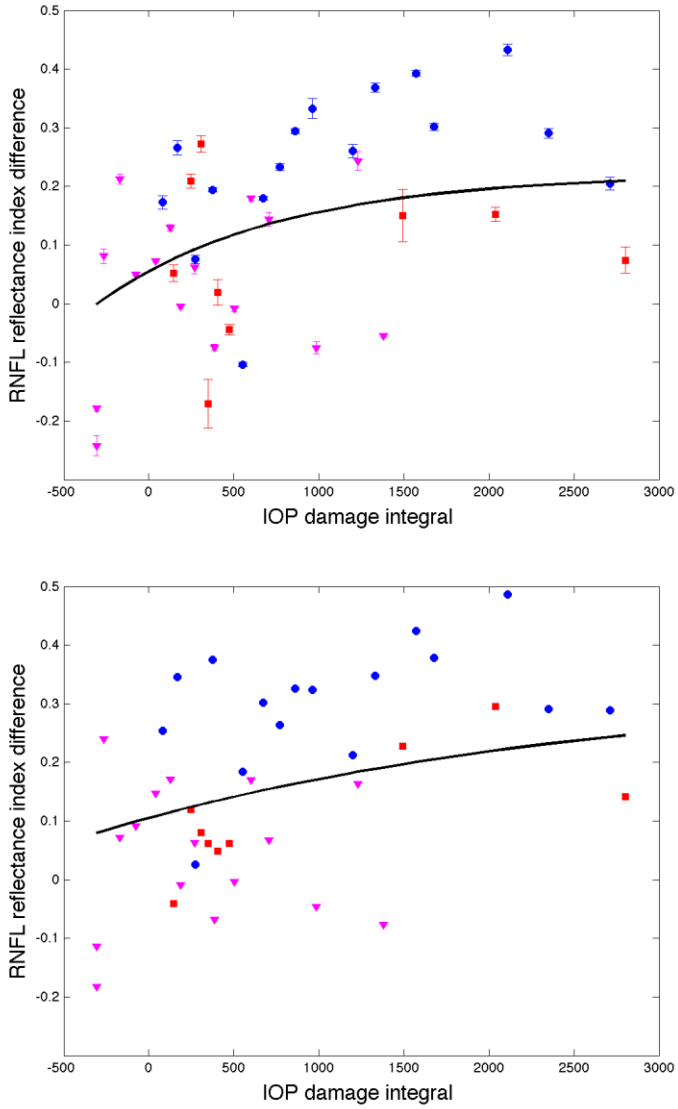

Figure 5.20. Average (all rings) of RNFL reflectance index (*RI*) difference (control less treated) for clustered (top) and continuous (bottom) retinal scans vs. IOP damage integral (squares primate 1; circles primate 2; and triangles are primate 3). Nonlinear mixed effects model fits (black curves) for clustered (τ =1060.4, AIC=-39.4, BIC=-30.8) and continuous (τ =2848.3, AIC=-52.0, BIC=-43.4) data for all primates.

5.4 DISCUSSION

In this study, the clearest measured indicator of retinal changes from elevated IOP was a decrease in the retinal RI as defined above. Significant changes in the RI were observed in half of the quadrants in the eyes, in the overall average values of the eyes and in the outer rings. Significant changes were observed in the RI for both the control and treated eyes as seen using the linear fits of the RI with number of days. In these fits, the slope was higher for the treated eye. It is possible that the frequent anesthesia needed to perform these experiments on a regular basis was responsible for the decreased RI in the control eyes. Mitochondrial changes are proposed as a possible mechanism for reduced retinal reflectance and mitochondrial changes are a documented effect of anesthesia exposure [47].

Although previous studies have found an RNFL thinning effect as a result of elevated IOP, this was observed in the current study only in the nasal region (the thinnest RNFL region) using the clustered thickness data. Considering the lower values of IOP utilized in this study compared to previous investigations, absence of much RNFL thinning is understandable. In this sense, this result can be viewed as complementary, not contradictory to previous studies. Phase retardation and birefringence changes were detected in the course of this study only in the inferior quadrant of the eyes. These effects should be considered as potential markers in subsequent investigations.

This is not the first study to observe reflectance changes in the retina, however it is the first known definition of the reflectance change observed with OCT and the first indication that the reflectance change is observable in glaucomatous primates [48, 49]. Additional investigation is necessary to test and identify the mechanisms for RNFL reflectance changes although changes in the mitochondrial networks and axonal

cytoskeleton changes are possible mechanisms. Previous studies have demonstrated changes in the mitochondrial membrane permeability in response to elevated pressure and have shown this to precede retinal ganglion cell loss in glaucomatous eyes [50, 51].

Mitochondria are recognized as providing a primary component to the reduced scattering coefficient of cells [52, 53]. Contribution of mitochondria to the reduced scattering coefficient is greatest in tissues (e.g., brain and liver) with dense mitochondrial populations [52]. In view of Mie theory and the physical principles of light scattering [53], the contribution of mitochondria to RNFL scattering strength is dependent on the spatial dimensions (or Fractal dimension) of the mitochondrial networks in neural axons. Mitochondrial dysfunction is recognized as an important component in the etiology of neurodegenerative pathologies including amyotrophic lateral sclerosis, Alzheimer's and Parkinson's disease. Mitochondria are recognized as dynamic organelles that constantly undergo fusion and fission processes that are required to maintain normal cell function. Fusion of mitochondria to form interconnected intracellular networks is believed to be a necessary component to maintain a mitochondrial population with a full complement of gene products that can mitigate age-related degeneration. In fact, autosomal dominant optic atrophy the leading cause of childhood blindness is caused by a mutation in the mitochondrial fusion genes OPA1.

Recently Ju et al. demonstrated that mitochondria fission in differentiated retinal ganglion cell cultures is induced in response to elevated hydrostatic pressures [54]. A number of recent studies have observed optical scattering changes in cells undergoing apoptosis that originate at least in part to the mitochondria. Pasternack et al. used a Fourier microscopy approach to demonstrate that early cell apoptosis is accompanied by

mitochondrial fission and fragmentation that results in more isotropic or large-angle light scattering [55]. Chalut et al. utilized angle-resolved OCT to document similar scattering changes that may involve mitochondrial fission [56]. A number of investigators have recently applied OCT to document light scattering changes in cells undergoing apoptosis or necrosis [57, 58]. Observed reduction in RI in glaucomatous primate eyes reported here is consistent with reduced backscatter due to increased mitochondrial fission resulting in increased large angle scattering. Increased mitochondrial fission is an important feature of early stages of apoptosis. Inasmuch as other mechanisms such as decreased density of mitochondria may contribute to the observed decrease in RNFL reflectance, additional studies are required to isolate and characterize this and other candidate cellular processes.

5.5 FUTURE DIRECTIONS

5.5.1 Instrumentation changes

We are satisfied with the performance of this system for taking measurements in the retina of these primates however the SNR of this system did put some limitations on the quality of the data. In large part the noise level in this system is thought to be due to the high-frequency laser noise discussed previously and shown in figure 2.13. This is a commercially available source, so there isn't much that we could do about this noise except to have the laser cavity re-aligned by the manufacturer. Another source by the same manufacturer, used by colleagues, does not show the same noise characteristics so it is not thought to be a flaw inherent in the design.

Another source of noise in this system is the amount of non-signal light that is coupled into the detection path. In our system the interference of the sample and reference light occurs at the main 50/50 beam splitter. Both the sample and reference paths operate in double pass so any misalignment in the optics of these paths means that there will be imperfect interference at the beamsplitter. Some of this non-interfered light is still accepted into the detection optics and directed onto the detectors. Care is taken to overlap these beams as much as possible when aligning the sample and reference path however it might be possible to lower the noise level by utilizing an aperture to further reduce the amount of non-signal light from coupling into the detection path.

5.5.2 Study design

In so far as this study indicates the value of using a measure of retinal reflectance as an indicator of early glaucomatous damage, there is reason for additional study to be performed in this area to further validate the technique and to refine the methods.

As discussed previously there is reason to believe that part of the reason for the measured change in reflectance is the changes in mitochondria associated with increased pressure or other mechanisms that signal apoptosis. This theory needs to be further investigated. At the end of this study, the primates were euthanized with a perfusion technique for whole body fixation in an effort to preserve the retinal tissue immediately upon death. Some insight could be gained into the mechanism of the reflectance change with TEM histology on these eyes. While we saw RI changes in both the control eyes and the treated eyes, there was a significantly larger change in the treated eyes. From the

theory, we would expect to see associated changes in the mitochondrial densities of these retinas.

In addition there is a need for theoretical validation of the theory that the amplitude of the reflectance changes could be associated with changes in the mitochondria. We have seen in previous literature [58, 59] that changes in the mitochondria affect the scattering angle of retinal tissue but this has not been correlated to the magnitude of retinal reflectance changes that we found in the course of this study. Some work has been done to model light interaction with retinal tissue [60, 61] and this work could form a basis for a theoretical analysis of the loss of retinal mitochondria and the associated changes in retinal reflectance intensity.

One of the shortcomings of this study was the lack of measured changes in the thickness and/or polarization properties of the retina. Previous studies have shown that these changes do exist and we expect that as the disease progressed further, these changes would have been observed in the primates however the frequency of the procedures on the animals and the need for anesthesia at each procedure precluded the extension of this study for a longer time period. It would be beneficial to monitor the changes in the retina at these lower IOP values over an extended period of time to have a better picture of the typical changes in the retina as the disease progresses. As the RGC's die and the microtubules reced, leaving increased concentration of glial tissue it is possible that the reflectance of the retina increases again. In order to accomplish a longer study, appropriate intervals would need to be put into place. Because of the low IOP increases, used in this study, we didn't see rapid changes in the retina that are associated with

higher IOP studies and the frequency of the procedures could have been reduced without missing any significant events.

REFERENCES

1. Resnikoff, S, Pascolini, D, Etya'ale, D, Kocur, I, Pararajasegaram, R, Pokharel, GP, Mariotti, SP, *Global Data on Visual Impairment in the Year 2002*, Bull. World Health Organ., 82 (2004) 844-851.
2. Friedman, DS, Wolfs, RCW, O'colmain, BJ, Klein, BE, Taylor, HR, West, S, Leske, MC, Mitchell, P, Congdon, N, Kempen, J, *Prevalence of Open-Angle Glaucoma among Adults in the United States*, Arch. Ophthalmol., 122 (2004) 532-538.
3. Wong, TY, Hyman, L, *Population-Based Studies in Ophthalmology*, Am. J. Ophthalmol., 146 (2008) 656-663.
4. *Eye Ultrastructure*,Wagner, R, Hossler, F,University of Delaware,November 14, 2011,<http://www.udel.edu/biology/Wags/histopage/empage/eey/eey.htm>
5. Quigley, H, Addicks, E, Green, W, *Optic Nerve Damage in Human Glaucoma: Iii. Quantitative Correlation of Nerve Fiber Loss and Visual Field Defect in Glaucoma, Ischemic Neuropathy, Papilledema, and Toxic Neuropathy*, Arch. Ophthalmol., 100 (1982) 135-146.
6. Agarwal, R, Gupta, SK, Agarwal, P, Saxena, R, Agrawal, SS, *Current Concepts in the Pathophysiology of Glaucoma*, Indian J. Ophthalmol., 57 (2009) 257-266.
7. Stroman, G, Stewart, W, Golnik, K, Cure, J, Re, O, *Magnetic-Resonance-Imaging in Patients with Low-Tension Glaucoma*, Arch. Ophthalmol., 113 (1995) 168-172.
8. Hernandez, M, Pena, J, *The Optic Nerve Head in Glaucomatous Optic Neuropathy*, Arch. Ophthalmol., 115 (1997) 389-395.
9. Wax, M, Tezel, G, *Neurobiology of Glaucomatous Optic Neuropathy - Diverse Cellular Events in Neurodegeneration and Neuroprotection*, Mol. Neurobiol., 26 (2002) 45-55.
10. Grus, FH, Joachim, SC, Wuenschig, D, Rieck, J, Pfeiffer, N, *Autoimmunity and Glaucoma*, J. Glaucoma, 17 (2008) 79-84.
11. Wax, M, *Is There a Role for the Immune System in Glaucomatous Optic Neuropathy?*, Curr. Opin. Ophthalmol., 11 (2000) 145-150.
12. Quigley, H, Nickells, R, Kerrigan, L, Pease, M, Thibault, D, Zack, D, *Retinal Ganglion Cell Death in Experimental Glaucoma and after Axotomy Occurs by Apoptosis*, Invest Ophth Visual, 36 (1995) 774.
13. Dielemans, I, Vingerling, JR, Wolfs, RC, Hofman, A, Grobbee, DE, De Jong, PT, *The Prevalence of Primary Open-Angle Glaucoma in a Population-Based Study in the Netherlands. The Rotterdam Study*, Ophthalmology, 101 (1994) 1851-1855.
14. Klein, BE, Klein, R, Sponsel, WE, Franke, T, Cantor, LB, Martone, J, Menage, MJ, *Prevalence of Glaucoma. The Beaver Dam Eye Study*, Ophthalmology, 99 (1992) 1499-1504.
15. Bonomi, L, Marchini, G, Marraffa, M, Bernardi, P, De Franco, I, Perfetti, S, Varotto, A, Tenna, V, *Prevalence of Glaucoma and Intraocular Pressure Distribution in a Defined Population - the Egna-Neumarkt Study*, Ophthalmology, 105 (1998) 209-215.

16. Ophthalmology, AaO, *Primary Open-Angle Glaucoma, Preferred Practice Pattern*, in: San Francisco: American Academy of Ophthalmology, 2005.
17. Weinreb, RN, Friedman, D, Fechtner, R, Cioffi, G, Coleman, A, Girkin, C, Liebmann, J, Singh, K, Wilson, M, Wilson, R, Kannel, W, *Risk Assessment in the Management of Patients with Ocular Hypertension*, Am. J. Ophthalmol., 138 (2004) 458-467.
18. Quigley, HA, Dunkelberger, GR, Green, WR, *Retinal Ganglion Cell Atrophy Correlated with Automated Perimetry in Human Eyes with Glaucoma*, Am. J. Ophthalmol., 107 (1989) 453-464.
19. Leeprechanon, N, Giaconi, JA, Manassakorn, A, Hoffman, D, Caprioli, J, *Frequency Doubling Perimetry and Short-Wavelength Automated Perimetry to Detect Early Glaucoma*, Ophthalmology, 114 (2007) 931-937.
20. Kelly, D, *Nonlinear Visual Responses to Flickering Sinusoidal Gratings*, J. Opt. Soc. Am., 71 (1981) 1051-1055.
21. Medeiros, F, Sample, P, Weinreb, R, *Frequency Doubling Technology Perimetry Abnormalities as Predictors of Glaucomatous Visual Field Loss*, Am. J. Ophthalmol., 137 (2004) 863-871.
22. Medeiros, F, Zangwill, L, Bowd, C, Weinreb, RN, *Comparison of the Gdx Vcc Scanning Laser Polarimeter, Hrt Ii Confocal Scanning Laser Ophthalmoscope, and Stratus Oct Optical Coherence Tomograph for the Detection of Glaucoma*, Arch. Ophthalmol., 122 (2004) 827-837.
23. Lalezary, M, Medeiros, FA, Weinreb, RN, Bowd, C, Sample, PA, Tavares, IM, Tafreshi, A, Zangwill, LM, *Baseline Optical Coherence Tomography Predicts the Development of Glaucomatous Change in Glaucoma Suspects*, Am. J. Ophthalmol., 142 (2006) 576-582.
24. Schuman, JS, Hee, M, Puliafito, C, Wong, C, Pedutkloizman, T, Lin, C, Hertzmark, E, Izatt, J, Swanson, EA, Fujimoto, JG, *Quantification of Nerve-Fiber Layer Thickness in Normal and Glaucomatous Eyes Using Optical Coherence Tomography - a Pilot Study*, Arch. Ophthalmol., 113 (1995) 586-596.
25. Sommer, A, Katz, J, Quigley, H, Miller, N, Robin, A, Richter, R, Witt, K, *Clinically Detectable Nerve-Fiber Atrophy Precedes the Onset of Glaucomatous Field Loss*, Arch. Ophthalmol., 109 (1991) 77-83.
26. Vessani, RM, Moritz, R, Batis, L, Zagui, RB, Bernardoni, S, Susanna, R, *Comparison of Quantitative Imaging Devices and Subjective Optic Nerve Head Assessment by General Ophthalmologists to Differentiate Normal from Glaucomatous Eyes*, J. Glaucoma, 18 (2009) 253-261.
27. Kanamori, A, Nagai-Kusuhara, A, Escano, M, Maeda, H, Nakamura, M, Negi, A, *Comparison of Confocal Scanning Laser Ophthalmoscopy, Scanning Laser Polarimetry and Optical Coherence Tomography to Discriminate Ocular Hypertension and Glaucoma at an Early Stage*, Graef Arch Clin Exp, 244 (2006) 58-68.
28. Schuman, JS, Wollstein, G, Farra, T, Hertzmark, E, Aydin, A, Fujimoto, JG, Paunescu, L, *Comparison of Optic Nerve Head Measurements Obtained by Optical Coherence Tomography and Confocal Scanning Laser Ophthalmoscopy*, Am. J. Ophthalmol., 135 (2003) 504-512.

29. Greaney, M, Hoffman, D, Garway-Heath, D, Nakla, M, Coleman, A, Caprioli, J, *Comparison of Optic Nerve Imaging Methods to Distinguish Normal Eyes from Those with Glaucoma*, Invest Ophth Visual, 43 (2002) 140-145.
30. Windisch, BK, Harasymowycz, PJ, See, JL, Chauhan, BC, Belliveau, AC, Hutchison, DM, Nicolela, MT, *Comparison between Confocal Scanning Laser Tomography, Scanning Laser Polarimetry and Optical Coherence Tomography on the Ability to Detect Localised Retinal Nerve Fibre Layer Defects in Glaucoma Patients*, Brit J Ophthalmol, 93 (2009) 225-230.
31. Huang, D, Swanson, EA, Lin, CP, Schuman, JS, Stinson, WG, Chang, W, Hee, MR, Flotte, T, Gregory, K, Puliafito, CA, *Optical Coherence Tomography*, Science, 254 (1991) 1178-1181.
32. *Largest Base of Optical Coherence Technology Worldwide with More Than 10,000 Units Installed*,10/18/2010,<http://www.meditec.zeiss.com/C1256A770030BCE0/WebViewTopNewsAllE/2D4B8A2D1E164576C12574C100317CFB?OpenDocument>
33. Fercher, AF, Hitzenberger, CK, Kamp, G, Elzaiat, S, *Measurement of Intraocular Distances by Backscattering Spectral Intereferometery*, Opt Commun, 117 (1995) 43-48.
34. Chinn, S, Swanson, EA, Fujimoto, JG, *Optical Coherence Tomography Using a Frequency-Tunable Optical Source*, Opt. Lett., (1997).
35. Nassif, N, Cense, B, Park, B, Pierce, M, Yun, S, *In Vivo High-Resolution Video-Rate Spectral-Domain Optical Coherence Tomography of the Human Retina …*, Opt Exp, (2004).
36. Zelmon, D, Small, D, Jundt, D, *Infrared Corrected Sellmeier Coefficients for Congruently Grown Lithium Niobate and 5 Mol. % Magnesium Oxide-Doped Lithium Niobate*, J Opt Soc Am B, 14 (1997) 3319-3322.
37. Santhanam, K, *Clock System Design for Quadrupling the Frequency of Reference Clock for a Swept Source Spectral Domain Optical Coherence Tomography*, MA Thesis. University of Texas, (2009).
38. Gaasterland, D, Kupfer, C, *Experimental Glaucoma in the Rhesus Monkey*, Invest. Ophthalmol. Vis. Sci., 13 (1974) 455-457.
39. Pederson, J, Gaasterland, D, *Laser-Induced Primate Glaucoma - Progression of Cupping*, Arch. Ophthalmol., 102 (1984) 1689-1692.
40. Quigley, HA, Hohman, RM, *Laser Energy Levels for Trabecular Meshwork Damage in the Primate Eye*, Invest. Ophthalmol. Vis. Sci., 24 (1983) 1305-1307.
41. Schuman, JS, Pedut-Kloizman, T, Pakter, H, Wang, N, Guedes, V, Huang, L, Pieroth, L, Scott, W, Hee, MR, Fujimoto, JG, Ishikawa, H, Bilonick, RA, Kagemann, L, Wollstein, G, *Optical Coherence Tomography and Histologic Measurements of Nerve Fiber Layer Thickness in Normal and Glaucomatous Monkey Eyes*, Invest. Ophthalmol. Vis. Sci., 48 (2007) 3645-3654.
42. Mujat, M, Chan, R, Cense, B, Park, B, Joo, C, Akkin, T, Chen, T, De Boer, JF, *Retinal Nerve Fiber Layer Thickness Map Determined from Optical Coherence Tomography Images*, Opt Exp, (2005).

43. Mayer, M, Hornegger, J, Mardin, C, Tornow, R, *Retinal Nerve Fiber Layer Segmentation on Fd-Oct Scans of Normal Subjects and Glaucoma Patients*, Biomedical Optics Express, (2010).
44. Wang, B, Paranjape, A, Yin, B, Liu, S, Markey, MK, Milner, TE, Rylander Iii, HG, *Optimized Retinal Nerve Fiber Layer Segmentation Based on Optical Reflectivity and Birefringence for Polarization-Sensitive Optical Coherence Tomography*, Proc. SPIE, (2011).
45. Liu, S, Dwelle, J, Ho, D, Milner, TE, Rylander, HG, Markey, MK, *Effect of Registration on Longitudinal Analysis of Retinal Nerve Fiber Layer Thickness of Non-Human Primates Using Oct*, in: Unpublished Manuscript, 2011.
46. Kemp, NJ, Park, J, Zaatari, HN, Rylander, HG, Milner, TE, *High-Sensitivity Determination of Birefringence in Turbid Media with Enhanced Polarization-Sensitive Optical Coherence Tomography*, J. Opt. Soc. Am. A, 22 (2005) 552-560.
47. Zhang, Y, Dong, Y, Wu, X, Lu, Y, Xu, Z, Knapp, A, Yue, Y, Xu, T, Xie, Z, *The Mitochondrial Pathway of Anesthetic Isoflurane-Induced Apoptosis*, J. Biol. Chem., 285 (2010) 4025-4037.
48. Zhang, X, Hu, J, Knighton, RW, Huang, X-R, Puliafito, CA, Jiao, S, *Dual-Band Spectral-Domain Optical Coherence Tomography for in Vivo Imaging the Spectral Contrasts of the Retinal Nerve Fiber Layer*, Opt Exp, 19 (2011) 19653-19659.
49. Huang, X, Zhou, Y, Kong, W, Knighton, RW, *Reflectance Decrease Prior to Thickness Change of the Retinal Nerve Fiber Layer in Glaucomatous Retinas*, Invest. Ophthalmol. Vis. Sci., (2011).
50. Mittag, TW, Danias, J, Pohorenec, G, Yuan, HM, Burakgazi, E, Chalmers-Redman, R, Podos, SM, Tatton, WG, *Retinal Damage after 3 to 4 Months of Elevated Intraocular Pressure in a Rat Glaucoma Model*, Invest. Ophthalmol. Vis. Sci., 41 (2000) 3451-3459.
51. Abu-Amero, KK, Morales, J, Bosley, TM, *Mitochondrial Abnormalities in Patients with Primary Open-Angle Glaucoma*, Invest. Ophthalmol. Vis. Sci., 47 (2006) 2533-2541.
52. Beauvoit, B, Evans, S, Jenkins, T, Miller, E, Chance, B, *Correlation between the Light Scattering and the Mitochondrial Content of Normal Tissues and Transplantable Rodent Tumors*, Annals of Biochemistry, (1995).
53. Mourant, J, Freyer, J, Hielscher, A, Eick, A, Shen, D, Johnson, T, *Mechanisms of Light Scattering from Biological Cells Relevant to Noninvasive Optical-Tissue Diagnostics*, Appl. Opt., (1998).
54. Ju, W, Liu, Q, Kim, K, Crowston, JG, Lindsey, JD, Agarwal, N, Ellisman, MH, Perkins, GA, Weinreb, RN, *Elevated Hydrostatic Pressure Triggers Mitochondrial Fission and Decreases Cellular Atp in Differentiated Rgc-5 Cells*, Invest. Ophthalmol. Vis. Sci., (2007).
55. Pasternack, R, Zheng, J, Boustany, NN, *Detection of Mitochondrial Fission with Orientation- Dependent Optical Fourier Filters*, Cytometry Part A, (2010).

56. Chalut, K, Ostrander, J, Giacomelli, M, Wax, A, *Light Scattering Measurements of Subcellular Structure Provide Noninvasive Early Detection of Chemotherapy-Induced Apoptosis*, Cancer Res., (2009).
57. Van Der Meer, F, Faber, D, Aalders, M, Poot, AA, Vermes, I, Van Leeuwen, T, *Apoptosis-and Necrosis-Induced Changes in Light Attenuation Measured by Optical Coherence Tomography*, Lasers Med. Sci., (2010).
58. Farhat, G, Mariampillai, A, Yang, V, Czarnota, G, Kolios, M, *Detecting Apoptosis Using Dynamic Light Scattering with Optical Coherence Tomography*, J. Biomed. Opt., (2011).
59. Pasternack, RM, Zheng, JZ, Boustany, NN, *Optical Scatter Changes at the Onset of Apoptosis Are Spatially Associated with Mitochondria*, J. Biomed. Opt., (2010).
60. Huang, X, Knighton, R, *Theoretical Model of the Polarization Properties of the Retinal Nerve Fiber Layer in Reflection*, Appl. Opt., 42 (2003) 5726-5736.
61. Zhou, Q, Knighton, R, *Light Scattering and Form Birefringence of Parallel Cylindrical Arrays That Represent Cellular Organelles of the Retinal Nerve Fiber Layer*, Appl. Opt., 36 (1997) 2273-2285.

VITA

Jordan Dwelle was born in Dallas, TX. After completing high school in Tyler, TX at Robert E. Lee H.S. in 1993 he lived in the northwest U.S. for several years working primarily in construction, woodworking, and seasonal jobs at resorts but was mainly interested in fly-fishing Montana streams for trout. He married Sarah on September 22, 1997 and moved to Bellingham, WA. He received an Associates degree from Whatcom Community College in 2000. From there he moved to Pullman, WA where his first daughter was born. He received a B.S. in Mechanical Engineering from Washington State University in 2003. In 2003 he enrolled at University of Texas at Austin and worked for Rebecca Richards-Kortum until 2005. In 2005 he received a Master of Science in biomedical engineering and began research for this dissertation under the joint supervision of Drs. Grady Rylander and Thomas Milner. While at UT he has had 3 additional children, two girls and a boy.

Permanent address (or email):

jdwelle@utexas.edu

This dissertation was typed by the author.